creative commons
COMMONS DEED

저작자표시-비영리-변경금지 2.0 대한민국

이용자는 아래의 조건을 따르는 경우에 한하여 자유롭게

- 이 저작물을 복제, 배포, 전송, 전시, 공연 및 방송할 수 있습니다.

다음과 같은 조건을 따라야 합니다:

저작자표시. 귀하는 원저작자를 표시하여야 합니다.

비영리. 귀하는 이 저작물을 영리 목적으로 이용할 수 없습니다.

변경금지. 귀하는 이 저작물을 개작, 변형 또는 가공할 수 없습니다.

- 귀하는, 이 저작물의 재이용이나 배포의 경우, 이 저작물에 적용된 이용허락조건을 명확하게 나타내어야 합니다.
- 저작권자로부터 별도의 허가를 받으면 이러한 조건들은 적용되지 않습니다.

저작권법에 따른 이용자의 권리는 위의 내용에 의하여 영향을 받지 않습니다.

이것은 이용허락규약(Legal Code)을 이해하기 쉽게 요약한 것입니다.

Disclaimer

dCollection

Ph. D. DISSERTATION

Graphene and Organic Flexible Electrodes for Highly Efficient Flexible Polymer Light-Emitting Diodes

고효율 플렉시블 폴리머 발광다이오드용
그래핀 및 유기 유연성 전극 개발에 대한 연구

BY

JAEHEUNG HA

FEBRUARY 2015

DEPARTMENT OF ELECTRICAL ENGINEERING AND
COMPUTUER SCIENCE
COLLEGE OF ENGINEERING
SEOUL NATIONAL UNIVERSITY

Graphene and Organic Flexible Electrodes for Highly Efficient Flexible Polymer Light-Emitting Diodes

고효율 플렉시블 폴리머 발광다이오드용 그래핀 및 유기 유연성 전극 개발에 대한 연구

지도교수 홍 용 택

이 논문을 공학박사 학위논문으로 제출함

2015 년 2 월

서울대학교 대학원

전기컴퓨터 공학부

하 재 흥

하재흥의 공학박사 학위논문을 인준함

2015 년 2 월

위 원 장 : 이 창 희 (인)

부위원장 : 홍 용 택 (인)

위 원 : 이 종 호 (인)

위 원 : 진 병 두 (인)

위 원 : 문 대 규 (인)

Abstract

Graphene and Organic Flexible Electrodes for Highly Efficient Flexible Polymer Light-Emitting Diodes

JAEHEUNG HA

DEPARTMENT OF ELECTRICAL ENGINEERING AND COMPUTER SCIENCE

COLLEGE OF ENGINEERING

SEOUL NATIONAL UNIVERSITY

In this Ph.D. dissertation, I investigated transparent and flexible electrodes as the alternative indium tin oxide (ITO) electrode for the highly efficient flexible display applications. Recently, flexible displays were successfully demonstrated using several flexible electrodes including graphene, silver nanowire, conductive polymeric anode, carbon nanotubes, metal grids, and thin metal films.

However, the graphene electrodes have not been utilized for polymer light emitting diodes (PLEDs) yet, although their simple device structure and

the solution-based fabrication process are expected to be more advantageous in terms of time and cost. I demonstrated high performance PLEDs which composed with simple two-layer structures using interface-engineered single-layer graphene films as anodes. The single-layer graphene synthesized by chemical vapor deposition methods was transferred onto a glass substrate utilizing an elastic stamp, and its work function was engineered by varying the duration and the power of ultraviolet ozone (UVO_3) treatment. I was able to optimize the contact between silver electrodes and the graphene anodes, leading to the considerable enhancement of light-emitting performance.

In case of the experiments about the conductive polymeric electrodes, highly efficient flexible PLEDs which composed with highly conductive and transparent foldable polymer electrodes were fabricated. New doping material, n-methyl-2-pyrrolidone (nMP) and n-methylformamide (nMF), have much improved the conductivity of poly(3,4-ethylenedioxythiophene) : poly(styrenesulfonate) (PEDOT:PSS). The selectively modulated inkjet-printing method facilitated the PEDOT:PSS's application to both transparent anodes and highly conductive bus line electrodes. Multiple-time printed electrodes showed similar performance to Ag bus lines while one-time printed anode showed much better figure of merit than ITO on the plastic substrates. Due to flexible property, high transparency and high work

function of the polymeric anode, ITO-free PLEDs showed high performance with foldable characteristics.

In order to increase the output efficiency of our device, high efficient flexible PLEDs which composed with the two dimensional nano hole arrays and highly conductive transparent polymer anodes were fabricated. The polymeric anodes were selectively deposited by an inkjet printing method. The photonic crystal structures embedded PLEDs showed high performance in the rigid and flexible substrates. The PC structures and polymeric anodes embedded flexible PLEDs showed an enhancement efficiencies by a factor of 1.31 and 1.28 in comparison with the normal PLEDs for the current and power efficiency at 979 cd/m^2, respectively. Moreover, ITO-free PLEDs showed the outstanding flexible property due to the mechanical property of the polymeric anode.

With the impedance spectroscopy, PLEDs with conductive polymeric anodes deposited by the inkjet printing process were investigated with impedance spectroscopy (IS). I analyzed the operational status of the PLEDs. In this work, the five devices were fabricated to study the effect of HIL and bus line electrode with two different anode materials, ITO and PEDOT:PSS. The equivalent circuit of our devices was established from IS measurements and analysis, including Cole-Cole plots, M-plots, Bode plots, and normalized resistance versus frequency plots. IS analysis showed that HIL should be

included in the series resistance, and EML should be divided to the interface region and the bulk region.

Moreover, to investigate the relationship between the IS parameter and the efficiency of the PLEDs, I fabricated PLEDs with PEDOT:PSS anodes on the various plastic substrates such as PA substrate, PS/PA substrate, and SiN_x/PA substrate. I showed the relationship between the IS parameters and the efficiency of the PLEDs, which the slope of the mobility extracted from the on-set frequency is related to the current and power efficiency of the PLEDs.

Keywords: polymer light-emitting diodes (PLEDs), transparent and conductive electrodes, graphene, conductive polymeric anode, PEDOT:PSS, impedance spectroscopy

Student Number: 2011-30262

Contents

Abstract i

Contents v

List of Figures ix

List of Tables xiv

Chapter 1 Introduction 1

1.1 Flexible Electrodes for the Future Display **1**

1.2 Impedance Spectroscopy **6**

1.3 Organization of This Dissertation **8**

Chapter 2 Graphene Electrode and its Devices 13

2.1 Introduction **13**

2.2 Experiments **16**

2.2.1 Preparation of the Graphene Substrate **16**

2.2.2 Transfer Length Method (TLM) 16
2.2.3 Fabrication of PLEDs 17
2.2.4 Measurements 18
2.3 Results and Discussion 20
2.3.1 Structures of Graphene-based PLEDs 20
2.3.2 Properties of Single-layer Graphene 21
2.3.3 Patterning of Graphene by UVO_3 treatment 23
2.3.4 Work Function Engineering 26
2.3.5 Selection of Bus Electrode for Low Contact Resistance 27
2.3.6 Characteristics of PLEDs 31
2.3.7 Flexible Property of Graphene Film 34
2.4 Summary 36
Chapter 3 Conductive Polymeric Electrode and its Devices 40
3.1 Introduction 40
3.2 Experiments 42
3.2.1 Preparation of Substrates 42
3.2.2 Preparation of Polymeric Anode Substrates 42
3.2.3 Fabrication of PLEDs 43
3.2.4 Measurements 43
3.3 Results and Discussion 44
3.3.1 Properties of PEDOT:PSS (E-157) 44

3.3.2 Flexible Property of PEDOT:PSS 52
3.3.3 Structure of PEDOT:PSS-based PLEDs 53
3.3.4 Energy Level Diagram 56
3.3.5 Characteristics of PEDOT:PSS-based PLEDs 58
3.4 Summary 65
Chapter 4 Flexible PLEDs with photonic crystal structures for high efficient devices 68
4.1 Introduction 68
4.2 Experiments 72
4.2.1 Fabrication of 2D Nano Hole Arrays 72
4.2.2 Preparation of Anode Substrate 72
4.2.3 Measurements 73
4.3 Results and Discussion 74
4.3.1 Laser Holographic Lithography 74
4.3.2 Device Fabrication Process 76
4.3.3 Structure of the Devices 79
4.3.4 Properties of the PEDOT:PSS film 83
4.3.5 Characteristics of the PLEDs 85
4.4 Summary 94
Chapter 5 Analysis with Impedance Spectroscopy 99
5.1 Introduction 99

5.2 Experiments 101

5.3 Effectiveness of HIL and Bus Electrodes 103

5.3.1 Characteristics of PLEDs 103

5.3.2 Reference Device 106

5.3.3 Devices without HIL or Bus Electrodes 110

5.3.4 Analysis with Impedance Spectroscopy 114

5.4 The relationship of efficiency and IS parameters ... 117

5.4.1 Two Parallel RC Circuits 117

5.4.2 Devices 122

5.4.3 Properties of the PEDOT:PSS anode 124

5.4.4 IS Measurements 127

5.5 Summary 131

Chapter 6 Conclusion 134

Publications and Conferences 138

한글 초록 141

List of Figures

Figure 1.1 Trends for display 2
Figure 1.2 Flexible and curved display revenue forecast 4
Figure 1.3 Impedance spectroscopy (a) equivalent circuit (b) Cole-Cole plot (c) M plot (d) bode plot ("Impedance spectroscopy", 2nd ed., J. Ross Macdonald).....7
Figure 2.1 Fabrication process of graphene based PLEDs.....20
Figure 2.2 Structures of PLEDs (a) schematic image of ITO-based PLEDs (b) schematic image of graphene-based PLEDs (c) SEM images of ITO-based PLEDs (d) SEM images of graphene-based PLEDs 21
Figure 2.3 AFM image of single-layer graphene film on the glass substrate.....22
Figure 2.4 Optical properties of single-layer graphene film 22
Figure 2.5 Patterning method of graphene film by UVO_3 treatment.....23
Figure 2.6 Measurement of resistance during patterning of graphene film.....24
Figure 2.7 Raman spectra of graphene films before and after UVO_3 treatment.....25
Figure 2.8 Change of work function (a) single-layer graphene (b) ITO 27
Figure 2.9 Schematic images of TLM.....28
Figure 2.10 Transfer length method (a) a plot of total resistance as a function of contact spacing (b) experimental data 30
Figure 2.11 Cross-sectional SEM images at the interface (a) between Ag and graphene (b) between Al and graphene 31
Figure 2.12 Characteristics of PLEDs (a) IVL plots (b) emission spectrum.....32
Figure 2.13 Efficiencies of PLEDs (a) graphene-based PLEDs (b) ITO-based PLEDs 34

Figure 2.14 The flexible test of ITO and graphene films (a) a custom made bending machine (b) the ratio of resistance.....35
Figure 3.1 Chemical structures (a) PEDOT (b) PSS (c) NMP (d) NMF.....44
Figure 3.2 Optical images of the PEDOT:PSS films on the glass substrate (a) with a modified background of SNU (b) with a white background 46
Figure 3.3 AFM images (a) substrates (glass, PA, and PS/PA) (b) ITO and PEDOT:PSS film.....47
Figure 3.4 Characteristics of the PEDOT:PSS and ITO films on the glass and the plastic substrates (a) thickness (b) sheet resistance (c) transmittance at 500nm (d) figure of merit.....50
Figure 3.5 Jetting of the inkjet printer head (a) at a fresh condition (b) At a nozzle clogging status.....51
Figure 3.6 Bending and folding test (a) images of custom made bending machine (b) ratio of resistance.....53
Figure 3.7 Resistance changes of ITO and PEDOT:PSS films during the bending test 54
Figure 3.8 (a) Structure of PLEDs (b) fabrication process.....55
Figure 3.9 Work function (a) UPS data (b) energy level diagram 57
Figure 3.10 Emission pixel images 58
Figure 3.11 Characteristics of four types PLEDs (a) IVL curve (b) efficiency curve 60
Figure 3.12 Characteristics of flexible PLEDs (a) IVL curve of ITO-PA PLEDs (b) efficiencies of ITO-PA PLEDs (c) IVL curve of PEDOT-PS/PA PLEDs (d) efficiencies of PEDOT-PS/PA PLEDs 61
Figure 3.13 IV characteristics of ITO-PA PLEDs after the folding stress test 63
Figure 3.14 Broken ITO film after the bending stress is applied 64
Figure 4.1 Schematic of OLED structure and optical ray diagram of light propagation with various modes including wave guided mode, glass guided mode and substrate escape mode.....69

Figure 4.2 Laser holography setup 74
Figure 4.3 Laser holographic lithography (a) for large period (b) for middle period (c) for short period 75
Figure 4.4 Conventional process for the anode preparation 76
Figure 4.5 Simple process with an inkjet printing method 78
Figure 4.6 Fabrication process of the PLEDs 78
Figure 4.7 Structures of the PLEDs (a) top images of the PEDOT:PSS anode (b) cross sectional image of the PEDOT:PSS anode (c) cross sectional image of the normal PLEDs 79
Figure 4.8 Structures of the PLEDs (a) top images of the 2D nano hole arrays (b) cross sectional image of 2D nano hole arrays (c) top images of the PEDOT:PSS anode on the 2D nano hole arrays (d) cross sectional image of the PEDOT:PSS anode on the 2D nano hole arrays (e) cross sectional image of the PC structures embedded PLEDs 81
Figure 4.9 Optical image (a) PC structures embedded anode substrate (b) normal anode substrate 82
Figure 4.10 Optical image of PC structures embedded PLEDs on the plastic substrate 82
Figure 4.11 Properties of the PEDOT:PSS anodes (a) transmittance (b) refractive index 83
Figure 4.12 Thickness and sheet resistance of the PEDOT:PSS anodes 84
Figure 4.13 Characteristics of the PLEDs (a) I-V-L characteristics of the PLEDs on the quartz substrate (b) current and power efficiency of the PLEDs on the quartz substrate 86
Figure 4.14 Characteristics of the PLEDs (a) I-V-L characteristics of the PLEDs on the SiNx/PA substrate, inset shows the emission devices with a bending stress (b) current and power efficiency of the PLEDs on the SiNx/PA substrate 88

Figure 4.15 Characteristics of the PLEDs (a) emission image of the normal PLEDs on the quartz substrate (4×4 arrays) (b) emission image of the PC structures embedded PLEDs on the quartz substrate (4×4 arrays).....89
Figure 4.16 Emission images (a) the 2 × 4 arrays of the normal PLEDs on the SiNx/quartz substrate (b) the 2 × 4 arrays of the PC structures embedded PLEDs on the SiNx/quartz substrate.....90
Figure 4.17 Emission images (a) 1 pixel of the normal PLEDs on the SiNx/PA substrate (b) 1 pixel of the PC structures embedded PLEDs on the SiNx/PA substrate 91
Figure 4.18 Schematics of light extractin for (a) a normal device (b) an OLED having the photonic crystal structures 91
Figure 4.19 Transmittance of the anodes and the substrates.....92
Figure 5.1 Schematic image of the device.....100
Figure 5.2 (a) IVL characteristics (b) power and current efficiencies.....105
Figure 5.3 Normalized resistance versus frequency (R-F plots) 106
Figure 5.4 (a) Cole-Cole plots (b) M plots (c) Bode plots of the device 1.....108
Figure 5.5 Equivalent circuit.....108
Figure 5.6 Cole-Cole plots of the high frequency region.....109
Figure 5.7 Plots of impedance spectroscopy (a) Cole-Cole plots (b) M plots (c) bode plots at 1.0 V (d) Cole-Cole plots (e) M plots (f) bode plots at 3.0 V.112
Figure 5.8 (a) Series resistance versus voltage (b) interface resistance and normalized interface capacitance versus voltage (c) bulk resistance and normalized bulk capacitance versus voltage 116
Figure 5.9 Schematic image of equivalent circuit.....116
Figure 5.10 Two parallel RC circuits 118
Figure 5.11 Schematic image of the device.....122
Figure 5.12 Characteristics of the PLEDs (a) I-V-L (b) efficiency graph.....123
Figure 5.13 Properties of the PEDOT:PSS films on the plastic substrates 124
Figure 5.14 Droplet images for measuring the surface energy.....126

Figure 5.15 Im(z) versus F plots (a) PLEDs on the PA substrates (b) PLEDs on the PS/PA substrates (c) PLEDs on the SiNx/PA substrate 127
Figure 5.16 Frequency versus the square root of the applied bias voltage.....128
Figure 5.17 Efficiencies of the PLEDs and slope from on-set frequency graph.....130

List of Tables

Table 2.1 Intensity ratio of 2D to G band of graphene film 25
Table 3.1 The surface roughness of the substrates and each anode film on the glass or plastic substrate 47
Table 3.2 Resistance changes during the bending or folding cycles 57
Table 3.3 Comparison table with previous reports 62
Table 4.1 Properties of the PEDOT:PSS film 85
Table 4.2 Characteristics of the PLEDs 90
Table 5.1 Parameters of each equivalent circuit 113
Table 5.2 Surface energy 126

Chapter 1 Introduction

1.1 Flexible Electrodes for the Future Display

Since the cathode ray tube (CRT) was introduced in 1897, the display industry has made considerable strides with several types of displays. The CRT was the representative of the 1st generation display, and the CRT had been recognized as the main display for more than 100 years until the 2nd generation display came into the market (**Figure 1.1**). With the coming of the 21st century, the main position in the display market was replaced with the flat panel displays (FPDs) such as liquid crystal displays (LCDs) and plasma display panel (PDPs). The FPDs has been developed into several rigid display applications including televisions and digital information displays (DIDs).

In recent years, there are significant research interests in the portable electronic devices including smart phones, tablet PCs, car navigations, and smart watches, which have several advantages of durable, lightweight, and

inexpensive display components. In some reports, the flexible display is considered as the front-runner in the next generation of the future optoelectronic devices, and the portable devices will be fabricated on the flexible display platform.[1] In this report, the flexible display will grow to 16% market share and $27 billion revenue of global display market by 2023 (**Figure 1.2**).

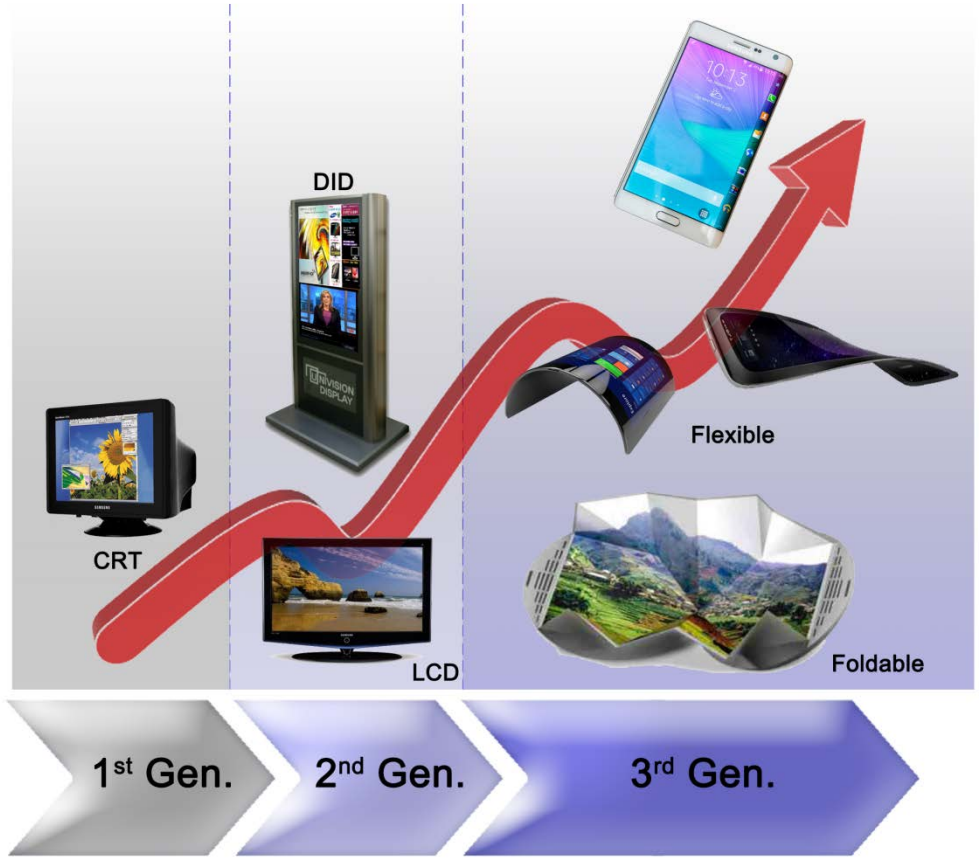

Figure 1.1 Trends for display

Recently, organic light-emitting diodes (OLEDs) have attracted a great attention for the flexible display applications, and have been considered as a front runner technology.[2] For realizing the flexible OLEDs, highly flexible, transparent, and conductive electrodes are essential. Although indium tin oxide (ITO) has been mainly used as a transparent electrode material in the various optoelectronic devices such as display, lightings, and photovoltaic applications, it is hard to be applied to the future flexible optoelectronic devices due to its brittleness, high fabrication costs due to the scarcity of indium, and poor surface property.[3-6] Moreover, the metal diffusion of indium into the organic layer, especially hole injection layer (HIL), is one of the failure mechanisms.[7-8] The presence of the injected metal in the organic layer increases the operating voltage and the power consumption, and reduces output efficiencies.[9]

Therefore, alternative flexible conductive electrodes have been intensively investigated in order to replace ITO including graphene,[10-13] conductive polymer,[14-16] silver nanowires,[17-18] carbon nanotubes,[19-20] and thin metal films.[21-22]

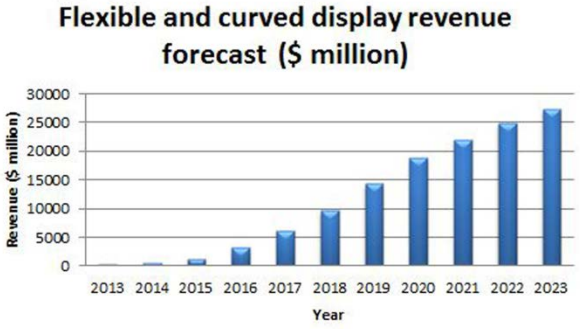

Figure 1.2 Flexible and curved display revenue forecast

Polymer light-emitting diodes (PLEDs) are one of the OLEDs, which are composed with the combination of polymeric organic layers and small molecule organic layers between two electrodes. PLEDs have been attracted many attentions because of their low fabrication costs, easy solution process, and potential applications for the flexible and printable optoelectronic devices.[23]

In addition to the flexible electrodes, the efficiency improvement of OLEDs has been one of the most significant topics in the flexible applications, which is related to a power consumption of the device. Although their internal quantum efficiency is reached almost 100% by using phosphorescent materials, their external quantum efficiency is usually limited to only 20%. Among the various modification techniques to enhance the low external quantum efficiency of conventional OLEDs, photonic crystal (PC) structures have been used, which were mainly fabricated on the rigid

substrate. However, the fabrication process of PC structures is very complicated. Moreover, the display device with PC structures has critical problems such as ghost images.

In this Ph.D. dissertation, I studied the properties of graphene and conductive polymer electrodes. With the conductive polymeric anode, I demonstrated the high efficient flexible PC structures embedded PLEDs.

1.2 Impedance Spectroscopy

Impedance spectroscopy (IS) is a popular analytical tool in material science areas because it involves a simple electrical measurement whose results often be correlated with many complex materials variables. IS is a powerful tool to understand the electrical properties of materials, and it can be employed to study the phenomena at organic/organic or organic/electrode interfaces in the OLEDs.[24-25] Experimentally obtained impedance data is analyzed by using an mathematical model based on a plausible physical theory. The experimental impedance data may be approximated by the impedance Z(ω) which made up of resistors (R), capacitors (C), and inductances (L).

IS has been applied to investigate the dynamics of mobile charges at the interface region or in the bulk region with the feature of easy, fast, and non-destructive method.[26-27] The power of IS analysis is the ability to determine impedance parameters from IS measurements such as Cole-Cole plot, Bode plot, and M plot (**Figure 1.3**).

In this Ph.D. dissertation, I investigated the flexible PLEDs with IS which composed with conductive polymeric anodes or ITO anodes. With the IS measurements, I modeled the equivalent circuits of the flexible PLEDs. Moreover, I investigated the relationship of the IS parameter and the device efficiency.

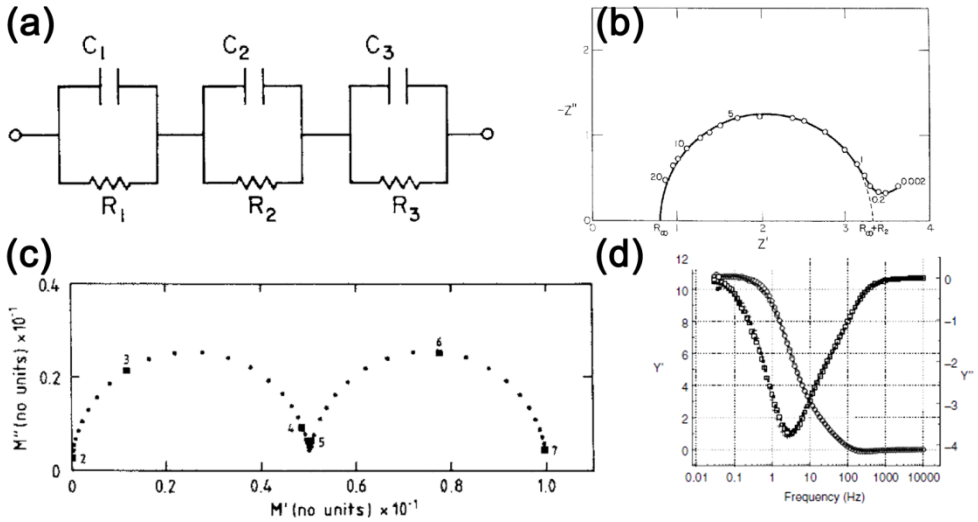

Figure 1.3 Impedance spectroscopy (a) equivalent circuit (b) Cole-Cole plot (c) M plot (d) bode plot ("Impedance spectroscopy", 2nd ed., J. Ross Macdonald)

1.3 Organization of This Dissertation

The work in this Ph.D. dissertation presents the studies on the transparent and flexible electrodes for the highly efficient and flexible display applications. The PLEDs which composed with conductive polymeric anodes were analyzed with the impedance spectroscopy.

This dissertation consists of six chapters including **Introduction** and **Conclusion**.

In **Chapter 1**, a brief history of display applications and some research issues of flexible electrodes, highly efficient devices, and impedance spectroscopy are introduced.

In **Chapter 2**, the electrical and optical properties of the single-layer graphene electrode were investigated. The new patterning method, the work function engineering method, and the selection of the proper metal bus line electrodes were introduced. The single-layer graphene-based PLEDs were compared with the ITO-based PLEDs on the glass substrate.

In **Chapter 3**, the new conductive polymeric anode material, PEDOT:PSS, were investigated. The characteristics of the PEDOT:PSS films deposited on the plastic substrate and its bending properties were included. The PEDOT:PSS-based PLEDs were compared with the ITO-based PLEDs on the plastic substrate.

In **Chapter 4**, the photonic crystal (PC) structures embedded PLEDs that

composed with the PEDOT:PSS electrodes, which utilized as the planarization layer and electrodes, were introduced. The PC-PLEDs were compared with the normal PLEDs which did not include PC structures on the rigid and flexible substrate.

In **Chapter 5**, the PEDOT:PSS-based PLEDs and ITO-based PLEDs were investigated with the impedance spectroscopy (IS). The equivalent circuit modeling of PLEDs was established from IS measurements and analysis. The relationship of device efficiency and IS parameters was investigated.

Reference

[1] *Touch display research*, "Flexible and Curved Display Technologies and Market Forecase Report.", September (2013)

[2] S. Reineke, F. Lindner, G. Schwartz, N. Seidler, K. Walzer, B. Lüssem, K. Leo, *Nature* **459**, 234 (2009)

[3] H. Aziz, Z. D. Popovic, *Chem. Mater*. **16**, 4522 (2004)

[4] P. Melpignano, A. Baron-Toaldo, V. Biondo, S. Priante, R. Zamboni, M. Murgia, S. Caria, L. Gregoratti, A. Barinov, M. Kiskinova, *Appl. Phys. Lett.* **86**, 041105 (2005)

[5] D. R. Cairns, R. P. Witte II, D. K. Sparacin, S. M. Sachsman, D. C. Paine, G. P. Crawford, *Appl. Phys. Lett.***76**, 1425 (2000)

[6] Y. Hong, Z. He, N. S. Lennhoff, D. A. Banach, J. Kanicki, *J. Electron. Mater*. **33**, 312 (2004)

[7] S. J. Jo, C. S. Kim, J. B. Kim, S. Y. Ryu, J. H. Noh, H. K. Baik, Y. S. Kim, S.-J. Lee, *J. Appl. Phys.***103**, 114502 (2008)

[8] C.-H. Chang, S.-A. Chen, *Appl. Phys. Lett.* **91**, 103514 (2007)

[9] S. T. Lee, Z. Q. Gao, L. S. Hung, *Appl. Phys. Lett.* **75**, 1404 (1999)

[10] J. Wu, N. Agrawal, H. A. Becerril, Z. Bao, Z. Liu, Y. Chen, P. Peumans, *ACS Nano* **4**, 43 (2010)

[11] T. Sun, Z. L. Wang, Z. J. Shi, G. Z. Ran, W. J. Xu, Z. Y. Wang, Y. Z. Li, L. Dai, G. G. Qin, *Appl. Phys. Lett*. **96**, 133301 (2010)

[12] T.-H. Han, Y. Lee, M.-R. Choi, S.-H. Woo, S.-H. Bae, B. H. Hong, J.-H. Ahn, T.-W. Lee, *Nat. Photonics* **6**, 105 (2012)

[13] J. Hwang, H. K. Choi, J. Moon, T. Y. Kim, J.-W. Shin, C. W. Joo, J.-H. Han, D.-H. Cho, J. W. Huh, S.-Y. Choi, J.-I. Lee, H. Y. Chu, *Appl. Phys. Lett.* **100**, 133304 (2012)

[14] K. Fehse, K. Walzer, K. Leo, W. Lövenich, A. Elschner, *Adv. Mater.* **19**, 441 (2007)

[15] Y. H. Kim, C. Sachse, M. Hermenau, K. Fehse, M. Riede, *Appl. Phys. Lett*. **99**, 113305 (2011)

[16] Y. H. Kim, C. Sachse, M. L. Machala, C. May, L. Müller-Meskamp, K. Leo, *Adv. Funct. Mater.* **21**, 1076 (2011)

[17] J.-Y. Lee, S. T. Connor, Y. Cui, P. Peumans, *Nano Lett*. **8**, 689 (2008)

[18] Z. Yu, Q. Zhang, L. Li, Q. Chen, X. Niu, J. Liu, Q. Pei, *Adv. Mater*. **23**, 664 (2011)

[19] J. Li, L. Hu, L. Wang, Y. Zhou, G. Grüner, T. J. Marks, *Nano Lett*. **6**, 2472 (2006)

[20] D. Zhang, K. Ryu, X. Liu, E. Polikarpov, J. Ly, M. E. Tompson, C. Zhou, *Nano Lett*. **6**, 1880 (2006)

[21] J. Meiss, M. K. Riede, K. Leo, *Appl. Phys. Lett*. **94**, 013303 (2009)

[22] L. H. Smith, J. A. E. Wasey, W. L. Barnes, *Appl. Phys. Lett*. **84**, 2986 (2004)

[23] J. H. Burroughes, D. D. C. Bradley, A. R. Brown, R. N. Marks, K. Mackay, R. H. Friend, P. L. Burns, and A. B. Holmes, *Nature* **347**, 539 (1990)

[24] T. Okachi, T. Nagase, T. Kobayashi, and H. Naito, *Thin Solid Films* **517**, 1327 (2008)

[25] G. G.-Belmonte, H. J. Bolink, and J. Bisquert, *Phys. Rev. B* **75**, 085316 (2007)

[26] S. Nowy, W. Ren, A. Elschner, W. Lövenich, and W. Brütting, *J. Appl. Phys*. **107**, 054501 (2010)

[27] I. H. Campbell, J. P. Ferraris, and D. L. Smith, *Appl. Phys. Lett*. **66**, 3030 (1995)

Chapter 2 Graphene Electrode and its Devices

2.1 Introduction

Since the first isolation of the graphene in 2004,[1] graphene has received remarkable attentions in the photonic and optoelectronic devices [2] such as OLEDs,[3-6] photovoltaic cells,[7] touch screens,[8] and light emitting electrochemical cells.[9-10] Although ITO has been mainly used as the transparent electrode material in display and photovoltaic applications due to its outstanding electrical and optical properties such as high transmittance, low resistivity, and chemical stability, many researchers have tried to find appropriate materials alternative to ITO because ITO has some disadvantages.

On the contrary, the graphene is one of the most promising candidates, and graphene electrode is expected to show not only outstanding transmittance and high conductivity but also smooth interface with adjustable

work functions, chemical inertness, and ultrahigh flexibility, which made it one of the promising candidates that replace ITO.[11-14] In practice, several papers have reported the use of graphene electrodes in small molecule OLED applications.[3-6] However, most of the papers show rather low efficiencies including current efficiency (cd/A) and power efficiency (lm/W) unless complicated multi-layered structures and additional hole injecting materials are utilized. So far, the introduction of the utilization of graphene electrodes for simple bi-layer structures of PLEDs has not been reported yet, although PLEDs are expected to become a commercial success in terms of low material costs, low investment costs, solution processibility, and flexibility.[15]

In most cases, multi-layer graphene electrodes have been used rather than single-layer graphene electrode because single-layer graphene shows a high sheet resistance and difficulty in handling.[3-6] However, the single-layer graphene shows much better performance in terms of surface roughness and optical transmittance compared with the multi-layer counterpart. Relatively the sheet resistance of anode may not limit the optoelectronic performance in bottom emission type displays because the transparent anodes are used only in a patterned manner just for individual pixels if the pixel emits uniformly. Therefore, appropriate methods for patterning, engineering

of its work function, and achievement of lower contact resistance between anodes and metal bus lines are more crucial than its conductivity.

Therefore, in this **Chapter 2**, I demonstrate the fabrication of highly efficient PLEDs using chemically modified single-layer graphene as an anode. I utilized the ultraviolet ozone (UVO_3) treatment for patterning and work function engineering of the single-layer graphene. The contact resistance between several metal bus lines and single-layer graphene electrodes were also investigated.

2.2 Experiments

2.2.1 Preparation of the Graphene Substrate

Single-layer graphene was synthesized by utilizing a chemical vapor deposition (CVD) process. The graphene film grown on the copper foil was covered by poly(methyl methacrylate) (PMMA) and floated in an aqueous solution of 0.1M ammonium persulphate ($(NH_2)_4S_2O_8$). After all the copper layers were etched away, submerging a clean PET film into the etchant and picking up the floating PMMA/graphene film to transfer it into DI water for 10 minutes to wash away remained ammonium persulphate etchants. The cleaning process was repeated 5 times. The graphene film with PMMA support was transferred to the glass. The sample was dried with a nitrogen immediately and was baked for 8 hours on the hot plate at 60 ºC, and then was placed into acetone at room temperature for 30 minutes to remove the PMMA support layer. The sample was dried and baked with in the same way.

2.2.2 Transfer Length Method (TLM)

Single-layer graphene film on a glass substrate was etched with the shadow mask by illuminating the UVO_3 in the air condition. The etching time was 15 minutes. Then, the several metal such as Ag, Al, Ti (99.995%, CERAC, USA) was deposited in the vacuum chamber under 5.0×10^{-6} torr

with the deposition rate at 5.0 Å/s, 2.0 Å /s, and 1.0 Å /s, respectively. The resistance between adjacent electrodes for the TLM and the patterning process optimization were measured by a semiconductor parameter analyzer (HP4145B, HP).

2.2.3 Fabrication of PLEDs

The prepared graphene films were transferred to a glass substrate (Soda-lime, Samsung Corning). For a reference device, ITO glass substrates were purchased from Free M Tech (Korea) were cleaned in the ultrasonic bath with acetone, isopropyl alcohol (IPA) and deionized water for each 10 minutes at 60 ℃ consecutively. Thickness and sheet resistance of the ITO were measured by a surface profiler (Surfcorder ET3000i, Kosaka) and 4 point probe (FPP-5000, Changmin), respectively. Then, the substrates were dried in an oven for 1 hour at 120 ℃. For PLEDs with the single-layer graphene anode, additional Ag (99.99%, Materion Advanced Chemical, U.S.A) electrodes were deposited under 5.0×10^{-6} torr by a thermal evaporation method in the vacuum chamber. The rate of deposition and the thickness of the Ag electrode is 5.0 Å/s and 1500 Å, respectively. To control the work function of anodes and to remove any organic contaminants on them, the substrates were treated by the UVO_3 for 5 minutes in case of the

graphene PLEDs and for 10 minutes in case of the ITO PLEDs. The power of UV lamp (Low Pressure Mercury Vopar Grid Lamp, Jelight) was 28mWcm^{-2}. After the UVO_3 treatment, the substrates were transferred to a globe box to control the concentration of H_2O and O_2 during the device fabrication. PEDOT:PSS (CLEVIOS ^{TM} P VP Al 4083, Heraeus, Germany) was spun-coated at 2000 rpm for 60 seconds. Then, annealing process was followed at 120℃ for 10 minutes. SPG-01T (Merck, Germany) that is a green emitting polymer was spun-coated by using 0.8 wt% concentrations in toluene solvent at 2000 rpm for 60 seconds. The substrates were annealed at 90℃ for 60 minutes. Next, Ca (99.99%, Sigma-Aldrich) was deposited at 1.0 Å/s rate in a vacuum chamber under 5.0×10^{-6} torr. Without breaking vacuum, Al (99.999%, CERAC, U.S.A) was deposited at 2.0 Å/s rate under 5.0×10^{-6} torr.

2.2.4 Measurements

The scanning electron microscope (SEM) images of a device structure and the atomic force microscopy (AFM) images of graphene films were taken by FE-SEM (Hitachi S-48000) and by non-contact mode of atomic force microscopy (XE-100, Park system), respectively. The work function was measured by photoemission yield spectroscopy (AC-2, Riken Keiki). The Raman spectrum and the transmittance of graphene films were measured

by Raman spectroscopy (Raman microsystem 2000, Renishaw) and ultraviolet visable spectrophotometer (Lambda 950, Perkin-Elmer). The electrical and optical characteristics of the PLEDs were measured by a digital multimeter (Keithley 2000, Keithley) and a source-measure unit (Keithley 237, Keithley) while sweeping voltage with a 0.1 V step. The measured data were calibrated by a spectroradiometer (CS-1000A, Konica Minolta).

2.3 Results and Discussion

2.3.1 Structures of Graphene-based PLEDs

Figure 2.1 shows the fabrication process of the graphene based PLEDs. First, the cleaning process was applied, and then UVO_3 treatment was followed. After HIL and EML was deposited by the spin-coating method, the bi-layer cathodes were deposited by the thermal evaporation method. The thickness of HIL, EML, Ca, and Al are 24, 70, 30, and 150 nm, respectively.

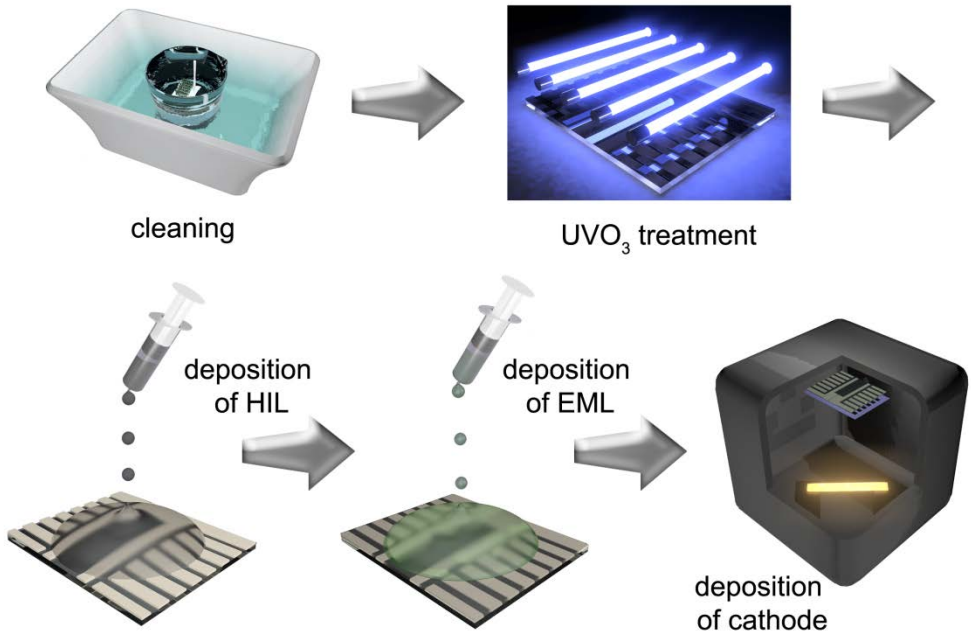

Figure 2.1 Fabrication process of graphene based PLEDs

Schematic structures of the graphene-based PLEDs and the ITO-based PLEDs are shown in **Figure 2.2** (a) and (b), respectively. ITO-based PLEDs

was used as the reference device. Corresponding cross-sectional SEM images are shown in **Figure 2.2** (c) and (d). The device structures of both PLEDs are identical except for the anode layer. The pixel size was 1.6×1.4 mm^2.

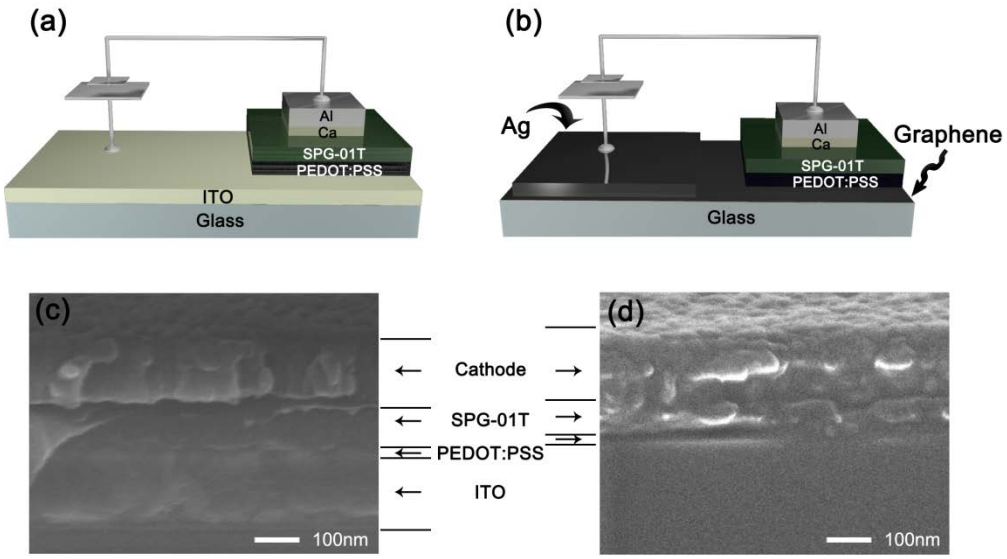

Figure 2.2 Structures of PLEDs (a) schematic image of ITO-based PLEDs (b) schematic image of graphene-based PLEDs (c) SEM images of ITO-based PLEDs (d) SEM images of graphene-based PLEDs

2.3.2 Properties of Single-layer Graphene

Two dimensional surface morphology of the graphene anode on the glass substrate is examined by using AFM as shown **Figure 2.3**. The graphene anode on the glass substrate exhibits very smooth surface roughness

with peak-to-peak features of 5.31 ± 0.15 nm and root mean square (RMS) under 1 nm. To confirm single-layer graphene film formation on the glass substrate, the Raman spectrum and transmittance of the transferred graphene film was measured by Raman spectroscopy and ultraviolet visible (UV-Vis) spectrophotometer. In **Figure 2.4**, the transmittance at 550 nm of the graphene film was 97.5%, which this result is consistent with previously reported paper,[16] and these results confirmed that graphene anode used in this experiment was single-layer.

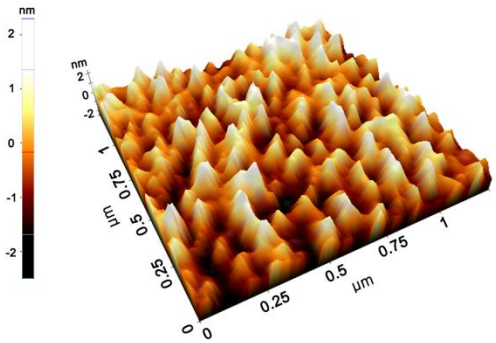

Figure 2.3 AFM image of single-layer graphene film on the glass substrate

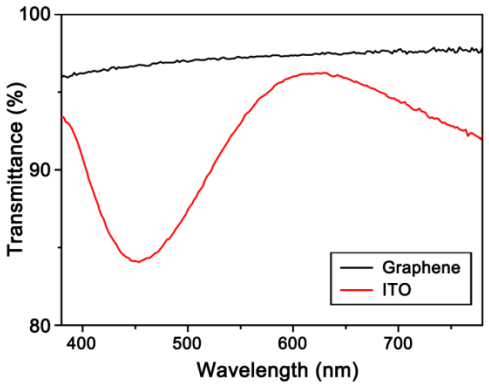

Figure 2.4 Optical properties of single-layer graphene film

2.3.3 Patterning of Graphene by UVO_3 treatment

Graphene film can be patterned by several methods, including oxidation,[17] plasma etching with chemically synthesized nanowires as an etch mask,[18] anisotropic etching,[19] scanning tunneling microscope lithography,[20] and photocatalytic patterning.[21] Although the conventional photolithography with O_2 plasma dry etching is an accurate etching method, the patterned films generally have a lot of contaminants originated from the photoresist residues and it requires some complicated process.[21] In order to simplify the patterning process and to obtain more high quality graphene anodes, the graphene anode was patterned by using UVO_3 treatment with a metal shadow mask (**Figure 2.5**). The exposure time has been optimized by monitoring the resistance between adjacent patterned electrodes as shown in **Figure 2.6** (a). **Figure 2.6** (b) shows that the resistance were rarely changed when the single-layer graphene anode were exposed to UVO_3 less than 5 minutes.

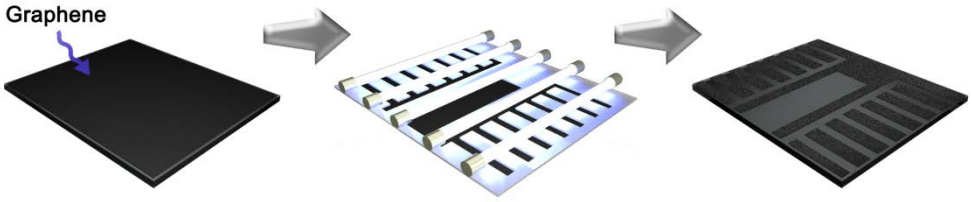

Figure 2.5 Patterning method of graphene film by UVO_3 treatment

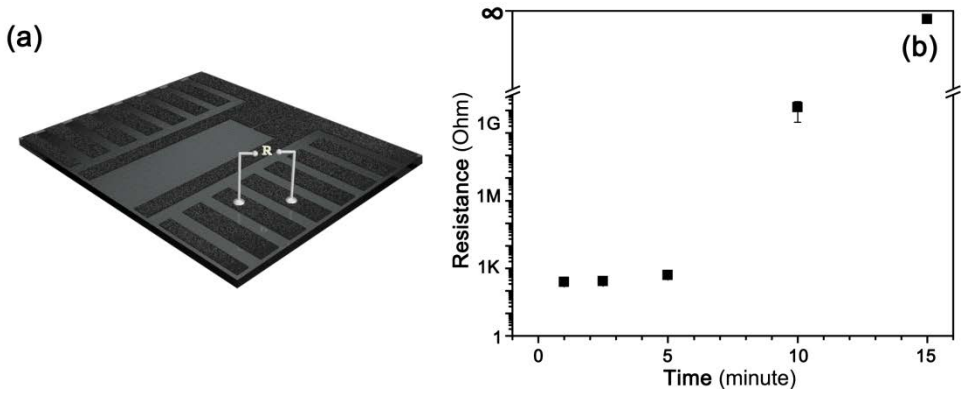

Figure 2.6 Measurement of resistance during patterning of graphene film

Moreover, Raman spectrum shows that the graphene anode maintains the single layer property until 5 minutes of UVO_3 treatment, which results are supported by the intensity ratio of 2D to G band (I_{2D}/I_G) (**Figure 2.7**). The intensity ratio of 2D to G band are varied from 4.521 to 1.16, and the full-width half-maximum (FWHM) are increased from 25.92 to 46.72 cm^{-1} which are summarized in **Table 2.1**. The broadening and the decrease of the 2D bands is due to the oxygen containing groups, including C − O, O − C = O, and C = O bonds on the graphene surface which are appeared while the graphene anode are exposed to UVO_3.[22]

After about 15 minutes, the resistance is infinite and the peaks in the Raman spectra are disappeared (**Figure 2.6** (b) and **Figure 2.7**), which shows that the single-layer graphene anodes were totally removed from the exposed

area, and became into the electrically isolated electrode patterns. If the power of UVO_3 and distance to the UV lamp in the patterning system is optimized, the process time can be further reduced.

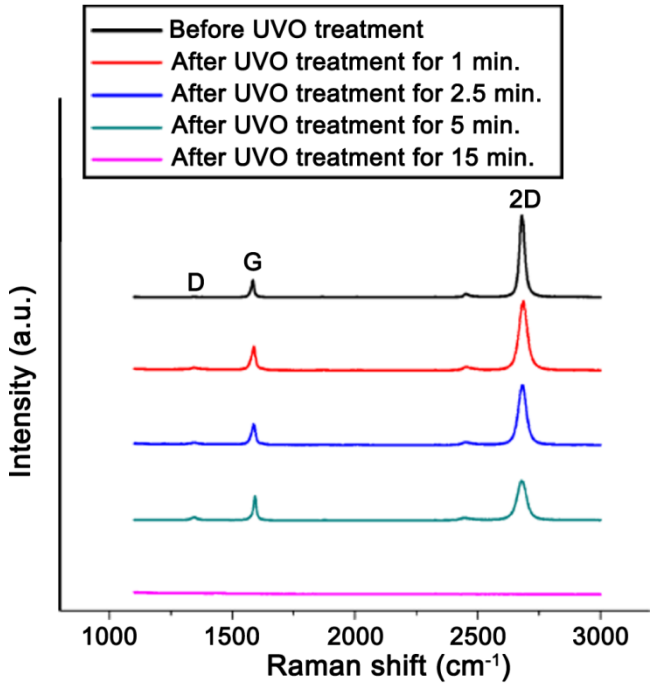

Figure 2.7 Raman spectra of graphene films before and after UVO_3 treatment

	I_{2D}/I_G	FWHM (cm^{-1})
Before UVO treatment	4.521	25.92
After UVO treatment for 1 min.	2.768	39.76
After UVO treatment for 2.5 min.	2.709	39.78
After UVO treatment for 5 min.	1.616	46.72

Table 2.1 Intensity ratio of 2D to G band of graphene film

2.3.4 Work Function Engineering

When we further investigated the property of the graphene anodes during the first 5 minutes, it was found that the UVO_3 treatment can effectively control the work function of the single-layer graphene film without losing its electrical conductivity. It is well known that the work function of the anode in OLEDs is related to the hole injection barrier, and its value is very important in improving the efficiency of hole injection to the hole injection layer (HIL) or hole transporting layer (HTL). In fact, the UVO_3 treatment is also a well-known technology to control the work function of the conventional ITO anode. However, it has not been applied yet to control the work function of graphene films, although several groups reported useful methods for controlling the work function of graphene films, including $AuCl_3$ doping,[23] AlO_x overlayers,[24] HNO_3 treatment,[25] electric field effect,[26] and functionalization by self-assembled monolayers.[27]

The time of the UVO_3 treatment needs to be well controlled because the work function of the single-layer graphene film sensitively changes with the exposure time. **Figure 2.8** shows the change of the work function of the single-layer graphene anodes and ITO anodes during the UVO_3 treatment, which were measured by photoemission yield spectroscopy. These results show that the work function of the single-layer graphene anode increases with the UVO_3 treatment time. The work function of the UVO_3 treated

single-layer graphene film for 2.5 minutes and 5 minutes was changed by 0.18 eV and 0.27 eV, respectively, comparing with non-treated graphene film. The work function of the ITO anode was also moved by 0.42 eV after 10 minutes of the UVO_3 treatment. This result shows that the UVO_3 treatment can be effectively utilized to control the work function of both single-layer graphene anode and ITO anode. This UVO_3 treatment introduces the down shifting of the graphene Fermi level, which results to the p-type doping of the graphene.[22]

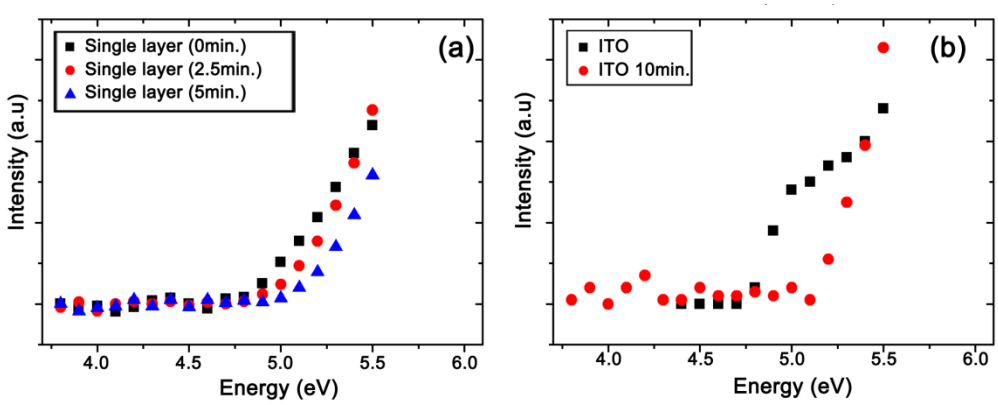

Figure 2.8 Change of work function (a) single-layer graphene (b) ITO

2.3.5 Selection of Bus Electrode for Low Contact Resistance

In a typical AMOLED display panel, there are several additional metal lines, in addition to anode and cathode, which span horizontally and vertically to operate individual sub-pixels, such as data, initialization, scan

and power lines. In most cases, low-resistive materials are used to implement those lines in contact with the patterned transparent anode such as aluminum or aluminum alloys. If there is significant contact resistance between the metal lines and each pixel anode, undesired voltage drop is induced at the contact area, and resulting in the degradation of display uniformity. Therefore, it must be considered that the contact resistance between the single-layer graphene and metal bus lines should be minimized in order to use the graphene as the materials of pixel anodes. Thus, we used a transfer length method (TLM) to investigate the contact resistance properties of the single-layer graphene and several metal materials. The schematic images of the TLM and the device top view are visualized in **Figure 2.9**. *L* is the length of the contact electrode (500 ㎛), *Z* is the width of the contact electrode (1 mm), *W* is the width of the patterned single-layer graphene film (1.4 mm), and *d* is the contact spacing length (from 150 ㎛ to 450 ㎛ with an interval of 50 ㎛).

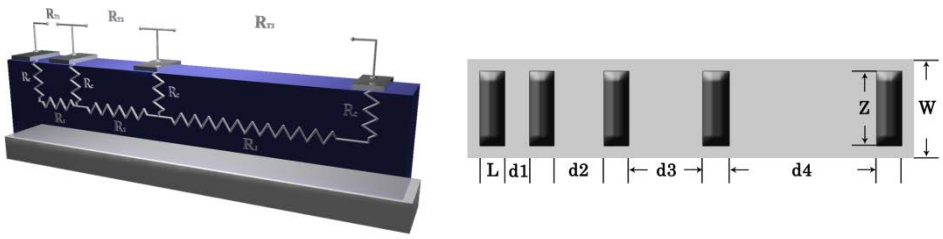

Figure 2.9 Schematic images of TLM

The contact resistance with various metal electrodes and the sheet resistance of the single-layer graphene anode can be extracted from the graph of a total resistance versus spacing distances (**Figure 2.10** (a)). R_T is a total resistance, R_{sh} is the sheet resistance of the single-layer graphene, and R_c is the contact resistance between the single-layer graphene and metal electrodes, and L_T is a transfer length. Several combinations of potential metal electrodes including Ag, Al, Ti/Ag, and Ti/Al were investigated, which the metal electrodes can be applied to the display panel. The thickness of metal electrodes such as Ag, Al, and Ti was 150 nm, 150 nm, and 20 nm, respectively, which were all measured by a surface profiler. **Figure 2.10** (b) shows that the sheet resistance of the single-layer graphene anode is 914.38 ± 9.41 Ω/□. The specific contact resistivity (ρ_c) can be calculated with **Equation 2.1**,[27] and the value between the single-layer graphene anode and Ag, Al, Ti/Ag, and Ti/Al metal electrodes are 4.96×10^{-6} Ω-mm^2, 3.16×10^{-4} Ω-mm^2, 7.51×10^{-6} Ω-mm^2, and 5.39×10^{-4} Ω-mm^2, respectively.

Equation 2.1 $$\rho_c=(L_T)^2\times R_{sh}$$

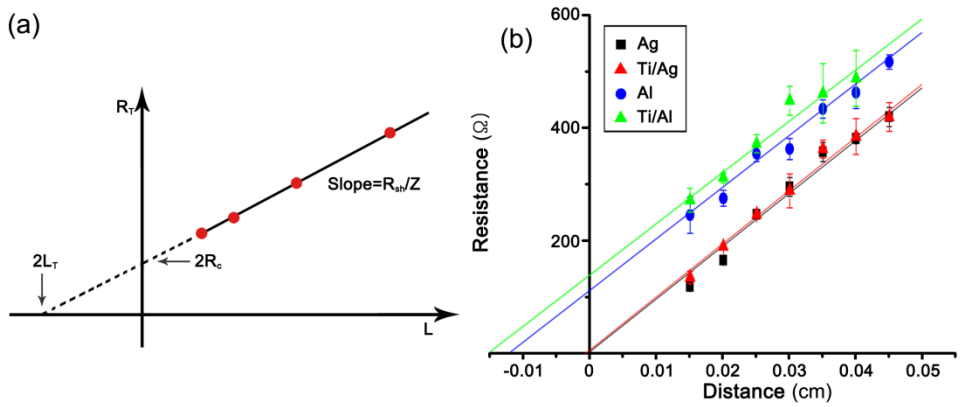

Figure 2.10 Transfer length method (a) a plot of total resistance as a function of contact spacing (b) experimental data

The results show that the specific contact resistivity of Al is higher than that of Ag due to poor adhesion of Al and graphene, which is consistent with the previous report.[28] The higher contact resistance of Al and graphene comes from the delamination of Al on the graphene film. The cross-sectional SEM images showed that Ag has a good adhesion property, but in case of Al, The hollow point between Al and graphene film can be easily detected (**Figure 2.11**). These defects cause the higher contact resistance in the Al and single-layer graphene contact point. Therefore, I used Ag as the contact and bus line electrode material to fabricate PLEDs which composed with the single-layer graphene anodes.

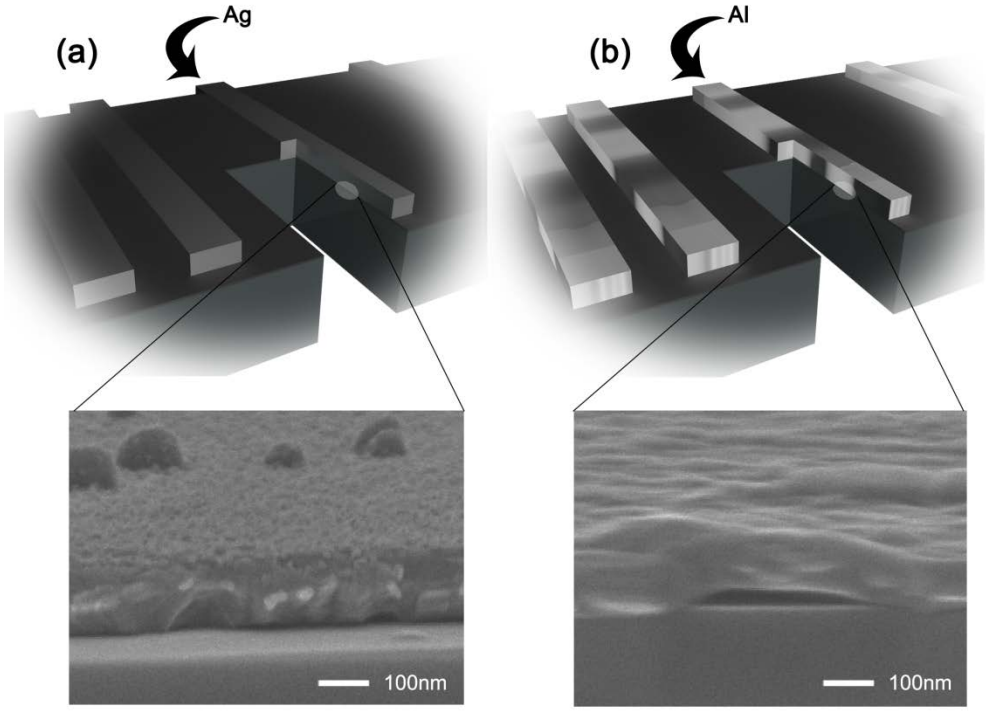

Figure 2.11 Cross-sectional SEM images at the interface (a) between Ag and graphene (b) between Al and graphene

2.3.6 Characteristics of PLEDs

In order to determine the electrical and optical properties of our PLEDs, I measured the current and luminance versus applied voltage of PLEDs with ITO anode (ITO-based PLEDs) and single-layer graphene anode (graphene-based PLEDs). The IVL curve shows in **Figure 2.12** (a). The turn-on voltage which defined as a bias voltage at the luminance of 1 cd/m^2 was 3.2 V and 3.6 V for ITO-based PLEDs and graphene-based PLEDs, respectively. The

graphene-based PLEDs have comparable current level to the ITO-based PLEDs for applied bias under 5 V. At bias > 5 V, the current level and the overall light intensity of the graphene-based PLEDs is lower than that of the ITO-based PLEDs, which is due to the high sheet resistance of the single-layer graphene anode. The sheet resistance of the ITO anode is 10.10 ± 0.11 Ω/□. In **Figure 2.12** (b), the emission spectrum of both PLEDs is shown, which is almost same to each other. The maximum peaks are located at 507 nm and 509nm for the graphene-based PLEDs and the ITO-based PLEDs, respectively. The second peaks are located at 533 nm and 531 nm.

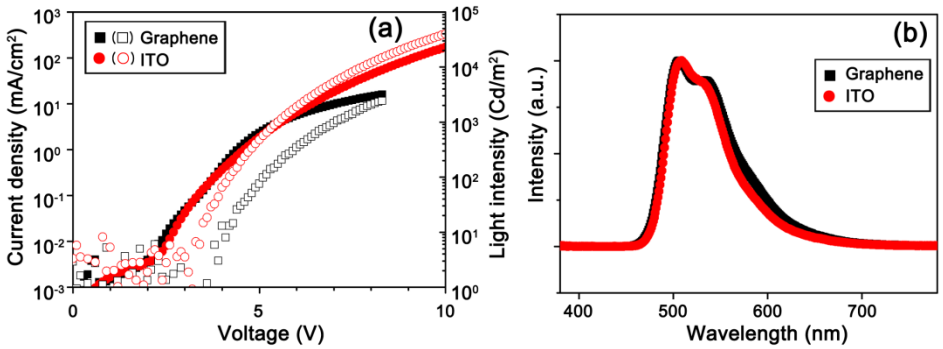

Figure 2.12 Characteristics of PLEDs (a) IVL plots (b) emission spectrum

The current and power efficiencies of the both PLEDs are shown in **Figure 2.13**. The maximum current efficiency and power efficiency of the graphene-based PLEDs are 9.13 cd/A (at 761 cd/m^2) and 5.51 lm/W (at 353

cd/m^2), respectively. At 1,008 cd/m^2, the efficiencies are 9.59 cd/A and 4.72 lm/W. For the ITO-based PLEDs, the maximum current and power efficiencies are 12.48 cd/A (at 1,444 cd/m^2) and 8.01 lm/W (at 125 cd/m^2), respectively. At 963 cd/m^2, the efficiencies are 12.46 cd/A and 7.01 lm/W. The emission photographs of both PLEDs operating at 0.5 mA appear in inset of **Figure 2.13**.

The graphene-based PLEDs showed comparable performances to the ITO-based PLEDs when UVO_3 treatment and Ag bus line electrodes are applied. I believe that the high sheet resistance effects on the degradation of the device performance is more significant for the large area emitting device, while it is negligible for the small area devices in few hundreds micrometer order such as AMOLED pixels. In addition, when additional methods such as hybridization with metal grids, silver nanowires, and chemical doping on the graphene films are applied simultaneously, the performance of PLEDs is expected to be further improved. Moreover, the graphene-based PLEDs are free from the metal diffusion problems between ITO and PEDOT:PSS for HIL, which often degrades the device performance.

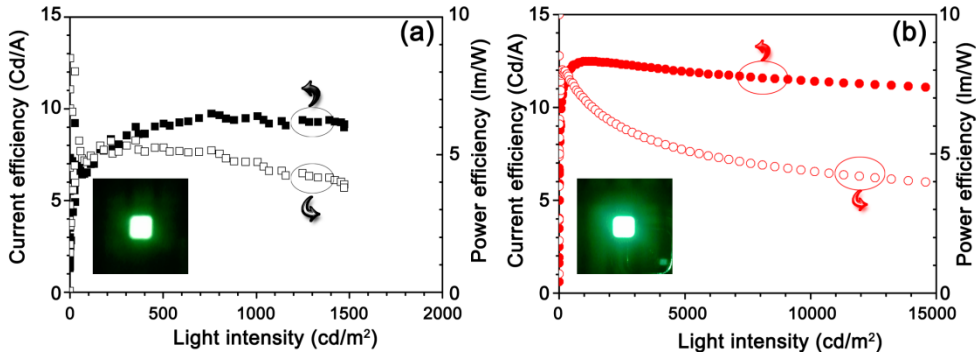

Figure 2.13 Efficiencies of PLEDs (a) graphene-based PLEDs (b) ITO-based PLEDs

2.3.7 Flexible Property of Graphene Film

To check the industrial applicability of the graphene film, the resistance variation was measured with a custom made bending machine, while the speed and moving distance were varied. The graphene film was transferred to the plastic film by the wet transfer method. The bending radius is moved from 21.57 to 8.58 mm when the moving distance is varied from 0 to 12mm. **Figure 2.14** shows the custom bending machine and the resistance variance of ITO and graphene film. Although the resistance of ITO films is drastically changed with the moving distance, the resistance of graphene films is not changed. Moreover, the resistance variance is more seriously applied to the bending radius than the moving speed.

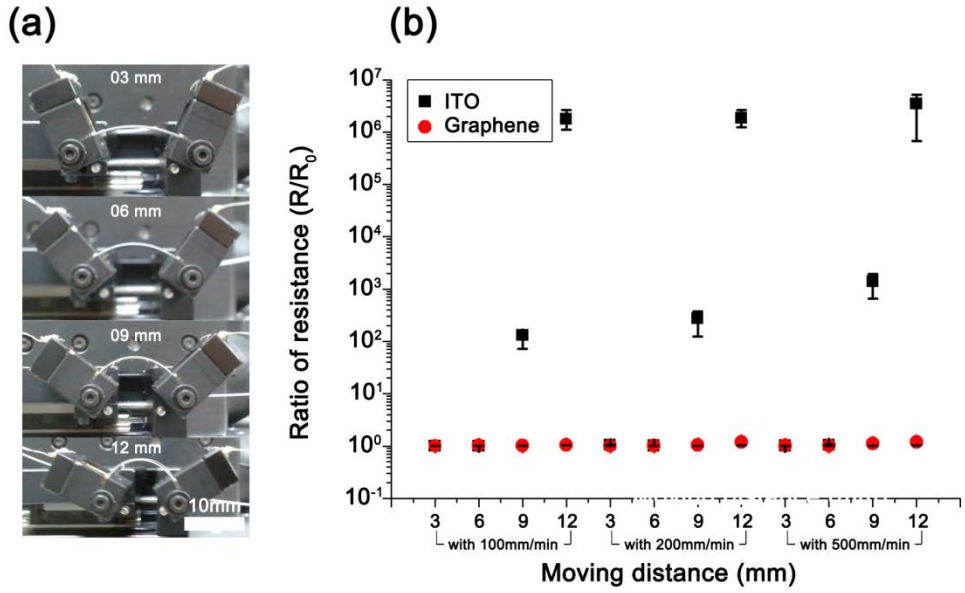

Figure 2.14 The flexible test of ITO and graphene films (a) a custom made bending machine (b) the ratio of resistance

2.4 Summary

In this **Chapter 2**, I demonstrated that the single-layer graphene anode can be used as the transparent and conductive anode of the PLEDs. The UVO_3-assisted pattering and work function engineering are useful to improve the performance of the PLEDs. Furthermore, the good contact property of the graphene with Ag material will enable us to introduce our print Ag electrode combined with the single-layer graphene anode for the flexible and potentially stretchable display application. [29]

References

[1] K. S. Novoselov, A. K. Geim, S. V. Morozov, D. Jiang, Y. Zhang, S. V. Dubonos, I. V. Grigorieva, A. A. Firsov, *Science* **306**, 666 (2004)

[2] F. Bonaccorso, Z. Sun, T. Hasan, A. C. Ferrari, *Nat. Photonics* **4**, 611 (2010)

[3] J. Wu, M. Agrawal, H. A. Becerril, Z. Bao, Z. Liu, Y. Chen, P. Peumans, *ACS Nano* **4**, 43 (2010)

[4] T. Sun, Z. L. Wang, Z. J. Shi, G. Z. Ran, W. J. Xu, Z. Y. Wang, Y. Z. Li, L. Dai, G. G. Qin, *Appl. Phys. Lett*. **96**,133301 (2010)

[5] T.-H. Han, Y. Lee, M.-R. Choi, S.-H. Woo, S.-H. Bae, B. H. Hong, J.-H. Ahn, T.-W. Lee, *Nat. Photonics* **6**, 105 (2012)

[6] J. Hwang, H. K. Choi, J. Moon, T. Y. Kim, J.-W. Shin, *Appl. Phys. Lett*. **100**, 33304 (2012)

[7] L. G. D. Arco, Y. Zhang, C. W. Schlenker, K. Ryu, M. E. Thomson, C. Zhou, *ACS Nano* **4**, 2865 (2010)

[8] S. Bae, H. Kim, Y. Lee, X. Xu, J.-S. Park, Y. Zheng. J. Balakrishnan, T. Lei, H. R. Kim, Y. I. Song, Y.-J. Kim, K. S. Kim, B. Özyilmaz, J.-H. Ahn, B. H. Hong, S. Iijima, *Nat. Nanotechnol*. **5**, 574 (2010)

[9] P. Matyba, H. Yamaguchi, G. Eda, M. Chhowalla, L. Edman, N. D. Robinson, *ACS Nano* **4**, 637 (2010)

[10] P. Matyba, H. Yamaguchi, M. Chhowalla, N. D. Robinson, L. Edman, *ACS Nano* **5**, 574 (2011)

[11] H. Aziz, Z. D. Popovic, *Chem. Mater*. **16**, 4522 (2004)

[12] P. Melpignano, A. Baron-Toaldo, V. Biondo, S. Priante, R. Zamboni, M. Murgia, S. Caria, L. Gregoratti, A. Barinov, M. Kiskinova, *Appl. Phys. Lett.* **86**, 041105 (2005)

[13] D. R. Cairns, R. P. Witte II, D. K. Sparacin, S. M. Sachsman, D. C. Paine, G. P. Crawford, *Appl. Phys. Lett.* **76**, 1425 (2000)

[14] Y. Hong, Z. He, N. S. Lennhoff, D. A. Banach, J. Kanicki, *J. Electron. Mater*. **33**, 312 (2004)

[15] Y. Hong, J. Kanichi, *IEEE Trans. Electron Devices* **51**, 1562 (2004)

[16] K. S. Kim, Y. Zhao, H. Jang, S. Y. Lee, J. M. Kim, K. S. Kim, J.-H. Ahn, P. Kim, J.-Y. Choi, B. H. Hong, *Nature* **457**, 706 (2009)

[17] N. Severin, S. Kirstein, I. M. Sokolov, J. P. Rabe, *Nano Lett*. **9**, 457 (2009)

[18] J. Bai, X. Duan, Y. Huang, *Nano Lett*. **9**, 2083 (2009)

[19] L. C. Campos, V. R. Manfrinato, J. D. Sanchez-Yamagishi, J. Kong, P. Jarillo-Herrero, *Nano Lett*. **9**, 2600 (2009)

[20] L. Tapasztó, G. Dobrik, P. Lambin, L. P. Biró, *Nat. Nanotechnol*. **3**, 397 (2008)

[21] L. Zhang, S. Diao, Y. Nie, K. Yan, N. Liu, B. Dai, Q. Xie, A. Reina, J. Kong, Z. Liu, *J. Am. Chem. Soc*. **133**, 2706 (2011)

[22] S. Huh, J. Park, Y. S. Kim, K. S. kim, B. H. Hong, J.-M. Nam, *ACS Nano* **5**, 9799 (2011)

[23] Y. Shi, K. K. Kim, A. Reina, M. Hofmann, L.-J. Li, J. Kong, *ACS Nano* **4**, 2689 (2010)

[24] Y. Yi, W. M. Choi, Y. H. Kim, J. W. Kim, S. J. Kang, *Appl. Phys. Lett*. **98**, 013505 (2011)

[25] Y.-J. Yu, Y. Zhao, S. Ryu, L. E. Brus, K. S. Kim, P. Kim, *Nano Lett*. **9**, 3430 (2009)

[26] W. H. Lee, J. Park, Y. Kim, K S. Kim, B. H. Hong, K. Cho, *Adv. Mater*. **23**, 3460 (2011)

[27] L. K. Mak, C. M. Rogers, D. C. Northrop, *J. Phys. E: Sci. Instrum*. **22**, 317 (1989)

[28] J. A. Robinson, M. LaBella, M. Zhu, M. Hollander, R. Kasarda, Z. Hughes, K. Trumbull, R. Cavalero, D. Snyder, *Appl. Phys. Lett*. **98**, 053103 (2011)

[29] S. Chung, J. Lee, H. Song, S. Kim, J. Jeong, Y. Hong, *Appl. Phys. Lett*. **98**, 153110 (2011)

Chapter 3 Conductive Polymeric Electrode and its Devices

3.1 Introduction

Poly(3,4-ethylenedioxythiophene):poly(styrenesulfonate) (PEDOT:PSS) has emerged as one of the most promising material for the transparent electrode in OLEDs and organic solar cells (OSCs).[1-8] In fact, PEDOT:PSS is one of the well-known material for the hole injecting layer (HIL) in the OLEDs due to its good electrical conductivity and high transmittance.[9] As well as its flexibility from the polymeric material property, PEDOT:PSS has an advantage of easy controllability of its electrical property. Therefore, many research groups have introduced some doping method into the PEDOT:PSS with various doping materials such as dimethyl sulfoxide (DMSO),[1] ethylene glycol (EG),[2-3] glycerol,[4] and N,N-dimethylacetamide (DMAc).[5] Although such anodes were applied for OLEDs, their power and current efficiencies were still low comparing with the OLEDs which composed with the ITO anodes.[1-7]

Another key advantage of the PEDOT:PSS is that the patterning of PEDOT:PSS and the thickness control of the PEDOT:PSS film can be done

by a simple inkjet printing process.[7-8] The complicated photolithography steps, the usage of materials, and the fabrication costs can be reduced with the inkjet printing. Since the PEDOT:PSS thin films have the trade-off between its conductivity and its transmittance depending on the film thickness, I can utilize this property to implement both the bus line electrode and the anode by just modulating the film thickness. The thickness of the PEDOT:PSS electrodes can be appropriately optimized for each usage by a simple inkjet printing technology. Moreover, some previous literatures [1-4, 8] reported OLEDs which used the PEDOT:PSS anode, however, all of them utilized a rigid glass substrate although the PEDOT:PSS anode has the outstanding mechanical flexibility. Therefore, in this **Chapter 3**, I demonstrated the fabrication of highly efficient flexible PLEDs with the inkjet-printed PEDOT:PSS anode and bus line electrodes.

3.2 Experiments

3.2.1 Preparation of Substrates

To prepare the polystylene (PS, Sigma Aldrich, USA) / polyarylite (PA, Ferrania, Italy) substrate, PS solution (1.8wt% in toluene) was deposited by the spin coating method on the PA substrate at 2000 rpm for 1 minute, and then the PS film was annealed at 120 ºC for 30 minutes

3.2.2 Preparation of Polymeric Anode Substrates

The PEDOT:PSS ink drop speed was 8 m/s, and the inkjet printing process was carried out at the room temperature without a stage heating. After the printing process, the PEDOT:PSS films were undergone the annealing process on the hot plate at 120 ºC for 1 hour. In the device which composed with the PEDOT:PSS anodes and Ag bus line electrodes (PEDOT:PSS-Ag PLEDs), the Ag ink (Sigma Aldrich) was printed on the PEDOT:PSS anode with a 10 picoliter cartridge and with a drop speed of 9 m/s. The printed Ag bus line electrodes were annealed in the oven at 120 ºC for 20 minutes. In the device which composed with the PEDOT:PSS anodes and the PEDOT:PSS bus line electrodes (PEDOT:PSS-PS/PA PLEDs), the PEDOT:PSS bus line electrodes were printed on the PEDOT:PSS anode by 7 times without a break. After 7 times printing, the PEDOT:PSS bus line electrodes were annealed on the hot plate at 120 ºC for 1 hour.

3.2.3 Fabrication of PLEDs

Except for the number of the printing times of HIL and the material of the electron injection material (EIL), the other fabrication processes were equal to the device which fabricated in the **Chapter 2**. In case of PLEDs on the glass substrate, the number of coating time of the HIL was just 1 time. In case of PLEDs fabricated on the PS/PA substrate, 3 times coating process was carried out. As the material of the EIL, lithium fluoride (LiF, 99.9 %, CERAC) was deposited at 0.1 Å/s in a vacuum chamber by a thermal evaporation method.

3.2.4 Measurements

The transmittance was measured by a spectrophotometer (DU-70, Beckman) in the range from 780nm to 380 nm with 1 nm step. The work function of the PEDOT:PSS for the anode, ITO, and PEDOT:PSS for the HIL were measured by ultraviolet photoelectron spectroscopy (UPS, Axis-Nova, Kratos) with He source (21.2 eV). The bending and folding properties were examined by our custom made bending machine, and the variation of the resistance before and after the bending and folding stress was measured by a Keithley 2400 sourcemeter. The other measurements such as the thickness, sheet resistance, AFM, and SEM are equal to the measurement systems in the **Chapter 2**

3.3 Results and Discussion

3.3.1 Properties of PEDOT:PSS (E-157)

PEDOT:PSS (E-157) which used as the anodes and the bus line electrodes in this dissertation, was supplied from Con-Tech. PEDOT and PSS were mixed in a weight ratio of 1:2.5. In our PEDOT:PSS films, two doping elements, N-methylformamide (NMF) and N-methyl-2-pyrrolidone (NMP), were included to increase its conductivity. The PEDOT:PSS anode and bus line electrodes were deposited on the glass and plastic substrates by the inkjet printing process. **Figure 3.1** shows the chemical structures of the materials which included in the PEDOT:PSS film (PEDOT, PSS, NMP, and NMF). **Figure 3.2** shows the optical images of the PEDOT:PSS films which deposited on the glass substrates by the inkjet printing process.

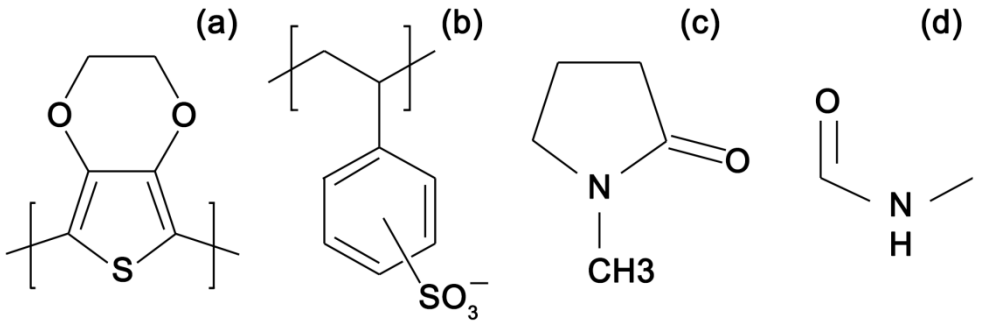

Figure 3.1 Chemical structures (a) PEDOT (b) PSS (c) NMP (d) NMF

Figure 3.2 shows the optical images of the PEDOT:PSS films on the glass substrate for the number of printing times. **Figure 3.2** (a) shows the images with a background of the modified symbol of Seoul National University. **Figure 3.2** (b) shows the photographs with a white background. The 1-time printed PEDOT:PSS film has the highest transparency, and the color of the PEDOT:PSS film on the glass substrate became dark depending on the printing times.

Figure 3.2 Optical images of the PEDOT:PSS films on the glass substrate (a) with a modified background of SNU (b) with a white background

Figure 3.3 shows a surface roughness of the glass, PA, and PS/PA substrates and each anode film. In the **Figure 3.3** (a), the PS/PA substrate has a smooth surface roughness comparing with the PA substrate. ITO film on the PA substrate has a smoother surface roughness than that of ITO film on the glass substrate because ITO film on the PA substrate could not be

experienced any annealing process. Peak to valley (R_{pv}) and root mean square (RMS) values of each sample are summarized in **Table 3.1**

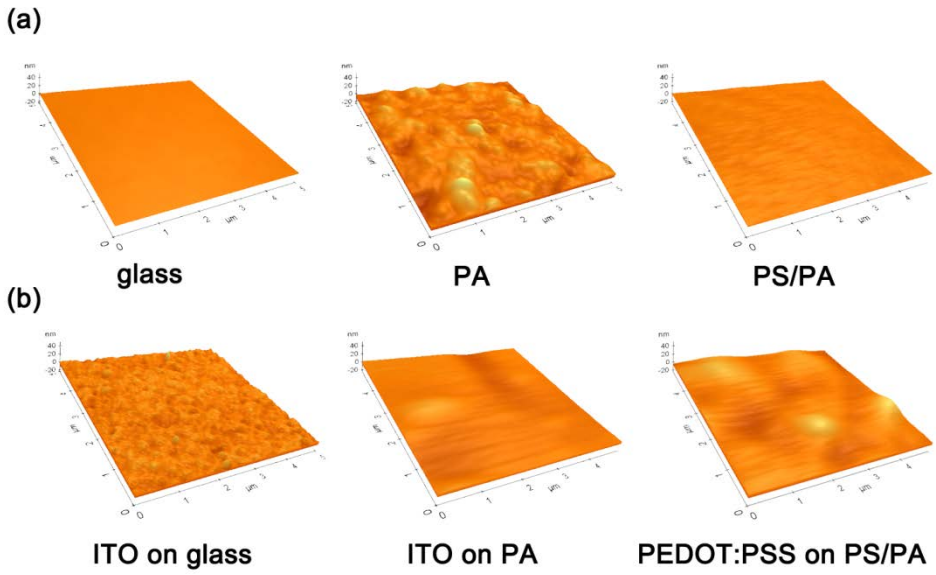

Figure 3.3 AFM images (a) substrates (glass, PA, and PS/PA) (b) ITO and PEDOT:PSS film

Substrate	R_{pv}* (nm)	RMS (nm)	Substrate	R_{pv}* (nm)	RMS (nm)
glass	0.99 ± 0.05	0.99 ± 0.05	ITO on glass	21.64 ± 7.20	1.57 ± 0.03
PA	28.78 ± 0.80	2.24 ± 0.13	ITO on PA	8.61 ± 2.03	1.20 ± 0.30
PS/PA	4.53 ± 0.27	0.67 ± 0.05	PEDOT:PSS on glass	40.53 ± 4.10	5.27 ± 0.67
			PEDOT:PSS on PS/PA	5.77 ± 1.03	1.09 ± 0.42

*R_{pv} : Peak to valley value

Table 3.1 The surface roughness of the substrates and each anode film on the glass or plastic substrate

The optical and electrical properties of the PEDOT:PSS films on the glass and plastic substrate such as thickness, sheet resistance, transmittance at

500 nm, and figure of merit (FOM) for the number of printing times are shown in **Figure 3.3**. The thickness of the PEDOT:PSS film increases and the sheet resistance decreases as the number of printing times increases. The PEDOT:PSS film on the glass substrate generally showed rougher and thicker properties than the ones on the plastic substrate for the same printing times (**Figure 3.3** (a) and **Figure 3.4**). The sheet resistance of the PEDOT:PSS film printed on the PS coated PA substrate (PS/PA) was comparable to that of the ones deposited on the glass substrate. PS was deposited on the PA substrate by the spin coating method in order to improve adhesion and wetting properties of the PEDOT:PSS film. Moreover, the PS coating layer remarkably improved the surface roughness of the plastic substrate (**Figure 3.3**). In case of the 8-time printed PEDOT:PSS film on the both glass and plastic substrate **(Figure 3.4**), the sheet resistance is 50.31 ± 2.79 Ω/□ and 45.88 ± 1.96 Ω/□ on the glass and PS/PA substrate, respectively, which is higher than that of the ITO on the glass substrate (30.13 ± 0.46 Ω/□). However, its sheet resistance is lower than that of the ITO on the PA substrate (109.17 ± 18.33 Ω/□, **Figure 3.4** (b)). The transmittance at 500 nm of the PEDOT:PSS film are shown in **Figure 3.4** (c). Moreover, the sheet resistance of the 1-time printed PEDOT:PSS (452.43 ± 12.55 Ω/□) is lower than that of the commercially utilized un-doped PEDOT:PSS (6.3×10^5 Ω/□) which is PH1000 of Clevios.[10] Since the 1-

time printed PEDOT:PSS film showed that the transmittance was much higher than that of the ITO film and similar to that of the single layer graphene which was previously reported in the **Chapter 2**, I used it as the anode of our devices. Furthermore, the PEDOT:PSS anode can be easily connected to the perimetric electronic circuits with a minimal contact resistance via multiple-time printed PEDOT:PSS bus line electrodes based on the same material, while the other electrode materials, including graphene, carbon nanotube, and transparent oxide conductor, requires additional metal electrodes, which results in undesired contact resistance between the other electrode materials and bus line electrode. In this research, I used the 8-time printed PEDOT:PSS electrodes as the bus line electrodes. It is noted that the transmittance of the 8-time printed PEDOT:PSS films on the PS/PA substrate is comparable with that of the ITO (**Figure 3.4** (c)). Therefore, I can obtain more transparent display pixels which are also the appropriate for the flexible or foldable optoelectronic applications when the PEDOT:PSS electrodes were used as both anode and bus line electrodes.

I can also use a figure of merit (FOM) to evaluate the PEDOT:PSS electrodes as the transparent and conductive electrodes. The FOM is one of the tools to evaluate a transparent electrode when the specific condition of the transmittance and conductivity are not given. The FOM is a combination of

the sheet resistance and the transmittance of the electrode which is expressed in **Equation 3.1**.[11]

Equation 3.1 $$\varphi_{TC}=T^{10}/R_s$$

where φ_{TC} is the FOM; T is the transmittance; and R_s is the sheet resistance of the electrode. Both 1- and 8- time printed PEDOT:PSS films on the PS/PA substrate showed higher FOM in comparison with the ITO film on the PA substrate (**Figure 3.4** (d)).

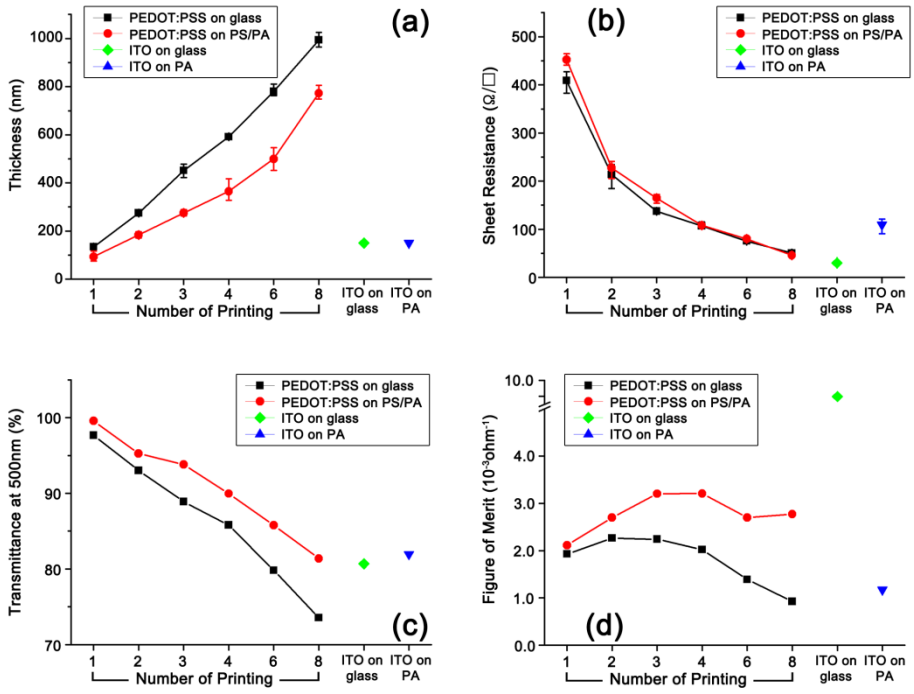

Figure 3.4 Characteristics of the PEDOT:PSS and ITO films on the glass and the plastic substrates (a) thickness (b) sheet resistance (c) transmittance at 500nm (d) figure of merit

In the inkjet printing process, a corrosion of the inkjet printer head by the strong acid was issued when the metal printer head was used. In our printer system, because the inkjet printer head was manufactured with a silicon material, it is unrestricted from the corrosion issue. However, in order to proceed to the mass production process, the nozzle clogging issue must be resolved (**Figure 3.5**)

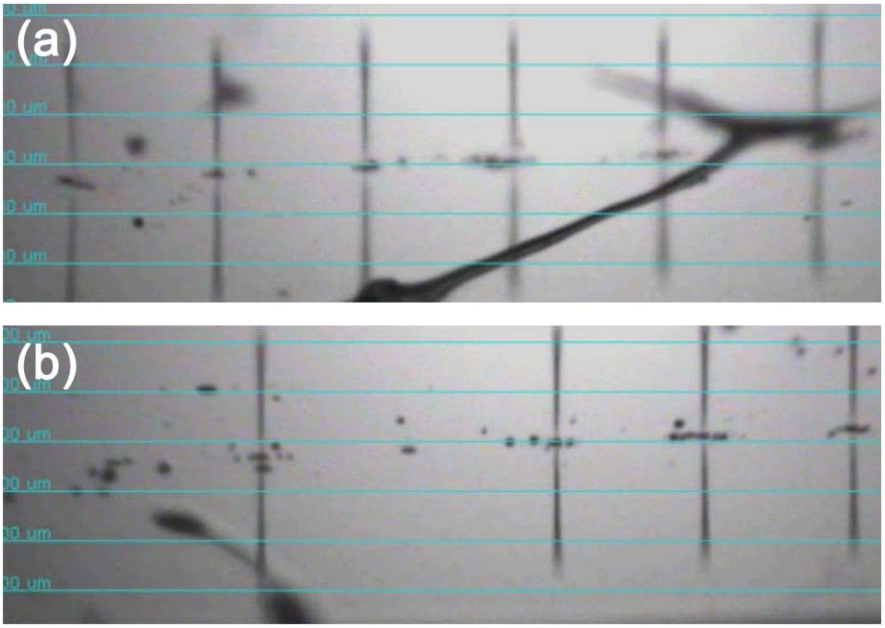

Figure 3.5 Jetting of the inkjet printer head (a) at a fresh condition (b) At a nozzle clogging status

3.3.2 Flexible Property of PEDOT:PSS

To evaluate the flexible and folding capability of the inkjet-printed PEDOT:PSS electrode, the resistance change was measured while the bending stress was applied to the PEDOT:PSS film on the PS/PA substrate and the ITO film on the PA substrate using a custom made bending machine, where one axis moves toward to the other fixed axis. Since two clamps are freely rotated, a uniform stress to the substrate is guaranteed. The moving distance is varied from 0 to 36mm, which is converted to the bending radius from 48.20 to 10.55 mm for the 40 × 20 mm^2 substrate. In case of the 24 × 20 mm^2 substrate, the bending radius is moved from 21.60 to 8.58 mm when the distance is varied from 0 to 12 mm. I also folded the substrates to evaluate their folding property. In case of the folding status, the bending radius is converted to 0.5 mm. **Figure 3.6** (a) shows our custom bending machine movements and folding status. For comparison, the resistance change of samples was monitored during the 100 bending cycles. After 100 bending cycles, the resistance of the PEDOT:PSS electrode does not change while the resistance of the ITO electrode starts to increase for the 24 mm moving distance, which is converted to 14.60 mm of the bending radius, as shown in **Figure 3.6** (b). Details of the resistance variations for each bending condition are shown in **Figure 3.7**. Even after 100 folding cycles, the resistance of the PEDOT:PSS electrode increases only by 1.184 time while the resistance of

the ITO film becomes infinitely as reported in a previous literature.[12] The resistance changes after the 100 bending and folding cycles are summarized in **Table 3.2**.

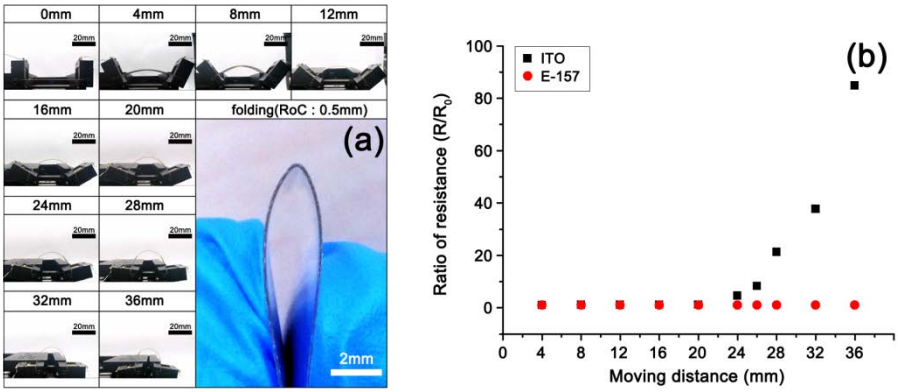

Figure 3.6 Bending and folding test (a) images of custom made bending machine (b) ratio of resistance

3.3.3 Structure of PEDOT:PSS-based PLEDs

The structure of the fabricated PLEDs is illustrated in **Figure 3.8** (a). For comparison, I fabricated four types of PLEDs: PLEDs with the ITO anodes and bus line electrodes on the glass substrate (named as ITO-glass) or the PA substrate (ITO-PA): PLEDs with the PEDOT:PSS anodes and bus line electrodes on the PS/PA substrate (PEDOT-PS/PA): PLEDs with the PEDOT:PSS anodes and Ag bus line electrodes on the PS/PA substrate

(PEDOT-Ag-PS/PA). The same organic layers (HIL and EML), the inorganic layer (LiF), and the cathode (Al) were used in all cases. **Figure 3.8** (b) shows the fabrication process of the four type's PLEDs

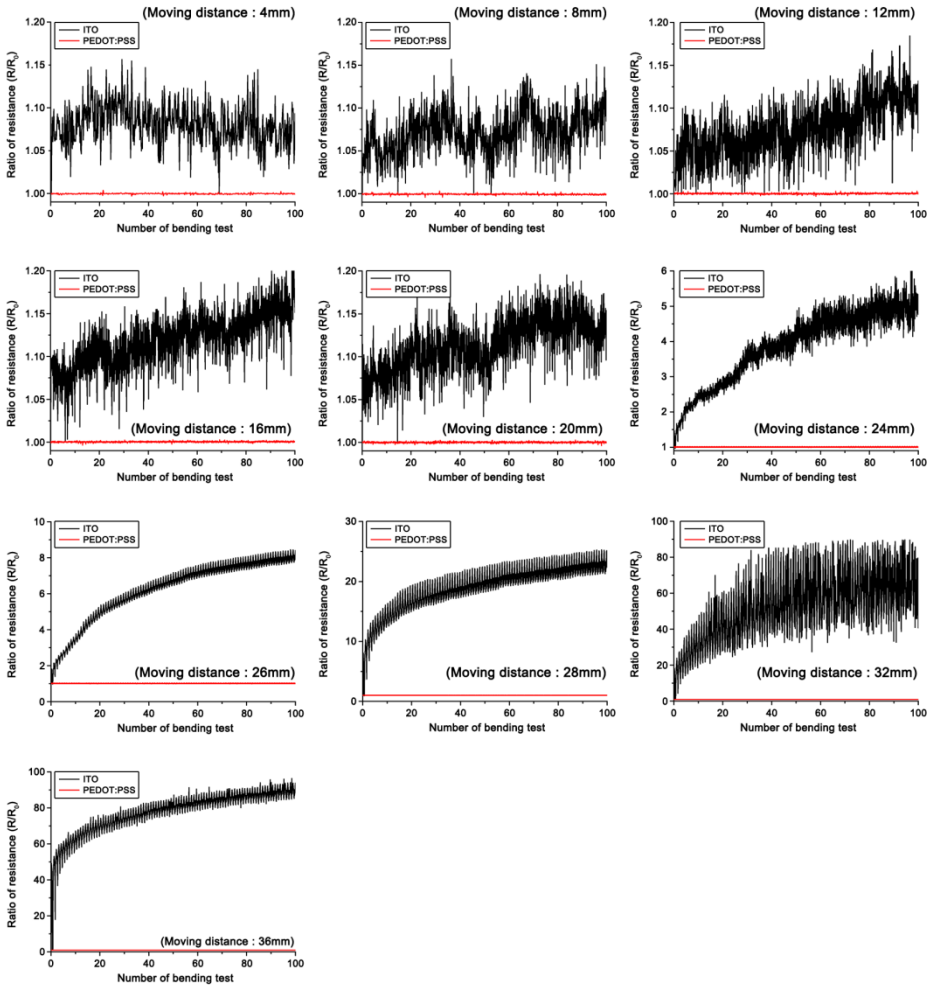

Figure 3.7 Resistance changes of ITO and PEDOT:PSS films during the bending test

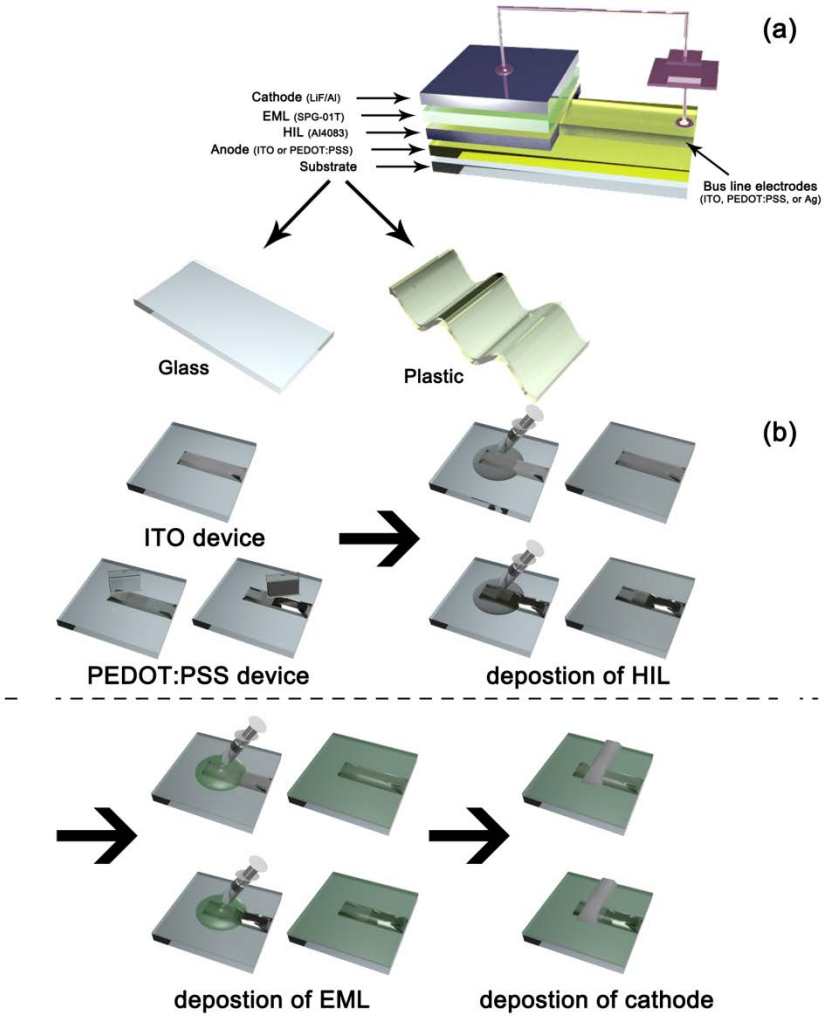

Figure 3.8 (a) Structure of PLEDs (b) fabrication process

3.3.4 Energy Level Diagram

From the graph which measured by UPS (**Figure 3.9** (a)), I could extract the work function of anodes (ITO and PEDOT:PSS, E-157) and HIL (PEDOT:PSS, AI 4083, Clevios). The work function of each layer was 4.62 eV for ITO, 5.34 eV for PEDOT:PSS anode, and 5.18 eV for PEDOT:PSS HIL, respectively. The lowest unoccupied molecular orbital (LUMO) and highest occupied molecular orbital (HOMO) levels of the EML (SPG-01T) were obtained from the manufacturer (Merck, Germany), and the work function of the EIL and cathode (LiF/Al) was referred from a previous paper.[13] The energy level diagram of the PLEDs is shown in **Figure 3.9** (b). The work function of the PEDOT:PSS anode is higher than that of the ITO anode, which resulting in the reduced hole injection barrier between the anode and the HIL. When the sheet resistance of the PEDOT:PSS electrodes is reduced by increasing the portion of the PEDOT in the PEDOT:PSS network, the work function of the high conductive PEDOT:PSS generally decreases.[14] However, the PEDOT:PSS anode, which used in the work, shows a high work function while still maintains its conductivity. Comparison data with the previously reported polymeric anodes is summarized in **Table 3.3**.

Type \ Moving distance	The ratio of Resistance (R/R_0)					
	4 mm (48.20mm)	8 mm (32.45mm)	12 mm (23.70mm)	16 mm (19.25 mm)	20 mm (16.45mm)	24 mm (14.60mm)
ITO	1.038	1.095	1.106	1.146	1.171	4.610
PEDOT:PSS	1.000	1.001	1.001	1.003	1.003	1.002

Type \ Moving distance	The ratio of Resistance (R/R_0)				
	26 mm	28 mm (13.05mm)	32 mm (11.07mm)	36 mm (10.55mm)	(0.50mm)
ITO	8.320	21.288	37.727	84.814	∞
PEDOT:PSS	1.002	1.003	1.003	1.003	1.184

Table 3.2 Resistance changes during the bending or folding cycles

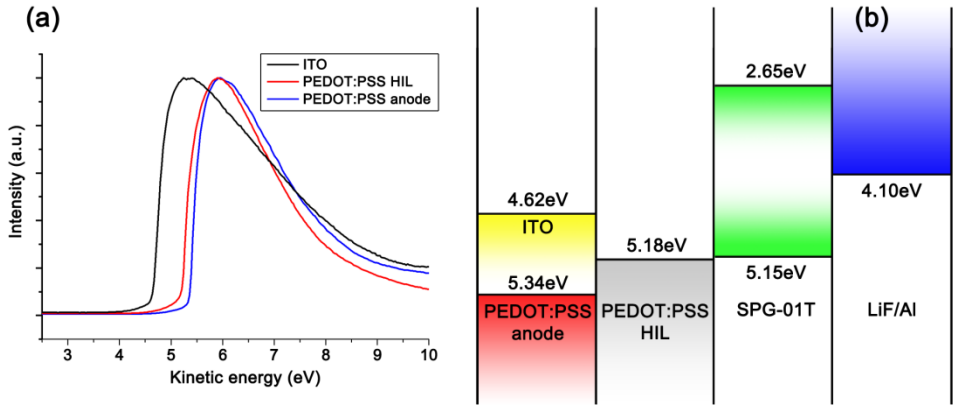

Figure 3.9 Work function (a) UPS data (b) energy level diagram

3.3.5 Characteristics of PEDOT:PSS-based PLEDs

The emissive pixel images of all devices are shown in **Figure 3.10**.

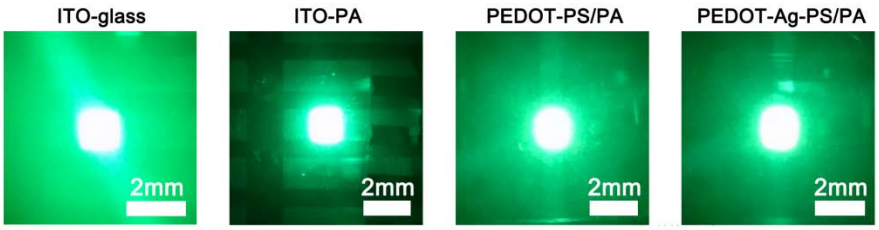

Figure 3.10 Emission pixel images

Figure 3.11 shows the measured characteristics of the four types of the PLEDs, including current density (mA/cm^2) and luminance (cd/m^2) versus voltage (V) (**Figure 3.11** (a)), and the current efficiency (cd/A) and power efficiency (lm/W) versus luminance (cd/m^2) (**Figure 3.11** (b)). ITO-glass and ITO-PA PLEDs were fabricated as the reference devices. **Figure 3.11** (a) shows that all types of the PLEDs showed similar turn-on voltages of 2.5 ~ 2.6 V, which were defined as the voltage at the luminance of 1 cd/m^2. This implies that the large electron injection barrier at the cathode dominates the light emission properties in our PLEDs, regardless of the different hole injection barriers of the ITO and the PEDOT:PSS anode. The PLEDs fabricated on the PS/PA substrates generally showed more rapid decrease of the current and power efficiencies in the high luminance levels comparing with the PLEDs on the glass substrate (**Figure 3.11** (b)) At the high current

density levels, the high sheet resistance of the PEDOT:PSS anode on the PS/PA substrate can play a key role in limiting the device performance. However, at the low luminance levels, the PEDOT-PS/PA PLEDs and PEDOT-Ag-PS/PA PLEDs showed much better performance even than the ITO-glass PLEDs due to the high work function and high transmittance of the PEDOT:PSS anode (**Figure 3.11** (b)). It is noted that the PEDOT-PS/PA PLEDs show almost the same performances comparing with the PEDOT-Ag-PS/PA PLEDs, which indicates that the performance of the 8-time inkjet-printed PEDOT:PSS bus line electrodes is similar to that of the Ag bus line electrodes. Therefore, the PEDOT:PSS electrodes can be used for the interconnection lines between the anode and the outer circuit lines. Furthermore, I think that the PEDOT:PSS electrodes can replace the opaque interconnection lines in a typical pixel of the OLED displays considering the relatively high transmittance of the 8-time inkjet-printed bus line electrodes and thus, they can be used to implement more transparent sub pixels. Details of the performance values for the four types PLEDs are summarized in **Table 3.3**.

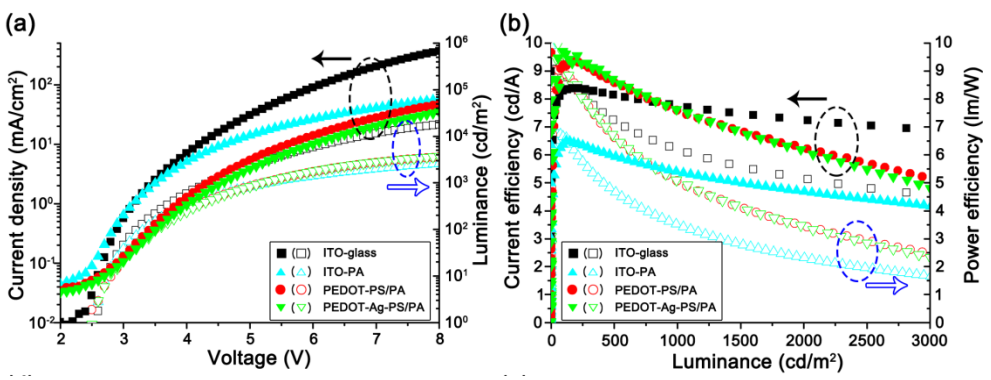

Figure 3.11 Characteristics of four types PLEDs (a) IVL curve (b) efficiency curve

In addition to the higher performances, the PEDOT-PS/PA PLEDs showed much better flexibility comparing with the ITO-PA PLEDs as shown in **Figure 3.12** after the 100 bending and folding cycles. The bending stress test of 10 mm bending radius and the folding stress test of 0.5 mm bending radius were performed for both PEDOT-PS/PA PLEDs and ITO-PA PLEDs. After the bending stress test, the ITO-PA PLEDs showed the decreased current and luminance values and lower efficiencies due to the increased resistance of the ITO bus line electrodes. At the large current levels, the device which composed of ITO anodes and bus line electrodes failed to operate, and its luminance were obtained just up to the region of 1,000 cd/m^2 as shown in **Figure 3.12** (b). When the folding stress test was applied to the ITO-PA PLEDs, the device failure was immediately observe (**Figure 3.13**), which was apparently from the infinite resistance of the ITO anode as shown

in **Table 3.2**. In other hand, the PEDOT-PS/PA PLEDs showed very small changes in their performance after the bending and folding stress tests. In the inset of **Figure 3.12** (c), the real operating device images are shown, where there are passive matrix pixel array of 2 × 5.

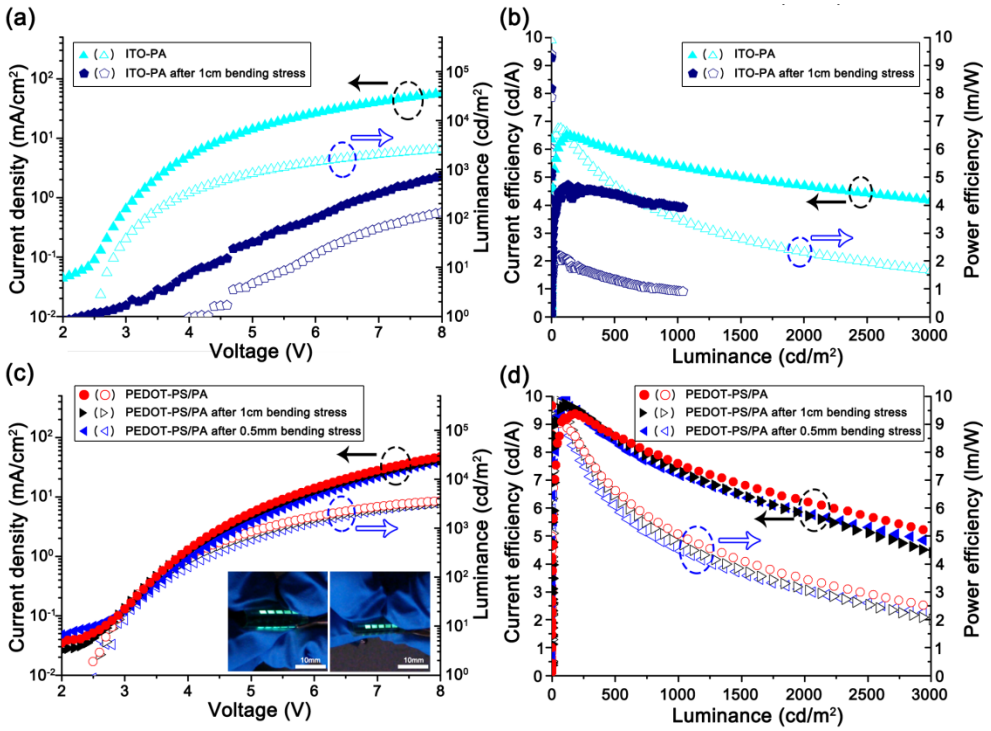

Figure 3.12 Characteristics of flexible PLEDs (a) IVL curve of ITO-PA PLEDs (b) efficiencies of ITO-PA PLEDs (c) IVL curve of PEDOT-PS/PA PLEDs (d) efficiencies of PEDOT-PS/PA PLEDs

Device label	Device	Main PEDOT:PSS	Additive	Substrate	Method	Reference
1-1	PLEDs [1]	PEDOT:PSS (Con-tech)	nMP [3], NMF [4]	glass	Inkjet printing	this work
1-2				PS [9] / PA		
2	sm-OLEDs [2]	PH500 (Baytron)	DMSO [5]	glass	Lift-up	Ref. 1
3	PLEDs	PV4071 (Baytron)	EG [6]	glass	Spin-coating	Ref. 2
4	sm-OLEDs	PH1000 (Heraeus)	EG	glass	Spin-coating	Ref. 3
5	sm-OLEDs	Baytron P	glycerol	glass	Spin-coating	Ref. 4
6	sm-OLEDs	PEDOT:FTS (Baytron)	DMAc [7]	PES [10]	Spin-coating	Ref. 5
7	PLEDs	EL_P3020 (Agfa)	-	glass	Inkjet printing	Ref. 6

Device label	Conductivity (S/cm or Ω/□)	Transmittance [11] (% at 500nm)	FOM ($10^{-3}/\Omega^{-1}$)	Work Function (eV)		Reference
				PEDOT:PSS	ITO	
1-1	40~450 Ω/□	73.6~97.7 %	1.15~2.62	5.34	4.62	this work
1-2	46~452 Ω/□	81.4~99.6%	2.70~3.21			
2	-	-		5.0	4.5~4.7	Ref. 1
3	160 S/cm	-		-	-	Ref. 2
4	93~209 Ω/□	84.4~88.9 % [12]		5.0	4.8	Ref. 3
5	1850 Ω/□	~90 %		5.0	-	Ref. 4
6	130~390 Ω/□	52~87 %		4.67	4.7	Ref. 5
7	290 Ω/□	-		5.02		Ref. 6

Device label	Von	Max. effi. (PEDOT:PSS)		Max. Brightness* (cd/m^2)	Reference
		lm/W	cd/A		
1-1	2.5~2.7 V	5.74 lm/W	5.71 cd/A	6,956	this work
1-2		5.80 lm/W	5.58 cd/A	6,032	
2	4~4.2 V	-	2.23 cd/A	2,500	Ref. 1
3		-	1.20 cd/A	500	Ref. 2
4		-	-	-	Ref. 3
5		0.70 %	-	700	Ref. 4
6		-	1.75 cd/A	4,500	Ref. 5
8		-	1.20 cd/A	3,000	Ref. 6

1) PLEDs (polymer light emitting diodes) 2) sm-OLEDs (small molecules organic light emitting diodes) 3) nMP (n-methyl-2-pyrrolidone)
4) nMF (n-methylformamide) 5) DMSO (dimethylsulfoxide) 6) EG (Ethylene glycol) 7) DMAc (N,N-dimethylacetamide)
8) PA (polyarylite) 9) PS (polystyrene) 10) PES (polyethersulfone) 11) without substrate 12) at 550nm
* The data was determined from the graphs in the paper.

Table 3.3 Comparison table with previous reports

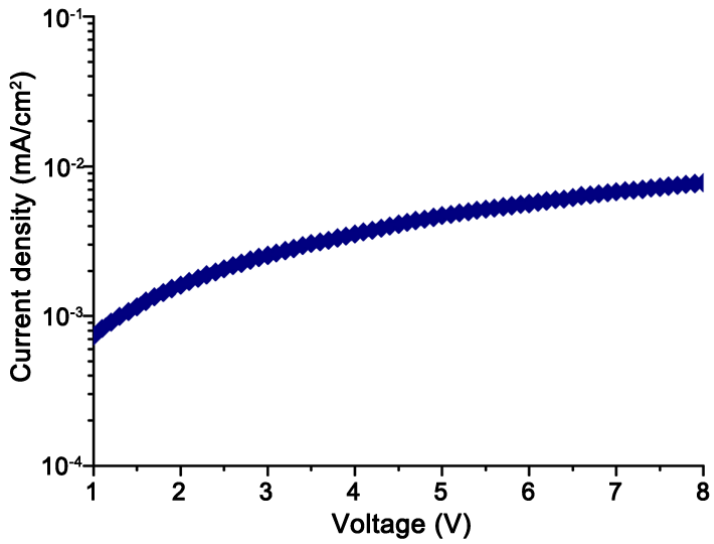

Figure 3.13 IV characteristics of ITO-PA PLEDs after the folding stress test

When the flexible test is applied to the ITO-PA PLEDs, the maximum luminance of the ITO-PA PLEDs is decreased due to the increased the sheet resistance of the ITO film. Moreover, the current and power efficiencies are also decreased after the bending stress is applied. The decreased efficiencies are caused by the broken ITO films (**Figure 3.14**) because the broken ITO film brings about the defects at the interface between ITO anode and organic layer.

In **Table 3.3**, the properties of the PEDOT:PSS electrodes (anodes and bus line electrodes) and the PEDOT-PS/PA PLEDs are compared with data which were previously reported. Although the conductivity is similar to the value from the other literatures, the work function and transmittance of

the PEDOT:PSS electrodes in this work are higher than those of the other PEDOT:PSS films, resulting in the high device efficiencies.

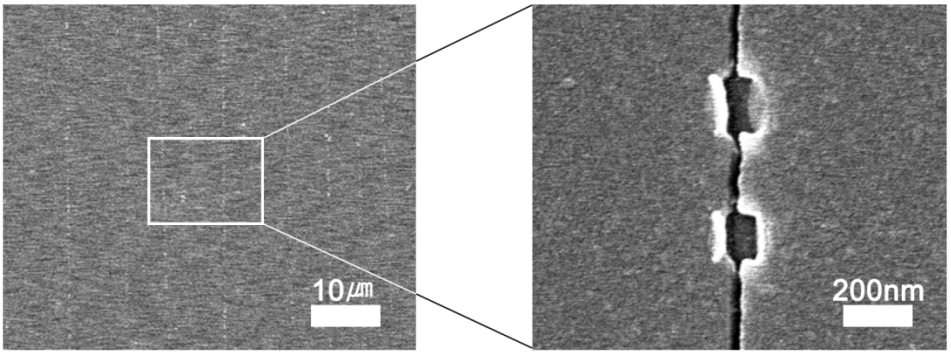

Figure 3.14 Broken ITO film after the bending stress is applied

3.4 Summary

I selectively printed the same PEDOT:PSS ink for the anodes and the bus line electrodes with the inkjet printer for the flexible PLED array applications. NMP and NMF doping material can enhance the conductivity of the PEDOT:PSS electrodes without losing their optical property. The inkjet-printed PEDOT:PSS films showed the excellent performance during the bending and folding stress condition. The fabricated PEDOT-PS/PA PLEDs well demonstrated the promising future application of the selectively printed polymeric transparent electrodes, which can be the key technology for the flexible, transparent and potentially stretchable optoelectronic devices.

References

[1] C. Piliego, M. Mazzeo, B. Cortese, R. Cingolani, G. Gigli, *Org. Electron.***9**, 401 (2008)

[2] J. Ouyang, C.-W. Chu, F.-C. Chen, Q. Xu, Y. Yang, *Adv. Funct. Mater*. **15**, 203 (2005)

[3] Y. H. Kim, J. Lee, S. Hofmann, M. C. Gather, L. Müller-Meskamp, K. Leo. *Adv. Funct. Mater*. **23**, 3763 (2013)

[4] W. H. Kim, A. J. Mäkinen, N. Nikolov, R. Shashidhar, H. Kim, Z. H. Kafafi, *Appl. Phys. Lett*. **80**, 3844 (2002)

[5] M. Kim, Y. S. Lee, Y. C. Kim, M. S. Choi, J. Y. Lee, *Syn. Metals* **161**, 2318 (2011)

[6] Y. Yoshioka, P. D. Calvert, G. E. Jabbour, *Macromol. Rapid Commun*. **26**, 238 (2005)

[7] W.-Y. Chou, S.-T. Lin, H.-L. Cheng, M.-H. Chang, H.-R. Guo, T.-C. Wen, Y.-S. Mai, J.-B. Horng, C.-W. Kuo, F.-C. Tang, C.-C. Liao, C.-L. Chiu, *Thin Solid Films* **515**, 3718 (2007)

[8] W. Zhang, B. Zhao, Z. He, X. Zhao, H. Wang, S. Yang, H. Wu, Y. Cao, *Energy Envion. Sci* **6**, 1956 (2013)

[9] Y. Hong, J. Kanicki, *IEEE Trans. Electron. Dev*. **51**, 1562 (2004)

[10] K. Lim, S. Jung, S. Lee, J. Heo, J. Park, J.-W. Kang, Y.-C. Kang, D.-G. Kim, *Org. Electron.* **15**, 1849 (2014)

[11] G. Haacke, *J. Appl. Phys*. **47**, 4086 (1976)

[12] S. Bae, H. Kim, Y. Lee, X. Xu, J.-S. Park, Y. Zhng, J. Balakrishnan, T. Lei, H. R. Kim, Y. I. Song, Y.-J. Kim, K. S. Kim, B. Özyilmaz, J.-H. Ahn, B. H. Hong, S. Iijima, *Nature Nanotech.* **5**, 574 (2010)

[13] S. Y. Park, C. H. Lee, W. J. Song, C. Seoul, *Curr. Appl. Phys*. **1**, 116 (2001)

[14] N. Koch, A. Elschner, J. P. Rabe, R. L. Johnson, *Adv. Mater*. **17**, 330 (2005)

Chapter 4 Flexible PLEDs with photonic crystal structures for high efficient devices

4.1 Introduction

OLEDs have been extensively investigated in recent years because of their potential applications in TVs, mobile displays, and solid state lightings. In the OLEDs research area, its efficiency has been one of the most significant topics, which is related to a power consumption of the device. Although its internal quantum efficiency has been reached almost 100% by using phosphorescent materials, the external quantum efficiency was usually limited to only 20% because a lot of portion of generated lights were captured and decayed into the wave guided mode and glass guided mode.[1-2] The external quantim efficiency is a ratio of the total number of photons generated by the emissive layer to the number of charges injected into a

device. The external quantim efficiency η_{ext} is related to the internal quantum efficiency η_{int} and the light output coupling factor χ by the following **Equation 6-1**,[3-4]

Equation 4.1 $$\eta_{ext} = \eta_{int} \cdot \chi = \gamma \times r_{st} \times q \times \chi$$

In the expression, γ is the charge balance factor of electron and hole, r_{st} is the ratio of singlet and triplet, and q is the luminescent efficiency. For the larger incidence angles than a critical total internal reflection angle, a half of the generated lights are propagated in the anode/organic layer and organic/organic layers, which called the wave guided mode, and 30% of the generated lights are trapped inside the glass substrate, which called the glass guided mode (**Figure 4.1**).[2]

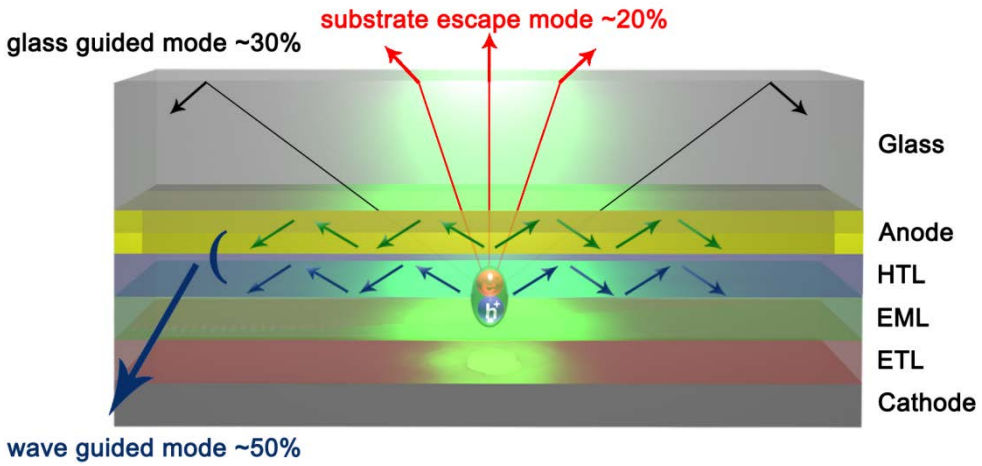

Figure 4.1 Schematic of OLED structure and optical ray diagram of light propagation with various modes including wave guided mode, glass guided mode and substrate escape mode

To overcome the low outcoupling efficiency of OLEDs, various interal and external device modification techniques have been introduced such as substrate modifications,[5-6] texturing the meshed structures,[7-8] insulting scattering mediums,[9-10] micro lens arrays,[11-12] micro-cavity structures,[13-14] nanowires,[15-16] buckling structures,[17-18] and photonic crystal structures.[19-23] The photonic crystal (PC) structures are usually fabricated on the rigid substrate, and then OLEDs, which is consisted with two electrode and organic functional layers, were fabricated on the PC structures. Although the OLEDs with PC structures showed the improved external quautum effieicncy, previous reports dealing with PC structures utilized a rigid substrate such as glass or quartz.[19-23] Moreover, PC structures embedded OLEDs required a complicated fabrication process including an additional planarization process using chemical vapor deposition (CVD) [19-20] or using solution-based materials [21-23] for flat surfaces, anode deposition process, and photolithography process for patterning the anode. Recently, Donghyun Kim and I reported the polymer light-emitting diodes (PLEDs) with the solution-processed gallium-doped zinc oxide (GZO) anode without any additional planarization process.[23] In our previous report, though the planarization layer was not necessary, too many coating processes to obtain enough conductivity of GZO were required, and the photolithography process to pattern the GZO anode was also necessary.

Moreover, the GZO film was easily damaged by the poly(3,4-ethylenedioxythiophene):poly(styrenesulfonate) (PEDOT:PSS) due to the strong acid of PEDOT:PSS, which was utilized as a hole injection layer.[24-25] In the **Chapter 2**, I reported a solution processable polymeric anode on the flexible substrate.

Therefore, in this **Chapter 4**, I report the flexible PLEDs with highly conductive and transparent polymeric anodes deposited by an inkjet printing process on the plastic PC structures. A solution-processed transparent conductive polymeric anode has several advantages in comparison with the vaccum process and our previous report including simple process to obtain the patterned anode, low fabrication costs, and smoothening of PC structures.[19-23] The flexible PLEDs with embedded PC structures and polymeric anodes showed an enhancement by a factor of 1.31 and 1.28 in comparison with the normal PLEDs for a current and power efficiency at 979 cd/m^2, respectively. In addition, although ghost images of the PC structures embedded OLEDs are a obstacle to apply the display applications, its diffraction patterns of the emitted light is one of the advantages to apply to the solid state lighting applications.

4.2 Experiments

4.2.1 Fabrication of 2D Nano Hole Arrays

For the fabrication of two dimensional (2D) photonic crystal structures, a conventional laser holographic lithography was used on the SiNx/quartz and the SiN_x/PA substrate. Before the coating of a negative photoresist, an chrome (Cr) hard mask was deposited by an e-beam evaporation method. After the deposition of Cr hard mask and negative photoresist, the substrates were exposed to the He-Cd laser (IK3301R-G, Kimmon Koha) two times in orthogonal direction in the holography system. After developing of the negative photoresist, the substrates were etched by a reactive-ion-etching (RIE 80 plus). The 2D nano hole arrays were obtained after removing Cr hard mask with Cr etchant.

4.2.2 Preparation of Anode Substrate

A silicon nitride (SiN_x) film was deposited on the polyarylite (PA) plastic substrate under 200℃ by the chemical vapor deposition (CVD) in case of the flexible substrate. On the rigid quartz substrate, a SiN_x film was deposited at 200℃ in the CVD chamber. The PEDOT:PSS anode was deposited by the inkjet printer (Dimatix, USA) using a 10 pico-liter cartridge,

which has the drop speed of 8 m/s. The inkjet printing process was conducted at the room temperature without heating. After the printing process, PEDOT:PSS films were baked on the hot plate at 120℃ for 1 hour. The Ag bus electrode was deposited on the PEDOT:PSS anode by the inkjet printing process, which has the drop speed of 9 m/s. Then, the printed Ag bus electrode was annealed on the oven at 120 ℃ for 20 minutes.

4.2.3 Measurements

The refractive index of the PEDOT:PSS film was measured by a spectroscopic ellipsometer (M-2000UI, J. A. Wollam). The other measurements and device fabrication process can be referred to the experiments section of the previous **chapters**.

4.3 Results and Discussion

4.3.1 Laser Holographic Lithography

The several methods to fabricate 2D PC structures have been introduced such as nanoimprint lithography,[21, 26-27] phase mask lithography,[28-29] nanosphere lithography,[30-31] and laser holographic lithography.[19-20, 22-23] In this **Chapter 4**, the laser holographic lithography was utilized to fabricate 2D nano hole arrays using He-Cd laser and interferometer setup by exposing two times in orthogonal direction (**Figure 4.2**). In the laser holographic lithography, a period of 2D hole arrays can be modulated by controlling the incident angle by following **Equation 6.2**,

Equation 4.2 $$\Lambda = \frac{\lambda}{2 \sin \theta}$$

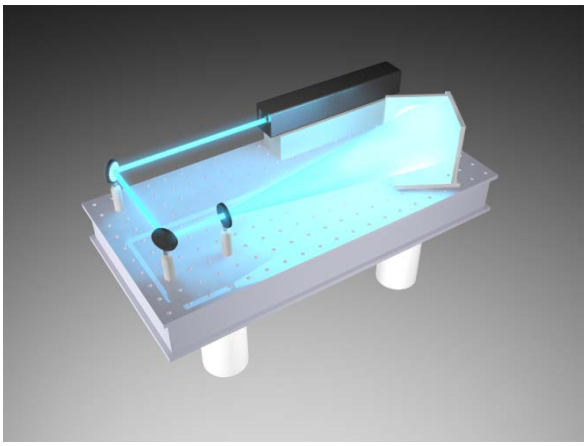

Figure 4.2 Laser holography setup

In the **Equation 4.2**, Λ is the period of PC structures, λ is the wavelength of a laser, and θ is an incident angle of light. In order to obtain large period patterns, the small incident angle should be applied. To fabricate short period patterns, the incident angle should be enlarged (**Figure 4.3**). In our experiment, the period and the incident angle of 2D nano hole arrays were 400 nm and 24˚, respectively.

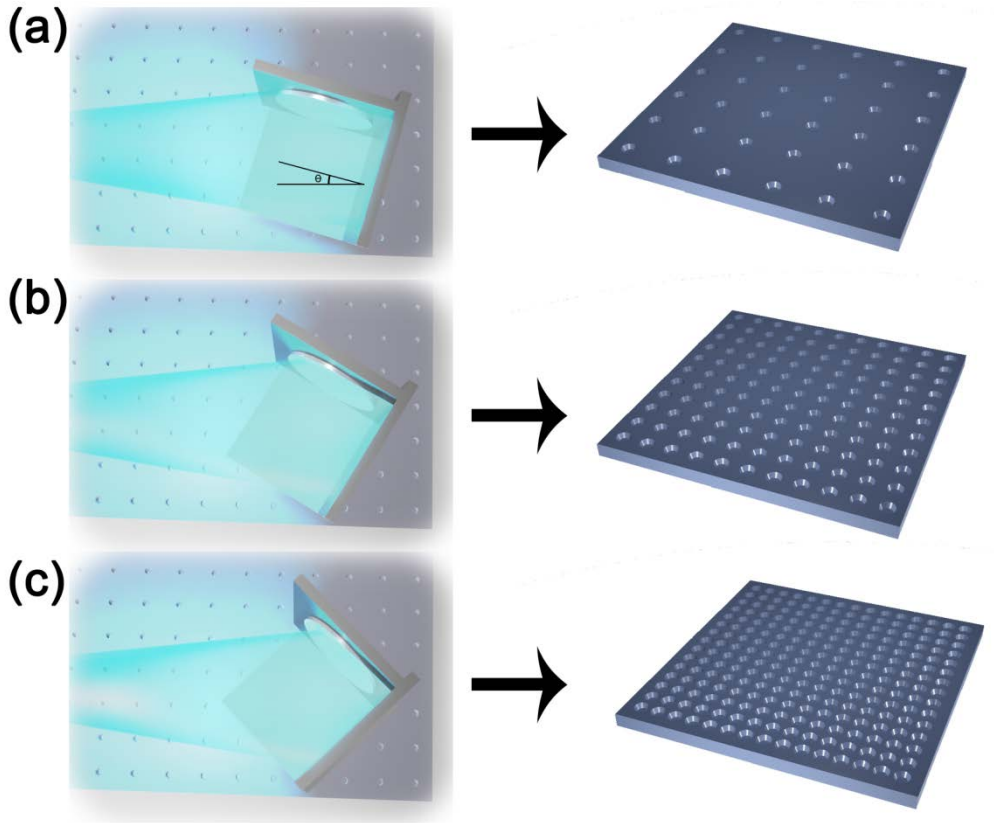

Figure 4.3 Laser holographic lithography (a) for large period (b) for middle period (c) for short period

4.3.2 Device Fabrication Process

In order to fabricate a conventional PC structures embedded OLEDs, too complicated processes were necessary. **Figure 4.4** shows a general fabrication process of the conventional PC structures.

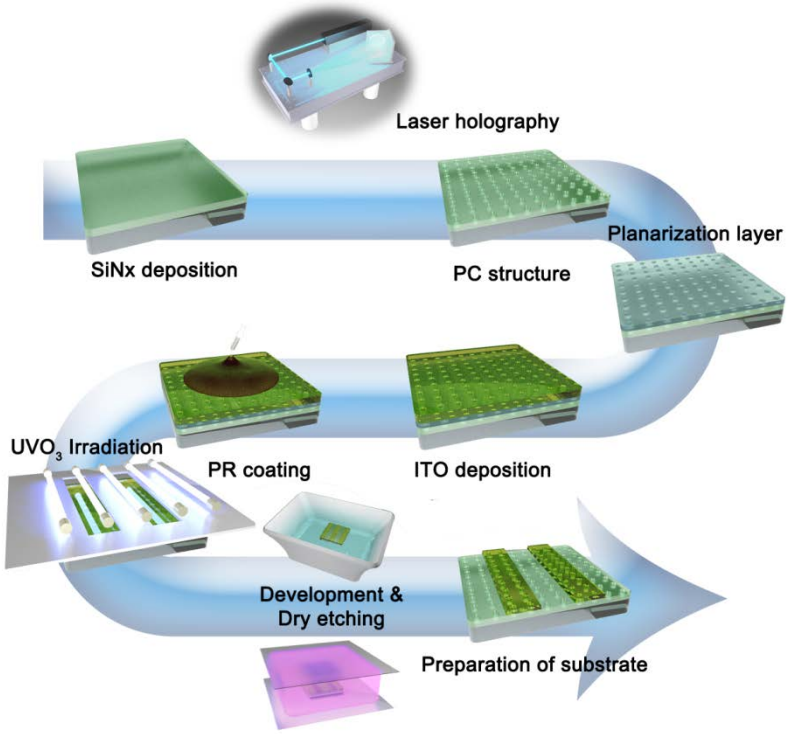

Figure 4.4 Conventional process for the anode preparation

First of all, the high index material was deposited on the substrates by a chemical vapor deposition (CVD). Then, the fabrication process of PC structures was followed. To obtain relatively flat surface for the anode deposition, another planarization layer was necessary. Then, several

processes were followed such as an anode deposition, photolithography for a patterning of anode including photoresist coating, baking, UVO_3 radiation with a photomask, development, and etching process. On the other hands, in our experiments, the preparation of the anode substrate can be simplified with our new conductive polymeric anode and inkjet printer (**Figure 4.5**).

After the fabrication of 2D nano hole arrays, the patterned anode was easily obtained by just 1-time inkjet printing and annealing process. **Figure 4.6** shows the fabrication process of PLEDs after the preparation of anode substrate.

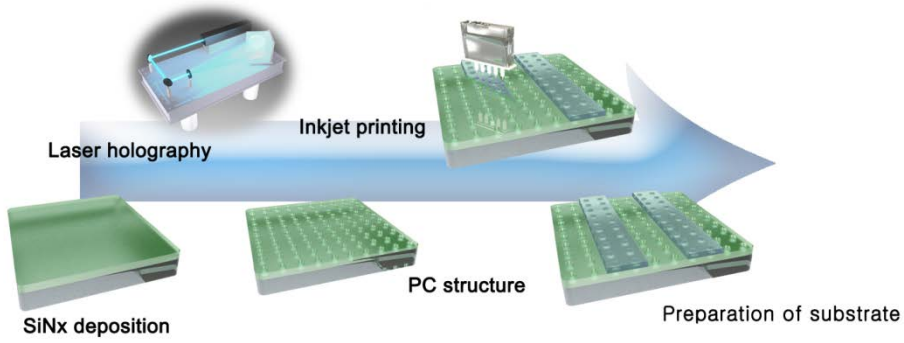

Figure 4.5 Simple process with an inkjet printing method

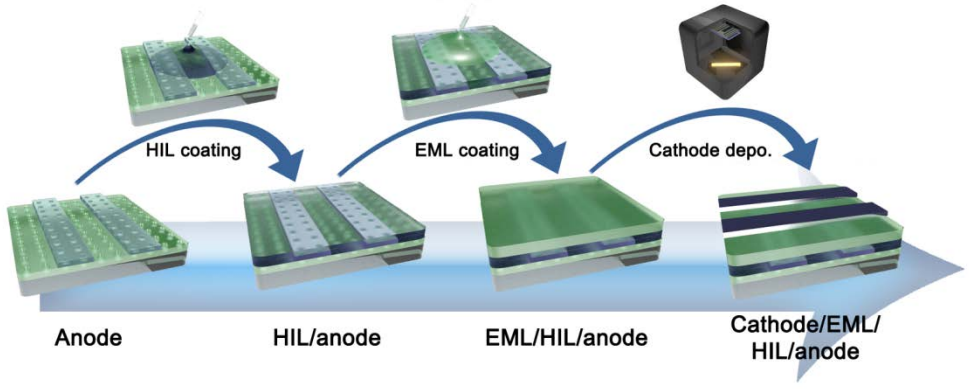

Figure 4.6 Fabrication process of the PLEDs

4.3.3 Structure of the Devices

Figure 4.7 (a)~(c) shows the cross sectional or top views of scanning electron microscope (SEM) images of the normal PEDOT:PSS PLEDs on a quartz substrate (PEDOT-Quartz PLEDs). The PEDOT:PSS anode has a smooth surface roughness, and is composed with small grains. From the cross sectional SEM images of the PEDOT-Quartz PLEDs (**Figure 4.7** (c)), each layer such as anode, organic layer, and cathode can be easily detected. The PEDOT:PSS for anode and the another PEDOT:PSS for HIL has similar morphology, and thus it is difficult to separate each layer in the cross sectional SEM image (**Figure 4.7** (c)).

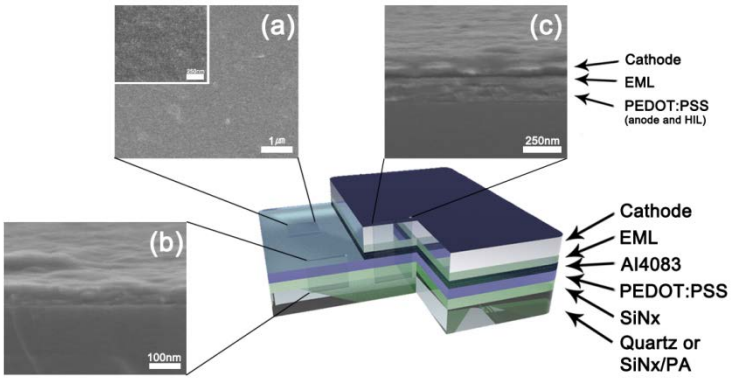

Figure 4.7 Structures of the PLEDs (a) top images of the PEDOT:PSS anode (b) cross sectional image of the PEDOT:PSS anode (c) cross sectional image of the normal PLEDs

Figure 4.8 (a)~(b) shows the 2D nano hole arrays in the SiNx layer, which has a period of 400 nm, a hole size of 196 ± 60 nm, and a hole's depth of 184 ± 22 nm. After the deposition of the PEDOT:PSS anode, the 2D nano hole arrays were covered with the PEDOT:PSS film except for the center of nano holes. In the top view (**Figure 4.8** (c)), the nano hole arrays were almost covered, however, the center region of each hole has void, which results in the slightly rugged anode surface. Moreover, the nano hole arrays were not totally filled with the PEDOT:PSS film. The air pockets in the nano hole arrays were formatted, which was the intermediate of the Cassie-Baxter and Wenzel state (**Figure 4.8** (d)).[32]

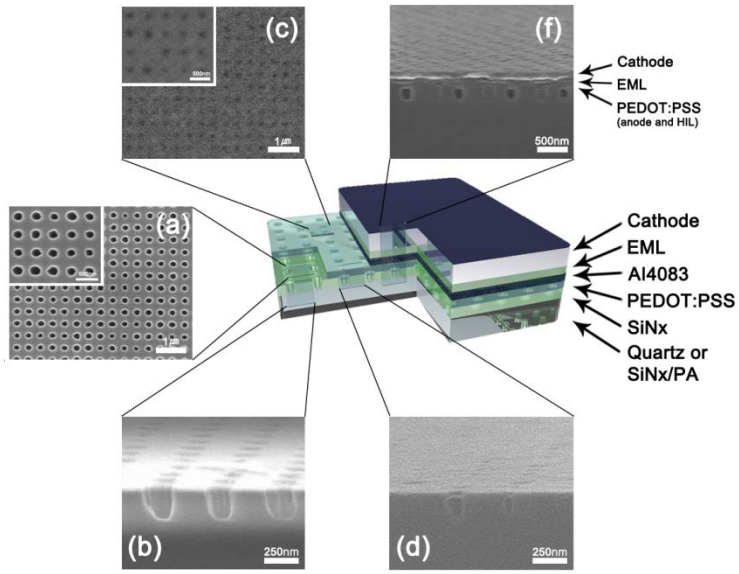

Figure 4.8 Structures of the PLEDs (a) top images of the 2D nano hole arrays (b) cross sectional image of 2D nano hole arrays (c) top images of the PEDOT:PSS anode on the 2D nano hole arrays (d) cross sectional image of the PEDOT:PSS anode on the 2D nano hole arrays (e) cross sectional image of the PC structures embedded PLEDs

Even after the deposition of organic layers and cathode, the air space and the corrugation surface on the top region were maintained (**Figure 4.8** (e)). The photo images of the PC structures embedded anode substrates and the reference anode substrates are shown in **Figure 4.9** (a) and (b). **In Figure 4.10**, the photo image of the PC structures embedded PLED fabricated on the plastic substrate is shown, which shows the holographic patterns.

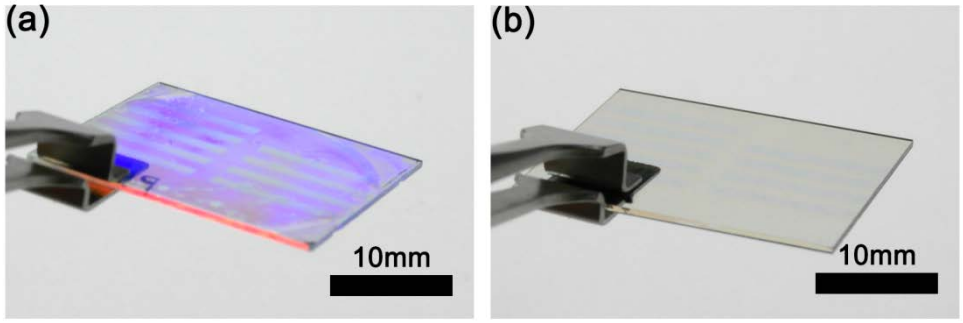

Figure 4.9 Optical image (a) PC structures embedded anode substrate (b) normal anode substrate

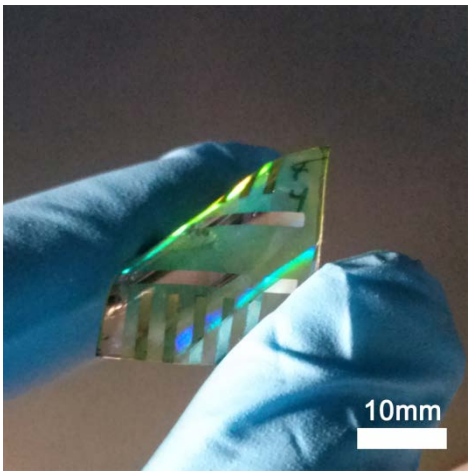

Figure 4.10 Optical image of PC structures embedded PLEDs on the plastic substrate

4.3.4 Properties of the PEDOT:PSS film

The transmittance of the PEDOT:PSS anode on the plastic substrate and substrates was measured with a spectrophotometer (**Figure 4.11** (a)). The deposition of a SiN_x film on the PA substrate leads to lower its transmittance. However, the transmittance of the SiN_x/PA substrate with the PEDOT:PSS film is higher than that of the SiN_x/PA substrate at the 500 nm, which is the main peak position of PLEDs.

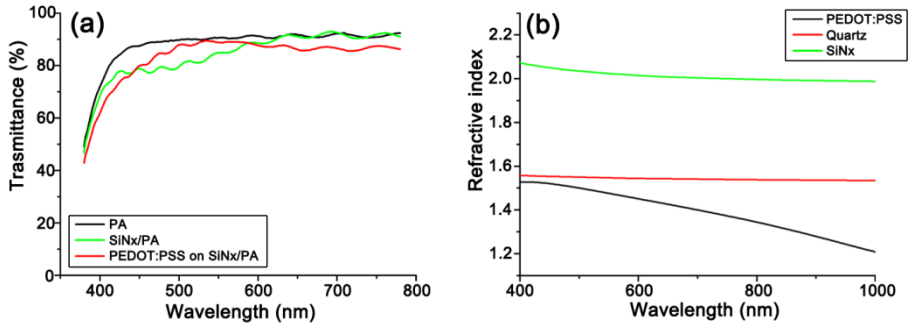

Figure 4.11 Properties of the PEDOT:PSS anodes (a) transmittance (b) refractive index

The refractive index of materials which used in this work is important because the extraction of the generated lights in the OLEDs is proportional to the difference of the refractive index. The refractive index of the PEDOT:PSS film was measured by an ellipsometer, and the refractive index of the other materials were referred to the previous paper and refractive index library.[33-34] The refractive index of the PEDOT:PSS, quartz, SiNx and air

at 500 nm are 1.50, 1.55, 2.03, and 1.00, respectively (**Figure 4.11** (b)). The difference of the refractive index between SiN_x and air is 1.03, and its difference between SiN_x and PEDOT:PSS is 0.53. On the other hands, the difference of the refractive index between PEDOT:PSS and quartz is just 0.05. In order to maximize the extraction efficiency of the generated lights in our devices, the PEDOT:PSS was selected as the anode material and SiN_x films was utilized as the base material of the PC structures.

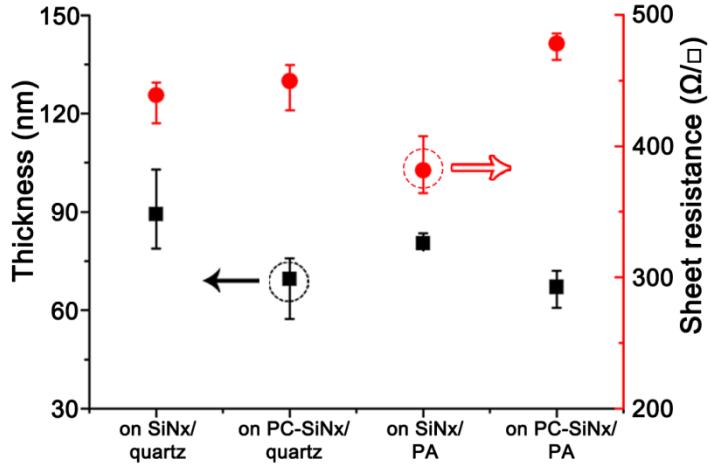

Figure 4.12 Thickness and sheet resistance of the PEDOT:PSS anodes

Figure 4.12 shows the geometrical and electrical properties of the PEDOT:PSS films on the normal substrate (SiN_x/quartz) and PC structures embedded substrate (PC-SiN_x/quartz). The thickness of the PEDOT:PSS film on the SiN_x/quartz is higher than that of the PEDOT:PSS film on the PC-SiN_x/quartz. Unlike the trend of thickness, the sheet resistance of the

PEDOT:PSS film on the PC-SiN_x/quartz is similar to that of the PEDOT:PSS film on the SiNx/quartz. This trend can be understood from **Figure 4.8** (d). Some portion of the PEDOT:PSS film on the PC-SiN_x/quartz filled the inlet of the nano holes. As much as the amount of the PEDOT:PSS which filled the nano holes, the thickness of the PEDOT:PSS film on the PC-SiNx/quartz was decreased. However, the conductive path of the PEDOT:PSS film does not changed regardless of the shape of the substrate. The thickness and the sheet resistance of PEDOT:PSS films on the rigid and plastic substrates are summarized in **Table 4.1**.

	thickness (nm)	sheet resistance (Ω/□)
PEDOT:PSS on SiNx/quartz	89.3 ± 13.7	438.9 ± 21.4
PEDOT:PSS on PC-SiNx/quartz	69.6 ± 12.3	449.7 ± 22.2
PEDOT:PSS on SiNx/PA	80.4 ± 3.1	381.4 ± 26.2
PEDOT:PSS on PC-SiNx/PA	67.1 ± 4.9	478.2 ± 12.2

Table 4.1 Properties of the PEDOT:PSS film

4.3.5 Characteristics of the PLEDs

To evaluate the effectiveness of the PEDOT:PSS anodes in the PC structures embedded PLEDs, I fabricated two types of devices on the rigid substrate. One was a reference device which was fabricated on the SiN_x/quartz substrate (PEDOT-SiN_x/quartz), and the other one was fabricated

on the PC-SiN_x/quartz substrates (PEDOT-PC-SiN_x/quartz). Although the current density of the PEDOT:PSS-PC-quartz PLEDs is slightly lower than that of the PEDOT:PSS-quartz (**Figure 4.13** (a)), the luminance of the PEDOT-PC-SiN_x/quartz PLEDs (4,117 cd/m^2 at 7 V) is higher than that of the reference device (3,839 cd/m^2 at 7 V), which shows the enhanced extraction efficiency of the generated lights due to the PC structures. The current and power efficiencies of the PEDOT-PC-SiN_x/quartz PLEDs are higher than those of the reference device, which are enhanced by a factor of 1.21 and 1.16 in the vicinity of 1,000 cd/m^2, respectively (**Figure 4.13** (b)).

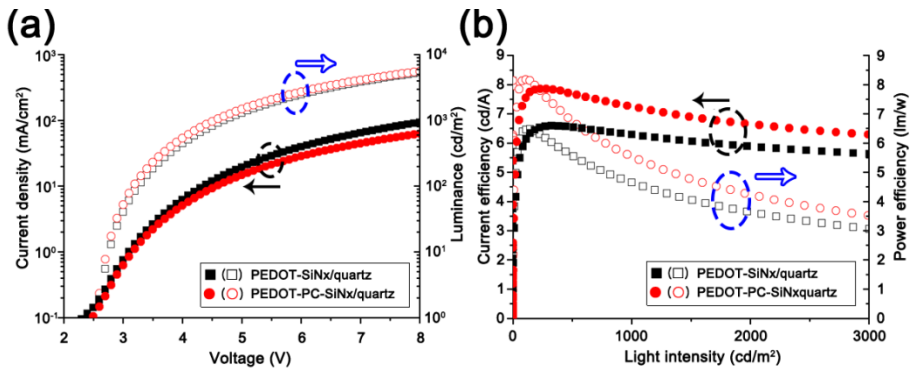

Figure 4.13 Characteristics of the PLEDs (a) I-V-L characteristics of the PLEDs on the quartz substrate (b) current and power efficiency of the PLEDs on the quartz substrate

In order to fabricate the flexible PC structures embedded PLEDs, I fabricated two devices. One was the reference device which was fabricated

on the SiN_x/PA substrate (PEDOT-SiN_x/PA), and the other was fabricated on the PC structures embedded plastic substrate (PEDOT-PC-SiN_x/PA). In **Figure 4.14** (a), the current density of the PEDOT-SiN_x/PA PLEDs is much higher than that of PEDOT:PSS-PC-SiN_x/PA, which is due to the lower sheet resistance. In case of the plastic substrate, the difference of the anode's sheet resistance is higher than that of the rigid substrate (**Table 4.1**). However, the luminance of the PEDOT-PC-SiNx/PA PLEDs is similar to that of the reference device, which shows that the PC structures embedded PLEDs fabricated on the plastic substrate has the similar enhancement to the PC structures embedded PLEDs on the rigid substrate. In the efficiency graph (**Figure 4.14** (b)), the current and power efficiencies of the PLEDs fabricated on the plastic substrate can be enhanced with an introduction of the PC structures by a factor of 1.37 and 1.37 in the maximum current efficiency and power efficiency, and 1.31 and 1.28 in the vicinity of 1,000 cd/m^2, respectively. Details of the performance data for the all PLEDs are summarized in **Table 4.2**. Even after the flexible test with the bending radius of 1 cm which was implemented with the custom made bending machine, most of the characteristics of the PC structures embedded PLEDs, including the current density, luminance, current efficiency and power efficiency, were not changed, which shows that the PC structures embedded PLEDs can be applied to the flexible optoelectronic applications. The photo image of the PC

structures embedded PLEDs which operated at 2 mA was shown in inset of **Figure 4.14** (a).

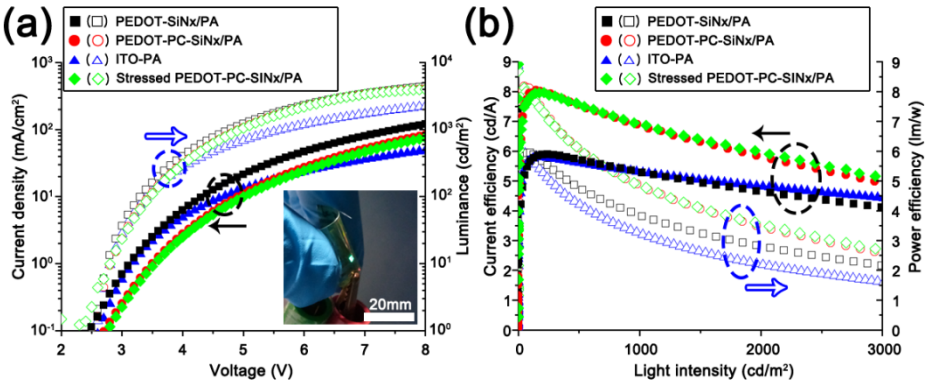

Figure 4.14 Characteristics of the PLEDs (a) I-V-L characteristics of the PLEDs on the SiNx/PA substrate, inset shows the emission devices with a bending stress (b) current and power efficiency of the PLEDs on the SiNx/PA substrate

The real operating pixel image operated at 7 V which was composed 4 × 4 arrays are shown in **Figure 4.15** (a) and (b). In the PEDOT-SiNx/quartz PLEDs, the lights were only observed on the pixel area. However, in the PEDOT-PC-SiN_x/quartz PLEDs, the generated lights were observed not only on the pixel area but also on the middle area of each pixel. These diffraction patterns were one of the obstacles when the PC structures were applied to the display applications. However, when the PC structures embedded PLEDs were applied to the lighting applications, the ghost images, which appeared in the middle of each pixel, can be one of the advantages to increase the

emission efficiency. The ghost images can be also observed in the device on the rigid substrate which was composed of 2 × 4 arrays (**Figure 4.16** (a) and (b)). In case of the flexible device, the diffracted lights of the PLEDs which operated at 2 mA can also be observed (**Figure 4.17** (a) and (b)).

This ghost image is one evidence of the enhanced outcoupling efficiency of our PLEDs having two dimensional photonic crystal structures because the generated photons suppressed at the interface can easily escape the device. (**Figure 4.18**, [35]) The outcoupling efficiency can be more increased when the difference of the refractive index is higher.

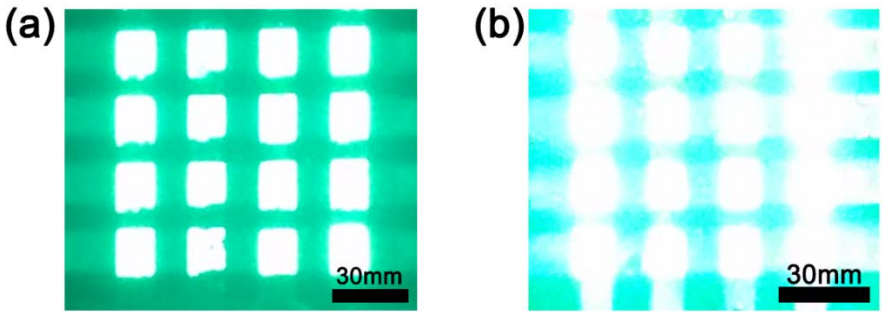

Figure 4.15 Characteristics of the PLEDs (a) emission image of the normal PLEDs on the quartz substrate (4×4 arrays) (b) emission image of the PC structures embedded PLEDs on the quartz substrate (4×4 arrays)

device	turn-on voltage	maximum efficiency		efficiencies around 1,000 cd/m^2		
	(V)	cd/A	lm/W	cd/A	lm/W	cd/m^2
PEDOT-SiNx/quartz	2.60	6.59	6.48	6.29	4.65	1,002
PEDOT-PC-SiNx/quartz	2.60	7.86	8.18	7.28	5.61	964
ITO-PA	2.60	5.80	5.93	5.28	3.20	1,025
PEDOT-SiNx/PA	2.60	5.89	5.95	5.28	3.81	1,021
PEDOT-PC-SiNx/quartz	2.60	8.04	8.18	6.91	4.90	979
Streesed PEDOT-PC-SiNx/PA	2.60	7.97	8.13	6.86	4.77	1,053

Table 4.2 Characteristics of the PLEDs

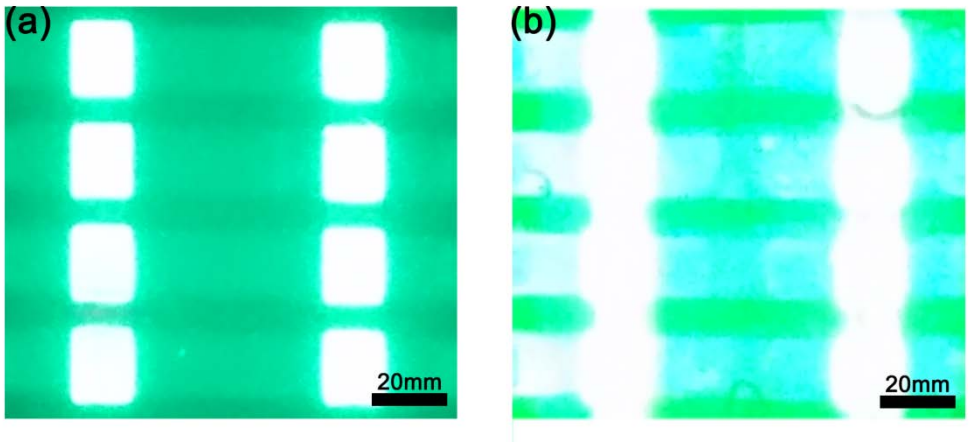

Figure 4.16 Emission images (a) the 2 × 4 arrays of the normal PLEDs on the SiNx/quartz substrate (b) the 2 × 4 arrays of the PC structures embedded PLEDs on the SiNx/quartz substrate

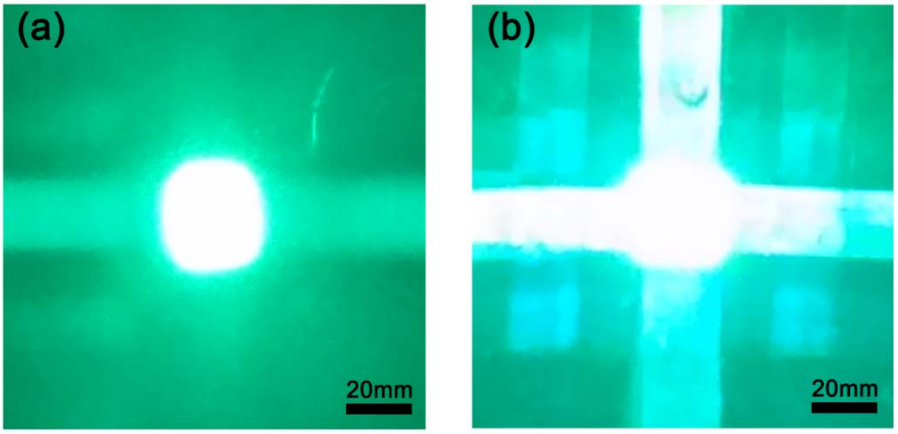

Figure 4.17 Emission images (a) 1 pixel of the normal PLEDs on the SiNx/PA substrate (b) 1 pixel of the PC structures embedded PLEDs on the SiNx/PA substrate

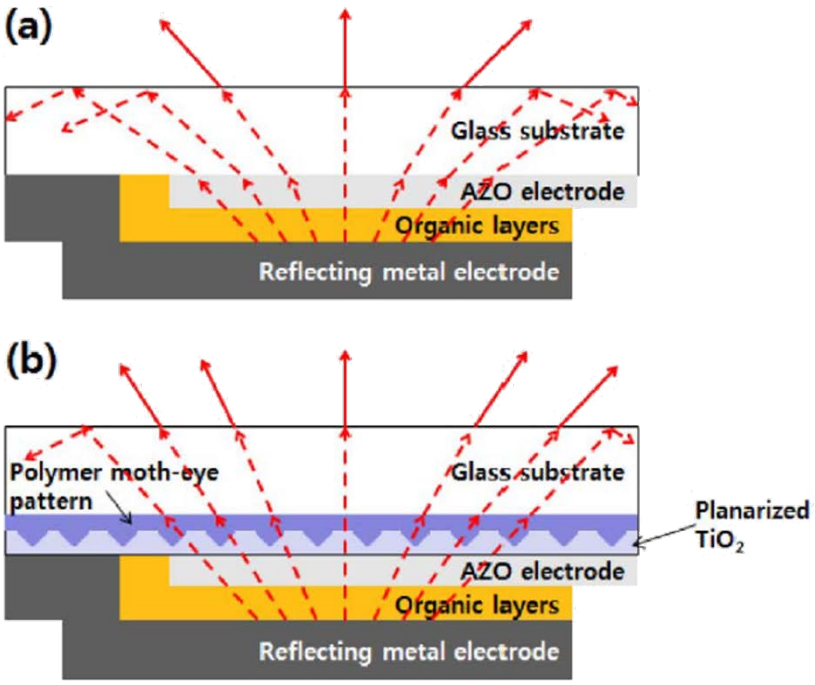

Figure 4.18 Schematics of light extractin for (a) a normal device (b) an OLED having the photonic crystal structures

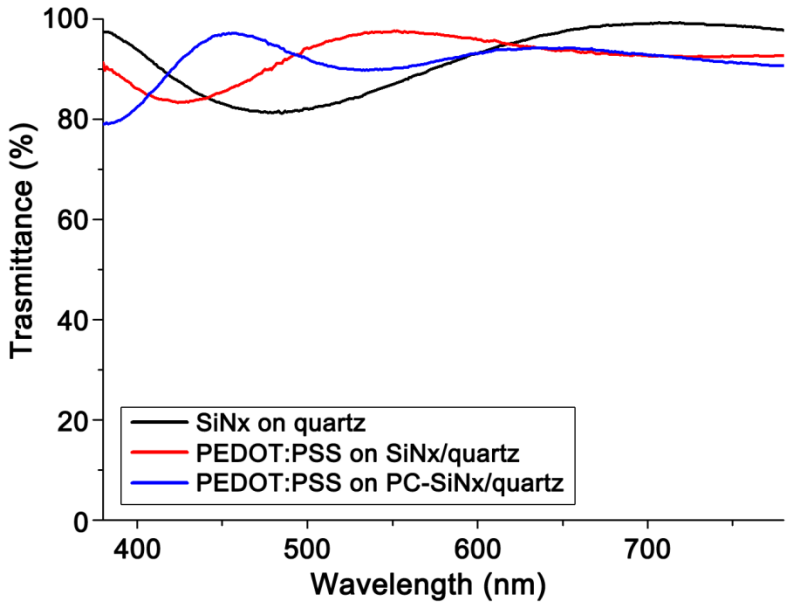

Figure 4.19 Transmittance of the anodes and the substrates

Figure 4.19 shows the transmittance of the PEDOT:PSS anodes on the PC structures or normal substrate, and the transmittance of the SiN_x/quartz substrate. At the 500 nm region, the PEDOT:PSS films on the PC-SiN_x/quartz and SiN_x/quartz substrate have much higher transmittance than the SiN_x/quartz substrate. At the 450 nm region, the PC structures embedded substrate has the highest transmittance among these samples. As the concept of the PC structures embedded PLEDs for highly efficient lighting applications, I fabricated two type's PLEDs, PC structures embedded PLEDs and normal PLEDs, which have the main peak at 500 nm. When I fabricate

the PLEDs which have the main peak at 450 nm, or when I tune the proper period of the PC structures for the highest efficiency at the 450 nm, it can be fabricated more efficient lighting devices.

4.4 Summary

I fabricated the flexible photonic crystal (PC) structures embedded PLEDs. I deposited the PEDOT:PSS materials for the anode with the inkjet printing process. The inkjet-printed PEDOT:PSS electrodes played a key role to smoothen the PC structures and to apply to the anode in the PLEDs at the same time. The PC structures embedded PLEDs have the higher emission efficiency and maintain the excellent performance under the flexible test. The fabricated PC structures embedded PLEDs well demonstrated the promising solid state lighting applications with the printed PEDOT:PSS anodes

References

[1] C. Adachi, M. A. Baldo, M. E. Thompson, S. R. Forrest, *Appl. Phys. Lett*. **90**, 5048 (2001)

[2] G. Gu, D. Z. Garbuzov, P. E. Burrows, S. Venkatesh, S. R. Forrest, *Opt. Lett*. **22**, 396 (1997)

[3] N. K. Patel, S. Cinà, J. H. Burroughes, *IEEE J. Select. Top. Quant. Electron*. **8**, 346 (2002)

[4] S. R. Forrest, D. D. C. Bradley, M. E. Thompson, *Adv. Mater*. **15**, 1043 (2003)

[5] B. W. D'Andrade, J. J. Brow, *Appl. Phys. Lett*. **88**, 192908 (2006)

[6] C. F. Madigan, M.-H. Lu, J. C. Sturm, *Appl. Phys. Lett*. **76**, 1650 (2000)

[7] Y.-H. Cheng, J.-L. Wu, C.-H. Cheng, K.-C. Syao, M.-C. Lee, *Appl. Phys. Lett*. **90**, 091102 (2007)

[8] J. M. Ziebarth, A. K. Saafir, S. Fan, M. D. McGehee, *Adv. Funct. Mater*. **14**, 451 (2004)

[9] T. Yamasaki, K. Sumioka, T. Tsutsui, *Appl. Phys. Lett*. **76**, 1243 (2000)

[10] J. J. Shiang, T. J. Faircloth, A. R. Duggal, *J. Appl. Phys*. **95**, 2889 (2004)

[11] S. Möller, S. R. Forrest, *J. Appl. Phys*. **91**, 3324 (2002)

[12] M.-K. Wei. I.-L. Su, *Opt. Exp*. **12**, 5777 (2004)

[13] S.-H. Cho, Y.-W. Song, J.-G. Lee, Y.-C. Kim, J. H. Lee, J. Ha, J.-S. Oh, S. Y. Lee, S. Y. Lee, K. H. Hwang, D.-S. Zang, Y.-H. Lee, *Opt. Exp*. **16**, 12632 (2008)

[14] T.-Y. Cho, C.-L. Lin, C.-C. Wu, *Appl. Phys. Lett*. **88**, 111106 (2006)

[15] S. Coskun, E. S. Ates, H. E. Unalan, *Nanotech*. **24**, 125202 (2013)

[16] Z. Yu, Q. Zhang, L. Li, Q. Chen, X. Niu, J. Liu, Q. Pei, *Adv. Mater*. **23**, 664 (2011)

[17] W. H. Koo, S. M. Jeong, F. Araoka, K. Ishikawa, S. Nishimura, T. Toyooka, H. Takezoe, *Nat. Photonics* **4**, 222 (2010)

[18] B. Park, H. G. Jeon, *Opt. Exp*. **19**, A1117 (2011)

[19] Y. R. Do, Y.-C. Kim, Y.-W. Song, Y.-H. Lee, *J. Appl. Phys.* **96**, 7629 (2004)

[20] Y.-J. Lee, S.-H. Kim, J. Huh, G.-H. Kim, Y.-H. Lee, S.-H. Cho, Y.-C. Kim, Y. R. Do, *Appl. Phys. Lett*. **82**, 3779 (2003)

[21] H.-H. Cho, B. Park, H.-J. Kim, S. Jeon, J.-H. Jeong, J.-J. Kim, *Appl. Opt*. **49**, 4024 (2010)

[22] Y.-C. Kim, S.-H. Cho, Y.-W. Song, Y.-J. Lee, Y.-H. Lee, Y. R. Do, *Appl. Phys. Lett*. **89**, 173502 (2006)

[23] D. Kim, J. Ha, J. Park, J. Hwang, H. Jeon, C. Lee, Y. Hong, *Org. Electron. Submitted*

[24] D.-K. Lee, J. Bang, M. Park, J.-H. Lee, H. Yang, *Thin Solid Films* **518**, 4046 (2010)

[25] H. Zheng, X. L. Du, Q. Luo, J. F. Jia, C. Z. Gu, Q. K. Xue, *Thin Solid Films* **515**, 3967 (2007)

[26] S. H. Kim, K.-D. Lee, J.-Y. Kim, M.-K. Kwon, S.-J. Park, *Nanotech.* **18**, 055306 (2007)

[27] S. H. Ahn, L. J. Guo, *ACS Nano* **3**, 2304 (2009)

[28] Y. Lin, P. R. Herman, K. Darmawikarta, *Appl. Phys. Lett*. **86**, 071117 (2005)

[29] D. Shir, E. C. Nelson, Y. C. Chen, A. Brzezinski, H. Liao, P. V. Braun, P. Wiltzius, K. H. A. Bogart, J. A. Rogers, *Appl. Phys. Lett*. **94**, 011101 (2009)

[30] H. Fredriksson, Y. Alaverdyan, A. Dmitriev, C. Langhammer, D. S. Sutherland, M. Zäch, B. Kasemo, *Adv. Mater*. **19**, 4297 (2007)

[31] S. Han, Z. Hao, J. Wang, Y. Luo, *J. Vac. Sci. Technol. B* **23**, 1585 (2005)

[32] D. Murakami, H. Jinnai, A. Takahara, *Langmuir* **30**, 2061 (2014)

[33] H. R. Philipp, *J. Electrochem. Soc*. **120**, 295 (1973)

[34] PV Lighthouse website, http://www.pvlighthouse.com.au/, accessed: September (2014)

[35] J. H. Kim, L.-M. Do, J.-H. Choi, J. Park, H. Lee, *Opt. Lett*. **38**, 3773 (2013)

Chapter 5 Analysis with Impedance Spectroscopy

5.1 Introduction

Impedance spectroscopy (IS) measurements and analysis enable us to model the simple equivalent circuit of OLEDs.[1-6] In literature, the IS analysis has been mainly conducted on a small molecule-based OLEDs which composed with tris(8-hydroxyquinolinato)aluminium (Alq_3) deposited by a thermal evaporation.[1-4, 6-7] On the other hands, there are few reports which carried out the IS measurements on the polymer light-emitting diodes (PLEDs),[5, 8-9] although PLEDs have been attracted much interest due to their easy solution process, low fabrication costs, and potential applications for the flexible and printable optoelectronic devices.[10] Moreover, the IS analysis of the PLEDs using the conductive polymeric anode as the electrode material has not been extensively carried out.

In this **Chapter 5**, I studied PLEDs which fabricated with a conductive polymeric anode (PEDOT:PSS) deposited by an inkjet printing process, and I designed the equivalent circuit of the PEDOT:PSS-based PLEDs with the IS analysis. Furthermore, I investigated devices with different anode materials, ITO and PEDOT:PSS, and I studied the usefullness of a hole injection layer (PEDOT:PSS, AI4083, Clevios, Germany) and Ag bus line electrodes with the IS measurements. Moreover, I studied the relationship between the efficiency of the devices and the IS parameters with PLEDs which had different efficiencies.

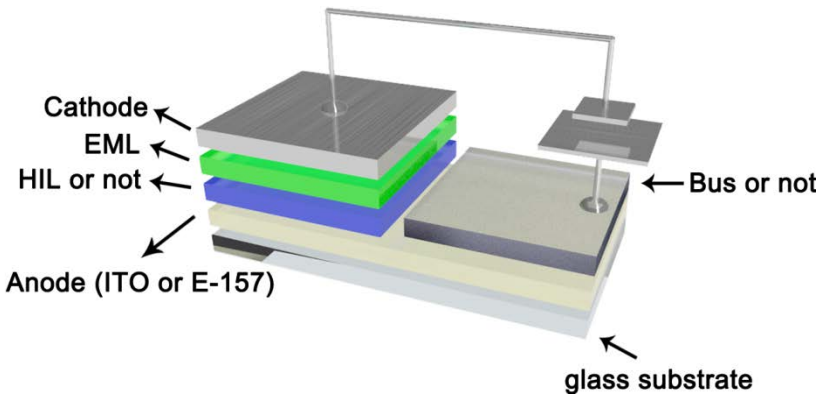

Figure 5.1 Schematic image of the device

5.2 Experiments

To conduct the IS measurements and IS analysis of PLEDs, the five devices were fabricated. Device 1 is a reference device (PEDOT:PSS anode with Ag bus electrode / AI 4083 (hole injection layer, HIL) / SPG-01T (green emitting polymer (EML), Merck) / LiF (electron injection layer) / Al (cathode)). Our PEDOT:PSS anode is a new transparent and conductive polymer, which was supplied from Con-Tech (Korea). PEDOT:PSS was utilized as the anode material in this work. Ag electrode was used as a bus line electrode in order to reduce a voltage drop between a pad electrode and a pixel anode. The PEDOT:PSS anode and Ag bus electrode were deposited by the inkjet printing process (Dimatix, USA). HIL and EML were deposited by a spin-coating process. LiF and Al were deposited in a vacuum chamber by a thermal evaporation. Device 2 is the device without HIL to figure out the usefulness of HIL (PEDOT:PSS anode with Ag bus electrode / SPG-01T / LiF / Al). In device 3, the Ag bus line electrode was eliminated (PEDOT:PSS anode without Ag bus electrode / AI 4083 / SPG-01T / LiF / Al). In device 4, the anode material was replaced by indium tin oxide (ITO) (ITO / AI 4083 / SPG-01T / LiF / Al). Device 5 is the ITO-based devices without HIL (ITO / SPG-01T / LiF / Al). All devices were fabricated on the glass substrate, and the schematic image is shown in **Figure 5.1**. The detailed process can be referred to the experiment in the **Chapter 2**.

The impedance spectroscopy measurements were conducted with a LCR precision meter (E4980A, Agilent). The amplitude of small signal was 100 mV, and the frequency was swept from 100 Hz to 1 MHz.

5.3 Effectiveness of HIL and Bus Electrodes

5.3.1 Characteristics of PLEDs

Figure 5.2 (a) and (b) shows the measured electrical and optical characteristics of the five types of PLEDs, including current density (mA/cm^2) and luminance (cd/m^2) versus applied voltages, and current efficiency (cd/A) and power efficiency (lm/W) versus luminance (cd/m^2). Device 1 and 4 were used as the reference devices. ITO-based reference device (device 4) has the highest current and luminance value in the space charge limited current (SCLC) region (> 5.0 V) among 5 devices due to the low sheet resistance of the ITO. In the off-region (< 2.5 V), the current densities of the devices without HIL (device 2 and 5) are higher than those of the reference devices (device 1 and 4) nevertheless of the anode materials. This high off-current is based on the easy movement of mobile charges in the EML to the anode due to the absence of the resistive layer (HIL). In case of device 3, the current density is similar to that of device 1 in the off-region. However, the current level in the SCLC region of the device without Ag bus electrode is lower than the reference device (device 1) because of the IR drop. Moreover, the off current levels of the PEDOT:PSS-based device (device 1) are higher than that of ITO device (device 4), which is resulted from the lower hole injection barrier of the PEDOT:PSS anodes. The turn-on voltages of all devices are

located in 2.5 ~ 2.6 V, which was defined as the voltage at the 1 cd/m^2. The efficiencies of the PEDOT:PSS-based PLEDs (device 1) are 3.95 cd/A and 3.25 lm/W at 991 cd/m^2, respectively, which are about 93.6 % of the current efficiency of the ITO-based PLEDs (device 4) at 971 cd/m^2. Device 3, which does not include the Ag bus line electrode, has 87.3% of the efficiency of the reference device 1, and the devices without HIL show the lower efficiencies than the devices with HIL. Especially, the current efficiency of the ITO-based device without HIL (device 5) shows the lowest value, which is about 24.4% of the ITO-based device with HIL (device 4). In the devices without HIL, a lot of holes are easily injected to the EML, which leads to a shift of a recombination zone to the cathode, which brings out the exciton quenching. Moreover, the injected electron from the cathode does not stay at the interface of EML and HIL, but leaves to the anode, which results in the lower charge balance of electron and hole. Due to the exciton quenching and low charge balance, the efficiencies of the devices without HIL are lower than those of the reference devices.

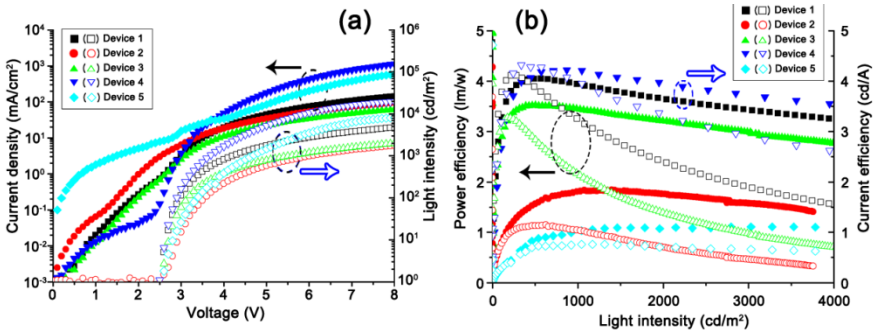

Figure 5.2 (a) IVL characteristics (b) power and current efficiencies

Figure 5.3 shows the plots of a normalized resistance as a function of frequency for all devices, which operated at 5.0 V. A positive derivative (dR/df) in the normalized resistance versus frequency plots indicates a negative capacitance (NC) at 10^2 Hz~10^4 Hz ranges in the all devices.[2] The NC is related with the interface trap filling and the accumulated space charge.[3, 11]

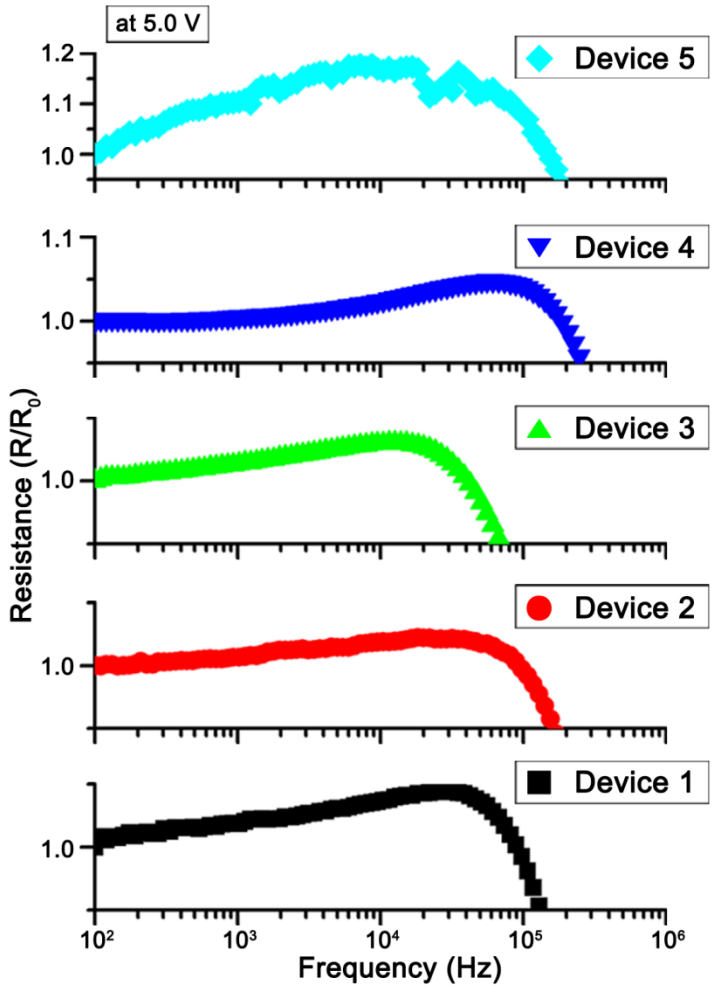

Figure 5.3 Normalized resistance versus frequency (R-F plots)

5.3.2 Reference Device

Cole-Cole plots of device 1 are shown in **Figure 5.4** (a), which operated at 0.0 ~ 5.0 V with 1 V step. Each solid line represents the fitted impedance values which obtained from the IS analysis, and each dot shows the measurement data. The diameters of the semi-circle decrease in accordance

with an increasing operating voltage, which is due to a total resistance decrease of the PLEDs. In the M plots (**Figure 5.4** (b)), the diameters of the left semi-circle are increased by an increasing voltages although the characteristics of the right semi-circle are not almost changed. It implies that the impedance value of one specific layer, which represents the right semi-circle, does not changed evidently although that of another layer, which represents the left semi-circle, is changed with the applying voltage. The relaxation frequency of devices is defined as the frequency when the value of differentiation is zero in the bode plots (**Figure 5.4** (c)). This relaxation frequency moves to the right direction when the applied voltage increases (**Figure 5.4** (c)). To extract the parameters, the equivalent circuit which composed of a single series resistance (R_s) and two parallel RC circuits (R_1-C_1 and R_2-C_2) was modeled (**Figure 5.5**). The series resistance (R_s) can be extracted from the Cole-Cole plots at the high frequency region (**Figure 5.6**).[12] Device 5 (without Ag bus electrode) has the highest series resistance, and the devices without HIL (device 2 and 5) have the lower series resistance than the reference devices (device 1 and 4). The series resistance varies according to the existence the Ag bus line electrode and HIL, which indicates that the Ag bus electrode and HIL components as well as a lead resistance, contact resistance and anode resistance should be included in the series resistance.

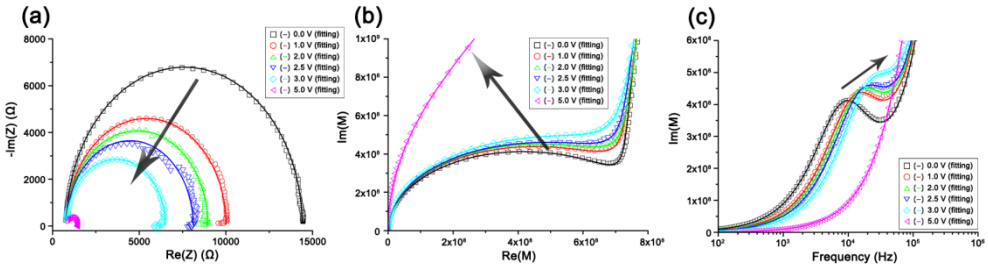

Figure 5.4 (a) Cole-Cole plots (b) M plots (c) Bode plots of the device 1

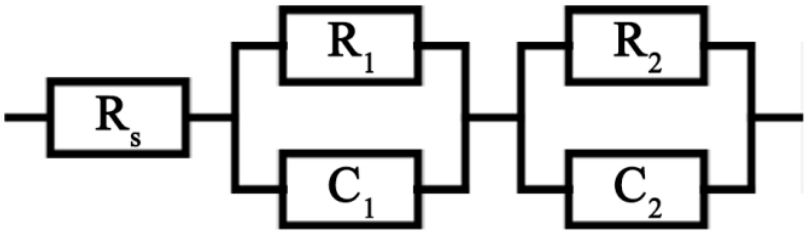

Figure 5.5 Equivalent circuit

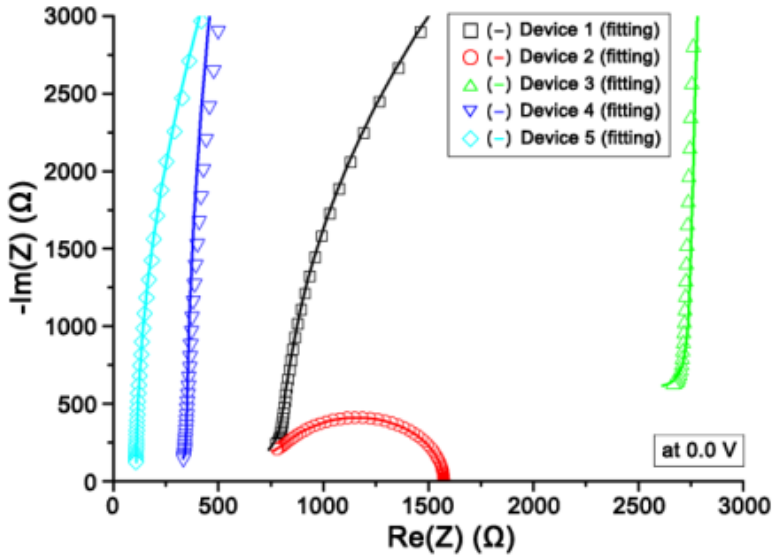

Figure 5.6 Cole-Cole plots of the high frequency region

5.3.3 Devices without HIL or Bus Electrodes

In the off-region where the operating voltage of 1.0 V is applied, Cole-Cole plots, M plots and bode plots are depicted in the **Figure 5.7** (a) ~ (c). The total resistance of each device can be extracted from the position and the size of the semi-circle's diameter in the Cole-Cole plots (**Figure 5.7** (a)). The magnitude of total resistance in the off-region is arranged device 3, device 4, device 1, device 5, and device 2 in sequence. The total resistances of the device without HIL (device 2 and 5) are lower than those of the reference devices with HIL as well as the series resistance. **Figure 5.7** (d) ~ (f) show the plots of the impedance spectroscopy where the operating voltage of 3.0 V is applied. The diameter size of the ITO-based device (device 4) is smaller than that of the PEDOT:PSS-based device (device 1) after the turn-on although the diameter size of device 4 is larger than that of device 1 in the off-region (**Figure 5.7** (a) and (d)) because the more holes can be injected to the organic layer in case of the ITO-based device due to the low sheet resistance of ITO. This tendency is well matched with the IV characteristics (**Figure 5.3**).

In M plots (**Figure 5.7** (b) and (e)), most of the devices have two semicircles regardless of the existence of HIL and Ag bus line electrode. The left semi-circles, which are response to the high frequency region, are varied according to the applied voltage. However, the right semi-circles, which are

response to the low frequency region, are not changed evidently. The apex of the bode plots (**Figure 5.7** (c) and (f)) moves to the high frequency region with increasing the applied voltage due to the decreased resistance.

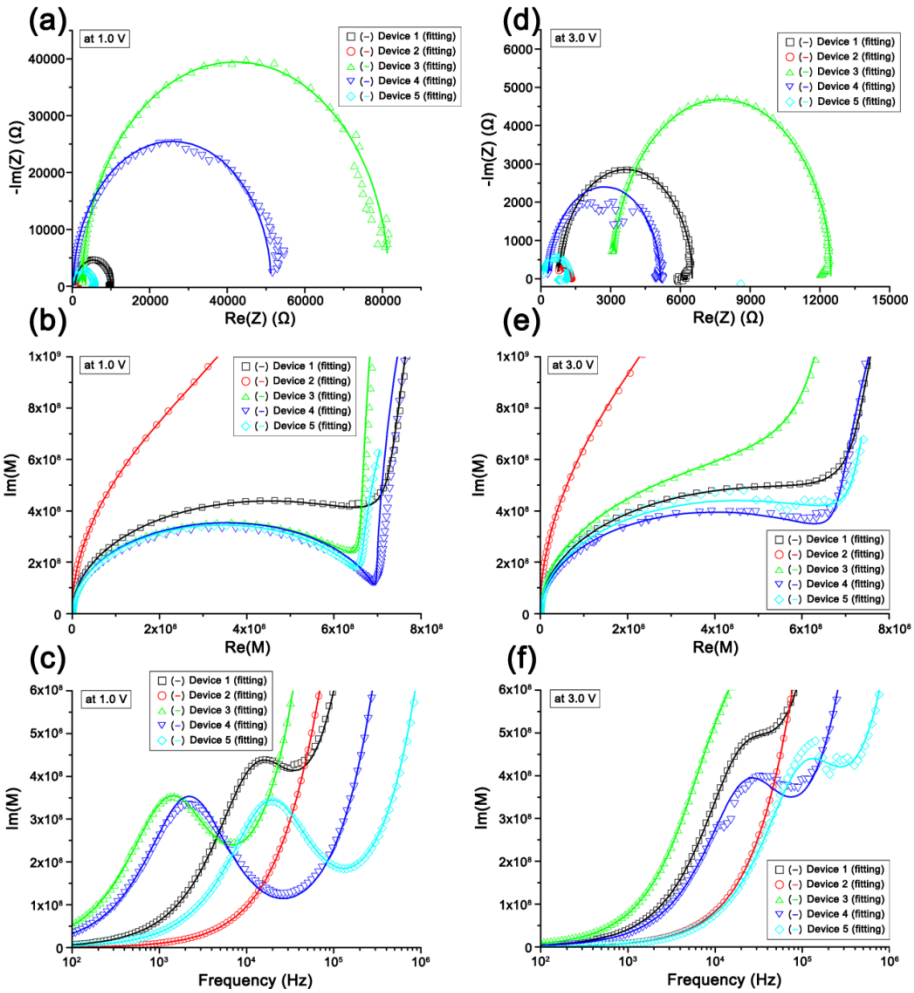

Figure 5.7 Plots of impedance spectroscopy (a) Cole-Cole plots (b) M plots (c) bode plots at 1.0 V (d) Cole-Cole plots (e) M plots (f) bode plots at 3.0 V

	voltage (V)	R_s (Ω)	R_i (Ω)	C_i (nF)	R_b (Ω)	C_b (nF)
device 1	0.0	655	150	1.04	13600	1.37
	1.0	665	150	1.17	9200	1.37
	2.0	665	150	1.12	8150	1.36
	2.5	665	150	1.03	7300	1.37
	3.0	665	150	1.28	5700	1.37
	5.0	680	150	1.28	670	1.35
device 2	0.0	570	210	0.38	790	1.50
	1.0	570	210	0.37	750	1.50
	2.0	570	210	0.39	670	1.51
	2.5	570	210	0.43	610	1.58
	3.0	570	210	0.39	530	1.45
	5.0	570	215	0.41	390	1.43
device 3	0.0	1850	900	0.21	272000	1.51
	1.0	1850	830	0.21	79000	1.51
	2.0	1850	865	0.21	51000	1.51
	2.5	1850	860	0.21	36300	1.55
	3.0	2000	930	0.20	9500	1.53
	5.0	2200	950	0.20	1350	1.54
device 4	0.0	300	50	2.34	82500	1.43
	1.0	290	55	2.01	51000	1.43
	2.0	270	63	1.99	37500	1.45
	2.5	240	90	1.80	11700	1.47
	3.0	265	75	1.62	4800	1.46
	5.0	180	80	0.47	360	1.40
device 5	0.0	60	50	0.54	30000	1.51
	1.0	60	50	0.52	5550	1.51
	2.0	60	50	0.47	2870	1.50
	2.5	60	70	0.35	1850	1.41
	3.0	50	55	0.18	1120	1.37
	5.0	50	55	0.24	510	1.46

Table 5.1 Parameters of each equivalent circuit

5.3.4 Analysis with Impedance Spectroscopy

Details of the fitted parameters of the IS analysis for the five types of the PLEDs are summarized in **Table 5.1**. While the other parameters are not varied so much by the operating voltage, the second parallel resistance (R_2) decreases evidently. In many cases,[1-3, 6-7] the authors assigned the equivalent circuit which composed with one series resistance and two parallel RC circuits, a single RC circuit to the hole transport layer such as α-NPB or TPD and another RC circuit to the emissive layer. However, in our case, the component of HIL must be included in the series resistance region because the series resistance of our devices is affected by the existence of HIL. From these results, I can conclude that these series resistances include the contact resistance, the anode resistance, and the resistance of HIL because the series resistance is varied according to the sheet resistance of anode material, the existence of HIL, and the existence of the bus line electrode. Although HIL is included in the series resistance, two semi-circles are depicted in the M plots (**Figure 5.7** (b) and (e)).

With these results, EML should be split into two regions, the interface region (R_i and C_i) and the bulk region (R_b and C_b). The series resistances and interface resistances are maintained regardless of the applied voltage (**Figure 5.8** (a) and (b)). In contrast with the PEDOT:PSS-based devices, the interface capacitance of the ITO-based devices are decreased with the increasing

applied voltage after turn on. The variations of the interface capacitance of the ITO-based devices shows the microscopic changes of the interfacial region due to the diffusion of a metal such as indium.[13]

The remarkable point is that the bulk resistances of the EML for the five devices are decreased with increasing the applied voltage while the bulk capacitances are almost independent of the bias voltage. The decreased bulk resistances are related to the SCLC theory, which the relation of the bulk resistance (R_b) and the bias voltage is given by **Equation 5.1**.[12]

Equation 5.1 $R_b \propto V/J \propto V^{-m}$

The *m* is obtained by the linear fitting of the **Figure 5.8** (c), and the m is 3.6, 0.4, 2.4, 5.1, and 1.9 in device 1 to 5, respectively. The linear dependency of *log* R_b versus log *V* implies that the conductivity of the mobile charge in the EML follows the SCLC relation. Moreover, the bulk capacitance is followed the SCLC condition, where the total charge of the bulk region is equal to C_bV. The invariance of the bulk capacitance is because the chemical structure of the EML does not changed under the bias voltage.[12] With these results, the equivalent circuit of our PLEDs can be modeled which is composed of one series resistance, which contains several resistance and HIL, and two RC circuits which are the bulk region and the interface region of EML. The schematic image of our device and the equivalent circuit is shown in **Figure 5.9**.

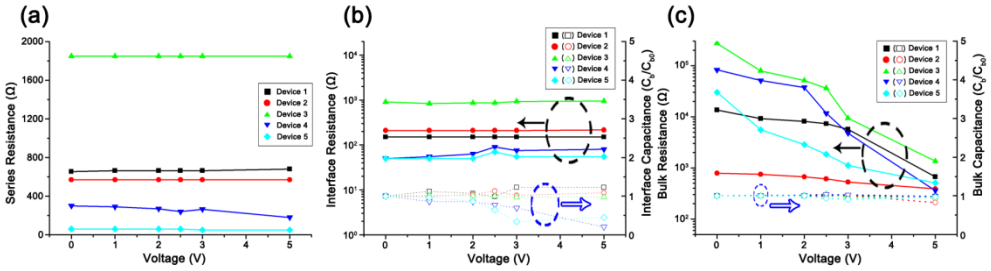

Figure 5.8 (a) Series resistance versus voltage (b) interface resistance and normalized interface capacitance versus voltage (c) bulk resistance and normalized bulk capacitance versus voltage

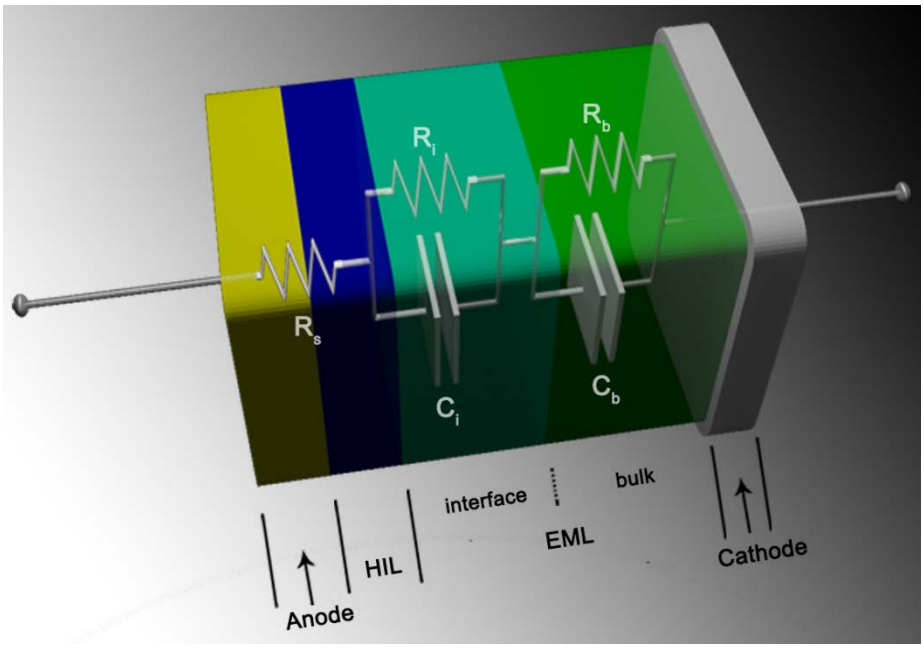

Figure 5.9 Schematic image of equivalent circuit

5.4 The relationship of efficiency and IS parameters

5.4.1 Two Parallel RC Circuits

A small and alternating electrical signal with small amplitude V_{AC} and frequency *f* is applied to the device in addition to a constant bias voltage V_{DC} in IS experiment. A total applied voltage *V(t)* is resulted in **Equation 5.2**.

Equation 5.2 $$V(t) = V_{DC} + V_{AC}(t) = V_{DC} + V_{AC} \cdot \cos(2\pi f \cdot t)$$

The current *I(t)* is a result of a combination of AC and DC response.

Equation 5.3 $$I_{AC}(t) = I_{AC} \cdot \cos(2\pi f \cdot t + \varphi)$$

In the **Equation 5.3**, φ is a phase shift between current and voltage.

The complex impedance Z is defined as the ratio of the applied alternating current and voltage response including their mutual phase shift, which is expressed in **Equation 5.4**.

Equation 5.4 $$Z = Re(Z) + Im(Z)$$

A resistor with resistance *R* has the complex impedance *R*, a capacitor with capacitance *C* has $1/i\omega C$. In a parallel RC circuit, the impedance *Z* was obtained from **Equation 5.5**.

Equation 5.5 $$Z = \frac{1}{\frac{1}{R}+i\omega C} = \frac{R}{1+i\omega RC} = \frac{R}{1+\omega^2R^2C^2} - i\frac{\omega R^2 C}{1+\omega^2R^2C^2}$$

In the **Equation 5.5**, the real part *Re*(*Z*) and imaginary part *Im*(*Z*) of the impedance *Z* are

Equation 5.6 $Re(Z) = \frac{R}{1+\omega^2 R^2 C^2}$, $Im(Z) = -\frac{\omega R^2 C}{1+\omega^2 R^2 C^2}$.

Considering two of parallel RC circuits (**Figure 5.10**), the impedance of this circuits is

Equation 5.7

$$\boldsymbol{Z_{total} = Z_1 + Z_2 = \{Re(Z_1) + Re(Z_2)\} + i\{Im(Z_1) + Im(Z_2)\}}$$

The capacitance *C* is defined as

Equation 5.8 $\boldsymbol{C_{total} = \frac{1}{\omega} \cdot \frac{-Im(Z_{total})}{(Re(Z_{total}))^2 + (Im(Z_{total}))^2}}$

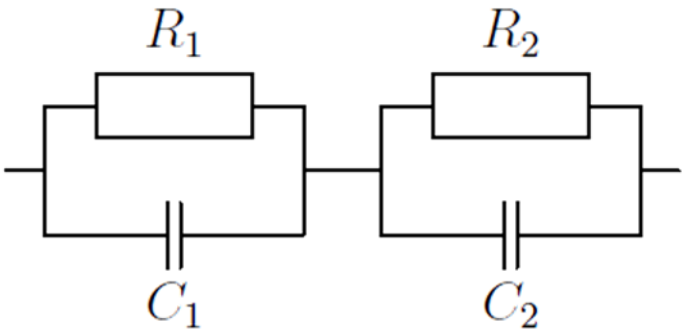

Figure 5.10 Two parallel RC circuits

From **Equation 5.8**, the total capacitance for the two parallel RC circuits is calculated as **Equation 5.9**.

Equation 5.9

$$C_{total} = \frac{1}{\omega} \cdot \frac{-Im(Z_{total})}{(Re(Z_{total}))^2 + (Im(Z_{total}))^2}$$

$$= \frac{1}{\omega} \cdot \frac{-\{Im(Z_1) + Im(Z_2)\}}{(Re(Z_1) + Re(Z_2))^2 + (Im(Z_1) + Im(Z_2))^2}$$

$$= \frac{1}{\omega} \cdot \frac{\frac{\omega {R_1}^2 {C_1}}{1+\omega^2 {R_1}^2 {C_1}^2} + \frac{\omega {R_2}^2 {C_2}}{1+\omega^2 {R_2}^2 {C_2}^2}}{\left(\frac{R_1}{1+\omega^2 {R_1}^2 {C_1}^2} + \frac{R_2}{1+\omega^2 {R_2}^2 {C_2}^2}\right)^2 + \left(\frac{\omega {R_1}^2 {C_1}}{1+\omega^2 {R_1}^2 {C_1}^2} + \frac{\omega {R_2}^2 {C_2}}{1+\omega^2 {R_2}^2 {C_2}^2}\right)^2}$$

$$= \frac{{R_1}^2 {C_1}}{(1+\omega^2 {R_1}^2 {C_1}^2)\left\{\left(\frac{R_1}{1+\omega^2 {R_1}^2 {C_1}^2} + \frac{R_2}{1+\omega^2 {R_2}^2 {C_2}^2}\right)^2 + \left(\frac{\omega {R_1}^2 {C_1}}{1+\omega^2 {R_1}^2 {C_1}^2} + \frac{\omega {R_2}^2 {C_2}}{1+\omega^2 {R_2}^2 {C_2}^2}\right)^2\right\}}$$

$$+ \frac{{R_2}^2 {C_2}}{(1+\omega^2 {R_2}^2 {C_2}^2)\left\{\left(\frac{R_1}{1+\omega^2 {R_1}^2 {C_1}^2} + \frac{R_2}{1+\omega^2 {R_2}^2 {C_2}^2}\right)^2 + \left(\frac{\omega {R_1}^2 {C_1}}{1+\omega^2 {R_1}^2 {C_1}^2} + \frac{\omega {R_2}^2 {C_2}}{1+\omega^2 {R_2}^2 {C_2}^2}\right)^2\right\}}$$

Substitute A for $1+\omega^2 {R_1}^2 {C_1}^2$, and B for $1+ \omega^2 {R_2}^2 {C_2}^2$,

Equation 5.10

$$= \frac{{R_1}^2 {C_1}}{A \cdot \left\{\left(\frac{R_1}{A} + \frac{R_2}{B}\right)^2 + \left(\frac{\omega {R_1}^2 {C_1}}{A} + \frac{\omega {R_2}^2 {C_2}}{B}\right)^2\right\}} + \frac{{R_2}^2 {C_2}}{B \cdot \left\{\left(\frac{R_1}{A} + \frac{R_2}{B}\right)^2 + \left(\frac{\omega {R_1}^2 {C_1}}{A} + \frac{\omega {R_2}^2 {C_2}}{B}\right)^2\right\}}$$

$$= \frac{{R_1}^2 {C_1}}{A \cdot \frac{{R_1}^2 B^2 + 2R_1 R_2 AB + {R_2}^2 A^2 + \omega^2 {R_1}^4 {C_1}^2 B^2 + 2\omega^2 {R_1}^2 {R_2}^2 C_1 C_2 AB + \omega^2 {R_2}^4 {C_2}^2 A^2}{A^2 B^2}}$$

$$+ \frac{{R_2}^2 {C_2}}{B \cdot \frac{{R_1}^2 B^2 + 2R_1 R_2 AB + {R_2}^2 A^2 + \omega^2 {R_1}^4 {C_1}^2 B^2 + 2\omega^2 {R_1}^2 {R_2}^2 C_1 C_2 AB + \omega^2 {R_2}^4 {C_2}^2 A^2}{A^2 B^2}}$$

$$= \frac{{R_1}^2 {C_1}}{\frac{{R_2}^2 A^2 (1 + \omega^2 {R_2}^2 {C_2}^2) + 2R_1 R_2 AB(1 + \omega^2 R_1 R_2 C_1 C_2) + {R_1}^2 B^2 (1 + \omega^2 {R_1}^2 {C_1}^2)}{AB^2}}$$

$$+ \frac{{R_2}^2 {C_2}}{\frac{{R_2}^2 A^2 (1 + \omega^2 {R_2}^2 {C_2}^2) + 2R_1 R_2 AB(1 + \omega^2 R_1 R_2 C_1 C_2) + {R_1}^2 B^2 (1 + \omega^2 {R_1}^2 {C_1}^2)}{A^2 B}}$$

$$= \frac{{R_1}^2 {C_1}}{\frac{{R_2}^2 A^2 B + 2R_1 R_2 AB(1 + \omega^2 R_1 R_2 C_1 C_2) + {R_1}^2 B^2 A}{AB^2}}$$

$$+ \frac{{R_2}^2 {C_2}}{\frac{{R_2}^2 A^2 B + 2R_1 R_2 AB(1 + \omega^2 R_1 R_2 C_1 C_2) + {R_1}^2 B^2 A}{A^2 B}}$$

$$= \frac{{R_1}^2 {C_1} \cdot B + {R_2}^2 {C_2} \cdot A}{{R_2}^2 A + 2R_1 R_2 (1 + \omega^2 R_1 R_2 C_1 C_2) + {R_1}^2 B}$$

$$= \frac{{R_1}^2 {C_1}(1 + \omega^2 {R_2}^2 {C_2}^2) + {R_2}^2 {C_2}(1 + \omega^2 {R_1}^2 {C_1}^2)}{{R_2}^2 (1 + \omega^2 {R_1}^2 {C_1}^2) + 2R_1 R_2 (1 + \omega^2 R_1 R_2 C_1 C_2) + {R_1}^2 (1 + \omega^2 {R_2}^2 {C_2}^2)}$$

$$= \frac{{R_1}^2 {C_1} + {R_2}^2 {C_2} + \omega^2 {R_1}^2 {R_2}^2 C_1 C_2 (C_1 + C_2)}{(R_1 + R_2)^2 + \omega^2 {R_1}^2 {R_2}^2 (C_1 + C_2)^2}$$

Equation 5.11 $\boldsymbol{C_{total} = \frac{{R_1}^2 {C_1} + {R_2}^2 {C_2} + \omega^2 {R_1}^2 {R_2}^2 C_1 C_2 (C_1 + C_2)}{(R_1 + R_2)^2 + \omega^2 {R_1}^2 {R_2}^2 (C_1 + C_2)^2}}$

According to **Equation 5.11**, the limiting case for the total capacitance C of the two parallel RC circuits in the high frequency range is

Equation 5.12 $\lim_{f\to\infty} C(f) = C_{hf} = \frac{C_1 C_2}{C_1+C_2}$.

And, in the low frequency range

Equation 5.13 $\lim_{f\to 0} C(f) = C_{lf} = \frac{{R_1}^2 C_1+{R_2}^2 C_2}{(R_1+R_2)^2}$.

The on-set frequency (f_r) is defined as

Equation 5.14 $\boldsymbol{C(f_r) = C_{hf} + \frac{C_{lf}-C_{hf}}{2} = \frac{C_{hf}+C_{lf}}{2}}$.

In case of two parallel RC circuits, the total capacitance at the on-set frequency is

Equation 5.15 $\boldsymbol{C(f_r) = \frac{1}{2}\left\{\frac{C_1C_2}{C_1+C_2} + \frac{{R_1}^2C_1+{R_2}^2C_2}{(R_1+R_2)^2}\right\}}$

$$= \frac{1}{2}\left\{\frac{C_1C_2(R_1+R_2)^2 + (C_1+C_2)\left({R_1}^2C_1 + {R_2}^2C_2\right)}{(C_1+C_2)(R_1+R_2)^2}\right\}$$

$$= \frac{1}{2}\left\{\frac{(R_1C_1+R_2C_2)^2 + 2C_1C_2\left({R_1}^2+{R_2}^2\right)}{(C_1+C_2)(R_1+R_2)^2}\right\}$$

Thus, the on-set frequency was obtained from **Equation 5.11** and **5.15**.

$$\frac{1}{2}\left\{\frac{(R_1C_1+R_2C_2)^2 + 2C_1C_2\left({R_1}^2+{R_2}^2\right)}{(C_1+C_2)(R_1+R_2)^2}\right\} = \frac{{R_1}^2C_1 + {R_2}^2C_2 + \omega^2{R_1}^2{R_2}^2C_1C_2(C_1+C_2)}{(R_1+R_2)^2 + \omega^2{R_1}^2{R_2}^2(C_1+C_2)^2}$$

$$\left\{(R_1C_1+R_2C_2)^2 + 2C_1C_2\left({R_1}^2+{R_2}^2\right)\right\}\cdot\left\{(R_1+R_2)^2 + \omega^2{R_1}^2{R_2}^2(C_1+C_2)^2\right\}$$

$$= 2\left\{{R_1}^2C_1 + {R_2}^2C_2 + \omega^2{R_1}^2{R_2}^2C_1C_2(C_1+C_2)\right\}\cdot\left\{(C_1+C_2)(R_1+R_2)^2\right\}$$

$$\left\{(R_1C_1+R_2C_2)^2 + 2C_1C_2\left({R_1}^2+{R_2}^2\right)\right\}\cdot(R_1+R_2)^2$$

$$+\left\{(R_1C_1+R_2C_2)^2 + 2C_1C_2\left({R_1}^2+{R_2}^2\right)\right\}\cdot\omega^2{R_1}^2{R_2}^2(C_1+C_2)^2$$

$$= 2\left({R_1}^2C_1 + {R_2}^2C_2\right)\cdot\left\{(C_1+C_2)(R_1+R_2)^2\right\}$$

$$+2\omega^2{R_1}^2{R_2}^2C_1C_2(C_1+C_2)\cdot\left\{(C_1+C_2)(R_1+R_2)^2\right\}$$

$$\omega^2 {R_1}^2 {R_2}^2 (C_1 + C_2)^2 \{(R_1 C_1 + R_2 C_2)^2 + 2C_1 C_2 ({R_1}^2 + {R_2}^2) - 2C_1 C_2 \cdot (R_1 + R_2)^2\}$$
$$= (R_1 + R_2)^2 \{2({R_1}^2 C_1 + {R_2}^2 C_2) \cdot (C_1 + C_2) - (R_1 C_1 + R_2 C_2)^2 - 2C_1 C_2 ({R_1}^2 + {R_2}^2)\}$$
$$\omega^2 {R_1}^2 {R_2}^2 (C_1 + C_2)^2 \cdot$$
$$({R_1}^2 {C_1}^2 + 2R_1 R_2 C_1 C_2 + {R_2}^2 {C_2}^2 + 2{R_1}^2 C_1 C_2 + 2{R_2}^2 C_1 C_2 - 2{R_1}^2 C_1 C_2 - 4R_1 R_2 C_1 C_2 - 2{R_2}^2 C_1 C_2)$$
$$= (R_1 + R_2)^2 \cdot$$
$$(2{R_1}^2 {C_1}^2 + 2{R_1}^2 C_1 C_2 + 2{R_2}^2 C_1 C_2 + 2{R_2}^2 {C_2}^2 - {R_1}^2 {C_1}^2 - 2R_1 R_2 C_1 C_2 - {R_2}^2 {C_2}^2 - 2{R_1}^2 C_1 C_2 - 2{R_2}^2 C_1 C_2)$$
$$\omega^2 {R_1}^2 {R_2}^2 (C_1 + C_2)^2 ({R_1}^2 {C_1}^2 - 2R_1 R_2 C_1 C_2 + {R_2}^2 {C_2}^2) = (R_1 + R_2)^2 ({R_1}^2 {C_1}^2 - 2R_1 R_2 C_1 C_2 + {R_2}^2 {C_2}^2)$$

$$\omega^2 = \frac{(R_1 + R_2)^2}{{R_1}^2 {R_2}^2 (C_1 + C_2)^2}$$

$$\omega = \frac{R_1 + R_2}{R_1 R_2 (C_1 + C_2)}$$

because of $\omega = 2\pi f$,

$$f = \frac{1}{2\pi} \cdot \frac{R_1 + R_2}{R_1 R_2 (C_1 + C_2)}$$

Assuming that one of the two resistors is significantly less resistive ($R_2 \gg R_1$),

Equation 5.16 $\boldsymbol{f = \frac{1}{2\pi} \cdot \frac{1}{R_1 (C_1 + C_2)}}$

5.4.2 Devices

To investigate the relationship between the efficiency of the device and the IS parameter of its equivalent circuit, I fabricated three type's PLEDs on the plastic substrate. I used three different substrates, PA, PS/PA and SiN_x/PA. As the transparent electrode, the PEDOT:PSS was applied with the inkjet printing method. Two organic layers were used as the HIL (AI 4083) and EML (SPG-01T), then the cathode (LiF/Al) was deposited by a thermal evaporation. The detail process condition can be referred to the experiments of the previous **chapter**. The schematic images of the PLEDs are shown in **Figure 5.11**.

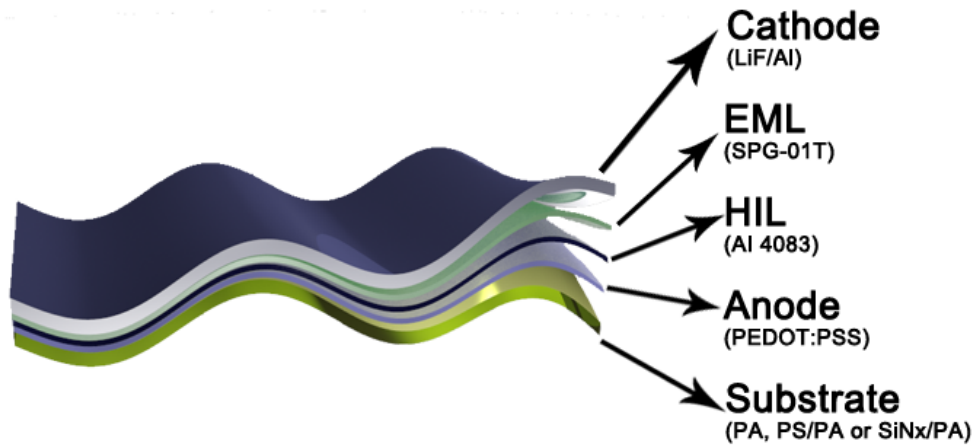

Figure 5.11 Schematic image of the device

In **Figure 5.12**, The I-V-L characteristics and efficiencies of the PLEDs are shown. The PLEDs which fabricated on the SiN_x/PA substrate (PEDOT-

SiN_x/PA) has the highest current level among the three devices, and the PLEDs which fabricated on the PA substrate (PEDOT-PA) has the lowest current level. On the other hands, the PLEDs are arranged the PEDOT-PS/PA, which fabricated on the PS/PA substrate, the PEDOT-SiNx/PA, and the PEDOT-PA according to its luminance value in the high voltage region (>5V). In the efficiency graph (**Figure 5.12** (b)), the PEDOT-PS/PA PLEDs has the highest maximum current and power efficiency (6.33 cd/A at 260 cd/m^2 and 5.91 lm/W at 116 cd/m^2). Although the PEDOT-PS/PA PLEDs and the PEDOT-SiN_x/PA PLEDs have the similar efficiency, the PEDOT-PA PLEDs has the lowest current and power efficiency, which is about 58 % of the current efficiency and 52 % of the power efficiency of the PEDOT-PS/PA PLEDs in the vicinity of 1,000 cd/m^2.

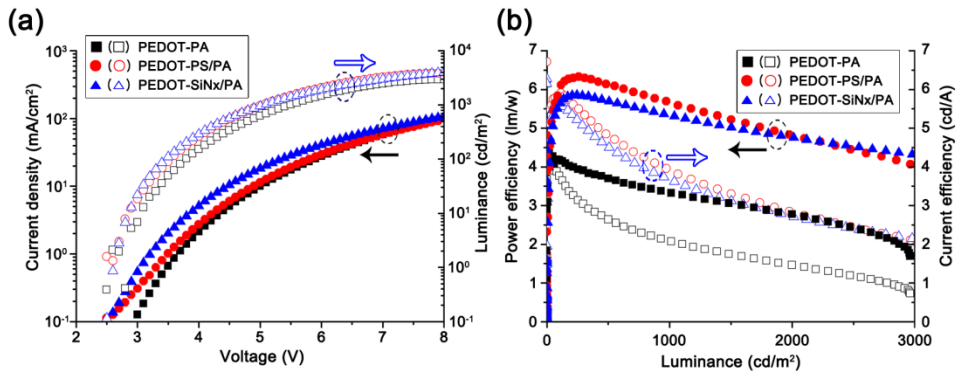

Figure 5.12 Characteristics of the PLEDs (a) I-V-L (b) efficiency graph

5.4.3 Properties of the PEDOT:PSS anode

To study the origin of the efficiency difference depending on the substrate, I investigate the properties of the PEDOT:PSS anode on the different substrate including thickness, sheet resistance, and transmittance (**Figure 5.13**). Although all of the samples have the similar transmittance (86~89%) which includes the transmittance of the substrate, the thickness of the PEDOT:PSS anode on the SiN_x/PA substrate has the lowest, and the sheet resistance of the PEDOT:PSS anode were varied from 381.4 Ω/□ (PEDOT:PSS on the SiN_x/PA) to 485.12 Ω/□ (PEDOT:PSS on the PA).

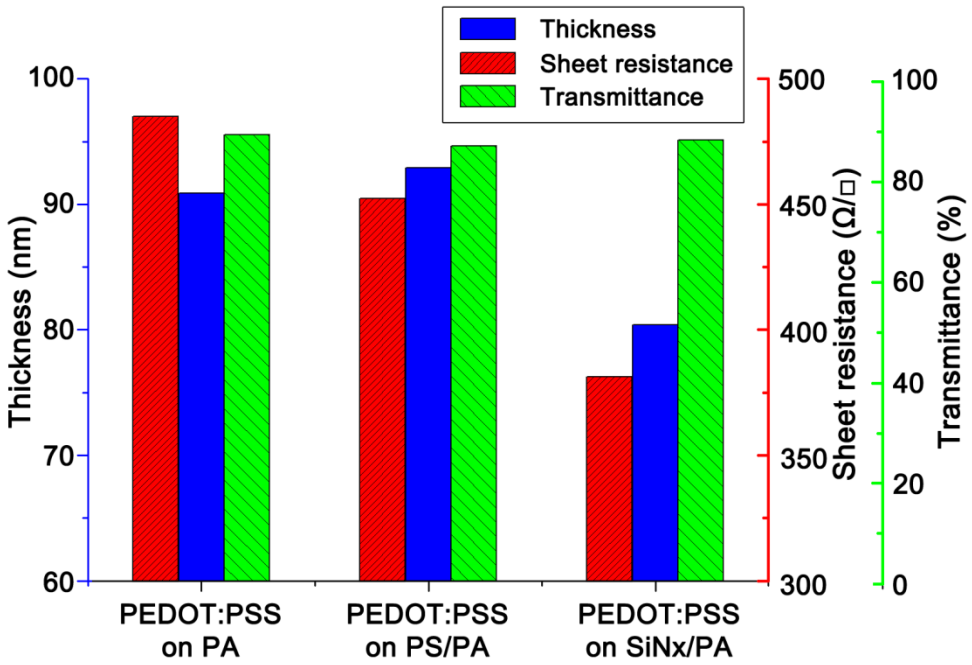

Figure 5.13 Properties of the PEDOT:PSS films on the plastic substrates

Moreover, in order to study the effect of the surface energy, its value of each substrate was investigated. The surface energy of the substrates was measured by a custom made surface energy measurement system by dropping two solutions, water and diiodomethane. The drop images are shown in **Figure 5.14**, and the surface energy of the substrates was calculated by the Owens-Wendt model analysis,[14] which was summarized in **Table 5.2**. The surface energy of the PS/PA substrate is comparable to that of the SiN_x/PA substrate, which is higher than that of the PA substrate. The PEDOT:PSS anode fabricated on the substrate which has a high surface energy shows a lower sheet resistance, which results in the enhanced current flow. If the device was fabricated on the substrate with a high surface energy and high transmittance, the current of the device would be improved.

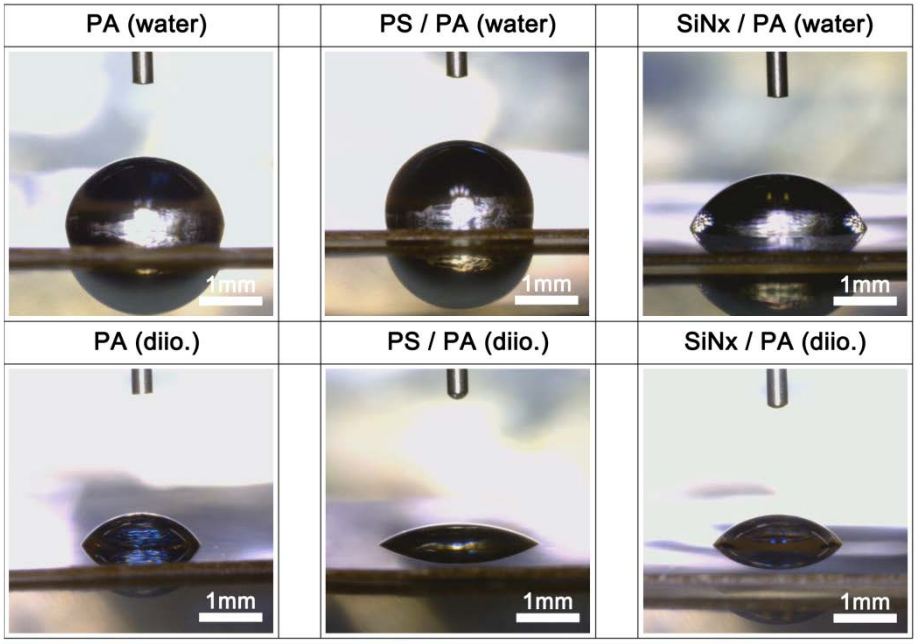

Figure 5.14 Droplet images for measuring the surface energy

Owens-Wendt model analysis					
sample	Contact angle (deg)		Dispersion term (mJ/m^2)	Polar term (mJ/m^2)	Surface energy (mJ/m^2)
	Water	Diiodomethane			
PA	86.40	56.30	30.70	3.22	33.92
SiNx / PA	65.90	56.70	30.50	12.71	43.21
PS / PA	89.10	35.80	41.66	0.92	42.57

Table 5.2 Surface energy

5.4.4 IS Measurements

The on-set frequency of the PLEDs can be extracted from the *Im*(*Z*) versus frequency (*f*) plots, which can be obtained from the apex of the *Im*(*Z*)-*f* plots. **Figure 5.15** shows the *Im*(*Z*)-*f* plots in log scale after the turn-on of the device. The on-set frequency is shifted to the higher frequency region according to the applied bias voltage increase. The on-set frequency is inversely proportional to the resistance of the EML (**Equation 5.16**). The mobile charges such as electrons and holes injected from cathode or anode are accumulated in the EML with the applied bias voltage. The amount of the accumulated mobile charges increases according to the bias voltage increase. Due to the increased mobile charges, the resistance of the EML decreases, and thus the on-set frequency of the PLEDs is shifted to the higher frequency.

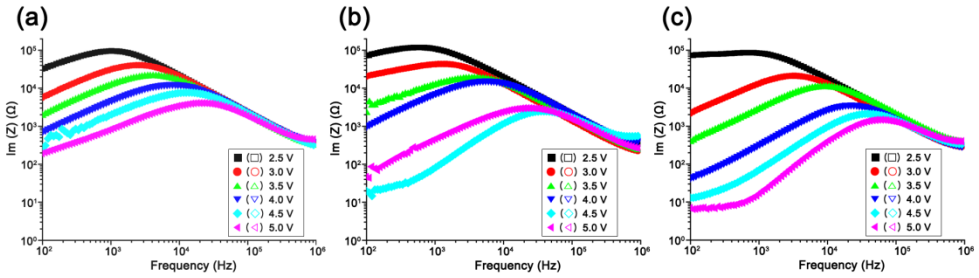

Figure 5.15 Im(z) versus F plots (a) PLEDs on the PA substrates (b) PLEDs on the PS/PA substrates (c) PLEDs on the SiNx/PA substrate

To study quantitatively this phenomenon, the on-set frequencies of the PLEDs are plotted as a function of the applied bias voltage in **Figure 5.16**. The on-set frequency of the PLEDs increases exponentially with the square root of the applied bias voltage.

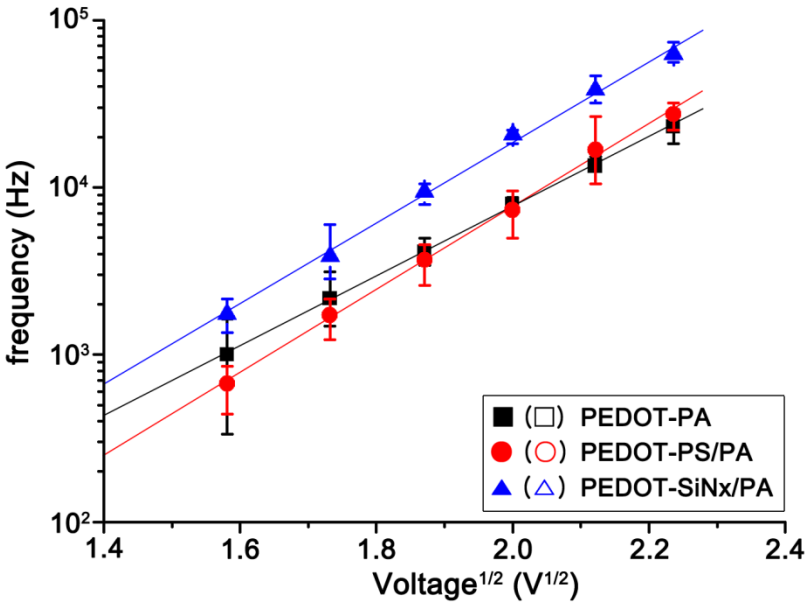

Figure 5.16 Frequency versus the square root of the applied bias voltage

From **Figure 5.16**, the slope of the graph can be estimated, and the results are 1.969, 2.020, and 1.616 for the PLEDs on the SiNx/PA, PS/PA, and PA substrates, respectively. In the **Figure 5.17**, the maximum current efficiency, power efficiency, and the slope from the frequency-voltage plots are shown, which shows that the higher the device has the current and power efficiencies, the higher the slop from the frequency-voltage graph (**Figure**

5.17) is. To obtain the higher slope in the frequency versus the root of voltage, the more mobile charge such as electrons and holes should be efficiently injected to the organic materials with the increase applied bias voltage. The efficiency of the OLEDs is related to the efficient charge injection, the balance between injected electrons and holes, the efficient exciton formation by the recombination of electrons and holes, and extraction of the generated lights. In the PLEDs used in this work, all of the device conditions are identical without the substrate, which shows that the morphology and electrical property of the anode affect the efficiency of the devices. In case of the PEDOT-SiN_x/PA PLEDs, the more holes can be injected to the organic layer due to the low sheet resistance of its anode, and thus the carrier mobility of the organic layers is higher than that of the other device. However, the charge balance of the PEDOT-PS/PA PLEDs is slightly higher than that of the PEDOT-SiN_x/PA PLEDs, which brings about the high efficiencies of the PEDOT-PS/PA PLEDs. With the proper charge balance, the exciton formatted in the recombination zone is more easily generated to the lights, and the more charge can be injected, and thus the on-set frequency of the PEDOT-PS/PA PLEDs increases quickly.

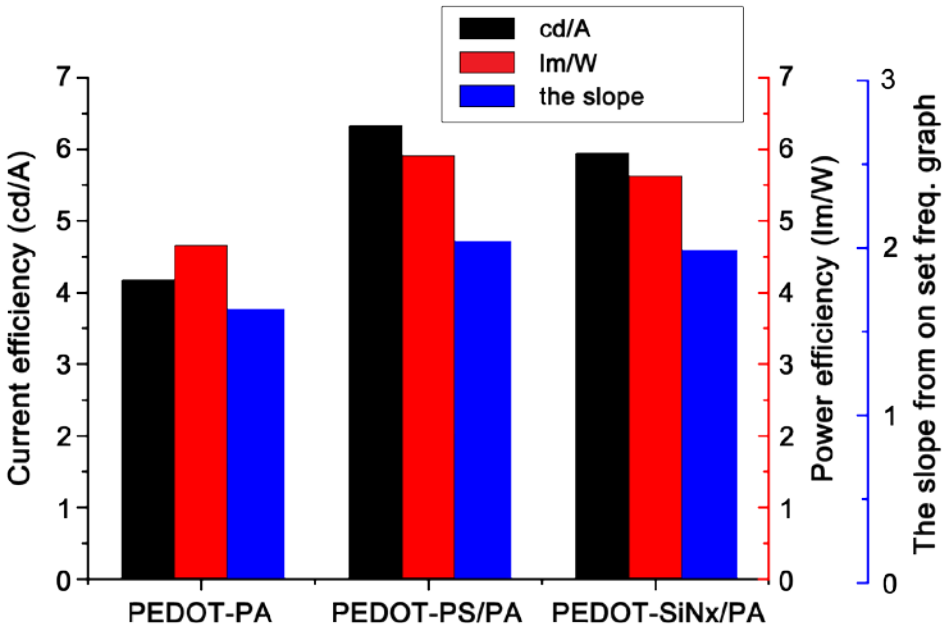

Figure 5.17 Efficiencies of the PLEDs and slope from on-set frequency graph

5.5 Summary

I conducted the IS measurements and analysis of PLEDs. I modeled the equivalent circuit of our devices, which is composed with a series resistance and two parallel RC circuits. In the series resistance, the anode resistance, the contact resistance, and the resistance of HIL are included. In contrast to the previous papers, EML should be divided by the interface region and the bulk region, which each region has a parallel resistance and a capacitance.

Moreover, I showed the relationship between the IS parameters and the efficiency of the PLEDs, which the slope of the on-set frequency is related to the current and power efficiency.

References

[1] E. Nam, H. Park, K. Park, M. R. Moon, S. Sohn, D. Jung, J. Yi, H. Chae, and H. Kim, *Thin Solid Films* **517**, 4131 (2009)

[2] L. S. C. Pingree, M. T. Russell, T. J. Marks, and M. C. Hersam, *Thin Solid Films* **515**, 4783 (2007)

[3] L. S. C. Pingree, M. T. Russell, T. J. Marks, and M. C. Hersam, *J. Appl. Phys*. **100**, 044502 (2006)

[4] S. H. Kim, S. C. Kim, J. H. Lee, and T. Zyung, *Curr. Appl. Phys*. **5**, 35 (2005)

[5] V. Shrotriya and Y. Yang, *J. Appl. Phys*. **97**, 054504 (2005)

[6] Y. S. Lee, J.-H. Park, J. S. Choi, and J. I. Han, *Jpn. J. Appl. Phys*. **42**, 2715 (2003)

[7] S. Nowy, W. Ren, A. Elschner, W. Lövenich, and W. Brütting, *J. Appl. Phys*. **107**, 054501 (2010)

[8] T. Okachi, T. Nagase, T. Kobayashi, and H. Naito, *Thin Solid Films* **517**, 1327 (2008)

[9] G. G.-Belmonte, H. J. Bolink, and J. Bisquert, *Phys. Rev. B* **75**, 085316 (2007)

[10] J. H. Burroughes, D. D. C. Bradley, A. R. Brown, R. N. Marks, K. Mackay, R. H. Friend, P. L. Burns, and A. B. Holmes, *Nature* **347**, 539 (1990)

[11] X. Wu, E. S. Yang, and H. L. Evans, *J. Appl. Phys*. **68**, 2845 (1990)

[12] S. H. Kim, K.-H. Choi, H.-M. Lee, D.-H. Hwang, L.-M. Do, H. Y. Chu, and T. Zyung, *J. Appl. Phys*. **87**, 882 (2000)

[13] S. J. Jo, C. S. Kim, J. B. Kim, S. Y. Ryu, J. H. Noh, H. K. Baik, Y. S. Kim, and S.-J. Lee, *J. Appl. Phys*. **103**, 114502 (2008)

[14] D. K. Owens, *J. Appl. Polym. Sci*. **13**, 1741 (1969)

[15] J. Shao, G. T. Wright, *Solid-State Electronics* **3**, 291 (1961)

[16] W. Brütting, H. Riel, T. Beierlein, W. Riess, *J. Appl. Phys*. **89**, 1704 (2001)

Chapter 6 Conclusion

In this thesis, I report the flexible polymer light-emitting diodes (PLEDs) with the several flexible transparent anodes on the rigid and plastic substrates for replacing ITO. By optimizing the fabrication process including the selection of materials, the control ofe UVO_3 treatments and inkjet printing process, and the introduction of 2D nano hole structures, highly efficient transparent and flexible PLEDs were demonstrated.

For the graphene anode, I used the single layer graphene anode in order to reduce the transfer step of the elastic stamping. The patterning of the single layer graphene and the control of its work function could be realized by the UVO_3 treatments by controlling the irradiation time. With the appropriate selection of Ag bus line electrode, the voltage drops could be reduced in the my devices. Although the PLEDs with the single layer graphene anodes showed the similar performance to the ITO-based PLEDs, however, the limitations such as the flatness for the transfer of the graphene film, low

conductivity, and relatively low work function, should be resolved to apply the future optoelectronic applications.

For the PEDOT:PSS anode, I fabricated the highly efficient flexible and foldable PLEDs with the highly transparent and flexible conductive polymeric anodes deposited by the inkjet printing process. The PEDOT:PSS anodes showed higher transmittance and higher work function than the ITO anodes. By the selectively modulated inkjet printing process, the PEDOT:PSS electrodes could be utilized to the anodes or the bus line electrodes. The PEDOT:PSS PLEDs showed the higher current and power efficiency than that of ITO PLEDs. Moreover, After the bending stress, even after the folding stress, the PEDOT:PSS PLEDs showed unchanged device properties. In order to apply the PEDOT:PSS electrodes to the real device, the low conductivity of the PEDOT:PSS should be resolved. It is realized by collaborating the PEDOT:PSS and high conductive transparent electrodes such as silver nanowires, metal grid, and transparent conductive oxide.

For the highly efficient lighting applications, I successfully demonstrated that the high performance flexible PLEDs with the 2D nano hole arrays and the flexible PEDOT:PSS anodes. The flexible photonic crystal (PC) structures embedded PLEDs were reported for the first time, and its devices had much higher efficiency than the normal PLEDs. Although the diffraction patterns occurred by the 2D nano hole arrays were one of the

obstacles in the display applications, the emission generated by the PC structures between the adjacent pixels could be enhanced the luminance in the lighting applications. Moreover, although the fabrication process of the PC structures was complicated and had the limitation to apply a large size substrate in the laser holographic lithography, the OLEDs with PC structures could be commercialized in the real device along with a simple fabrication process such as nanosphere lithography.

I also reported the equivalent circuit of the PLEDs with the impedance spectroscopy. With the impedance spectroscopy, I studied the effectiveness of HIL and bus line electrodes, which related to the series resistance. Also I studied the difference characteristics of the PLEDs which fabricated on the different anode materials. Moreover, I showed that the resistance of the EML decreased according to the applied bias voltage, which was due to the injection of the mobile charges. In addition, I showed the relationship between the IS parameter and the efficiency of the PLEDs, which the higher the slop from the charge carrier mobility is, the higher the efficiency of the devices is.

From this Ph.D. dissertation, I believe that the conductive polymeric electrodes or the hybrid conductive polymeric electrodes have a great potential to replace ITO electrodes for the flexible and low cost optoelectronics devices. Moreover, the impedance spectroscopy can be

applied to investigate the operational principles or the lifetime of the OLEDs based on my research results.

Publications and Conferences

[1] International Journals

1. ***J. Ha***, S. Park, D. Kim, J. Ryu, C. Lee, B. H. Hong, Y. Hong, *Org. Electron*. **14**, 2324 (2013)
2. T. Kim, H. Song, ***J. Ha***, S. Kim, D. Kim, S. Chung, J. Lee, Y. Hong, *Appl. Phys. Lett*. **104**, 113103 (2014)
3. ***J. Ha***, J. Park, J. Ha, D. Kim, S, Chung, C. Lee, Y. Hong, *Org. Electron. Accepted*
4. D. Kim, ***J. Ha***, J. Park, J. Hwang, H. Jeon, C. Lee, Y. Hong, *Org. Electron. Submitted, (**equally contributed**)*
5. ***J. Ha***, J. Park, H. Im, C. Lee, Y. Hong, *Manuscript preparation for Appl. Phys. Lett. Submittion*
6. ***J. Ha***, D. Kim, J. Park, S. Lee, H. Jeon, C. Lee, Y. Hong, *Manuscript preparation for Nat. Commun. Submittion*

[2] Proceeding

1. ***J. Ha***, S. Park, D. Kim, J. Ryu, C. Lee, B. H. Lee, Y. Hong, *SPIE Optics+Photonics 2012*, 8476 0Y
2. D. Kim, ***J. Ha***, Y. Hong, *SPIE Optics+Photonics 2012*, 8476 67
3. ***J. Ha***, J. Park, J. Ha, D. Kim, C. Lee, Y. Hong, *IDW'13*, OLED4-2

[3] Oral Presentation

1. ***J. Ha***, S. Park, D. Kim, J. Ryu, C. Lee, B. H. Lee, Y. Hong, *SPIE Optics+Photonics 2012*, 8476 0Y
2. ***J. Ha***, J. Park, J. Ha, D. Kim, C. Lee, Y. Hong, *IDW'13*, OLED4-2
3. ***J. Ha***, J. Park, J. Ha, D. Kim, K. Kim, C. Lee, Y. Hong, *EMRS 2014 Spring Meeting*, R.VIII 4
4. ***J. Ha***, D. Kim, J. Park, S. Lee, H, Jeon, C. Lee, Y. Hong, *SPIE Photonics West 2015*, 9385-26

[4] Poster Presentation

1. D. Kim, ***J. Ha***, Y. Hong, *SPIE Optics+Photonics 2012*, 8476 1W
2. S. Chung, J. Ha, ***J. Ha***, Y. Hong, *IWFPE 2012*, P-PE15
3. J. Park, ***J. Ha***, C. Lee, Y. Hong, *EMRS 2014 Spring Meeting*, R.PI 13
4. ***J. Ha***, J. Park, J. Ha, D. Kim, C. Lee, Y. Hong, *IWFPE 2012*, I-17
5. D. Kim, ***J. Ha***, J. Park, S. Lee, H. Jeon, C. Lee, Y. Hong, 2014 MRS Fall Meeting

한글 초록

본 박사논문에서 고효율 플랙시블 디스플레이 개발을 위해 기존 산화 인듐 (ITO) 전극을 대체할 수 있는 투명 플랙시블 전극을 연구하였다. 최근들어, 그래핀, 은 나노와이어, 전도성 폴리머, 탄소 나노튜브, 메탈 메쉬 그리드, 얇은 메탈 박막 등 여러 유연성 전극을 이용하여 제작한 유연성 소자의 결과물들이 보고되고 있다.

하지만, 폴리머 발광 소자의 경우, 단순한 소자 구조, 값싼 비용 및 용액공정으로 소자 제작이 가능하다는 장점이 있음에도 불구하고, 그래핀 전극을 양극으로 이용한 소자는 아직까지 활발히 보고되지 못하고 있다. 이 졸업 논문에서는 간단한 두 층으로 구성되어 있으며 한 층의 그래핀을 양극으로 사용하는 폴리머 발광 소자를 성공적으로 제작하였다. 화학기상방법으로 합성된 한 층의 그래핀은 탄성 스탬프 방식으로 유리 기판에 전사되었으며, 극자외선 오존처리의 시간과 그 파워를 조절함으로서 그래핀의 패터닝 및 일함수 튜닝이 가능함을 보여주었다. 또한 발광 특성을 개선시킬 수 있도록 그래핀 과의 접촉 저항을 줄일 수 금속 전극을 찾아내었다.

전도성 폴리머 전극의 경우, 매우 전도성이 좋고 투명하며 접을 수 있는 폴리머 전극을 이용하여 고효율 폴리머 발광소자를

제작하였다. 새로운 도핑 원소 (nMP 와 nMF)를 PEDOT:PSS 에 첨가함으로서 전도성 폴리머 전극의 전도성을 개선할 수 있었다. PEDOT:PSS 전극을 투명한 양극 및 매우 전도성이 좋은 버스 전극에 적용하기 위해, 각 조건에 적합한 잉크젯 프린팅 공정을 적용하였다. 수차례의 프린팅 공정을 진행한 전극은 은 전극과 유사한 특성을 보이며, 반면에 플라스틱 기판상에 1 회 프린팅한 전극은 ITO 전극 대비 FOM 이 더 좋은 결과를 얻었다. 폴리머 전극의 유연한 역학적 특성, 높은 투과율 및 높은 일함수로 인해 ITO 를 적용하지 않아도 고성능의 접을 수 있는 소자를 제작하였다.

소자의 외부 발광 효율을 높이기 위해 2 차원 홀 어레이 및 전도성이 높은 투명 폴리머 전극을 이용하여 고효율 유연성 소자를 제작하였다. 폴리머 전극은 선택적인 위치에 잉크젯 프린팅으로 증착되었으며, 포토닉 크리스탈이 적용된 폴리머 발광 소자는 딱딱한 기판 및 플라스틱 기판상에 제작되었고, 매우 높은 효율 특성을 보여주고있다. 포토닉 크리스탈 구조 및 폴리머 전극이 적용된 유연성 폴리머 발광 소자는 일반 소자대비 전류효율 및 전력효율이 약 1.31 배 및 1.28 배 증진된 결과를 얻었다. 더구나 본 소자는 놀라운 유연성 특성까지 보여주고 있다.

임피던스 스페트로스코피를 이용하여, 투명 유연성 전극으로 제작된 폴리머 발광소자의 작동원리를 분석하였다. 양극의 재료에 따른 동작의 차이, HIL 및 버스 전극의 유무에 의한 동작의 차이를

확인하기 위해 5 개의 소자가 제작되었다. 각 소자의 등가회로는 임피던스 스펙트로스코피에서 사용되는 다양한 그래프를 이용하여 설정하였다. 임피던스 스펙트로스코피 분석을 통해 HIL 층은 시리즈 저항성분으로 포함시켜야 하며, 발광층은 벌크 및 경계지역으로 나누어야 함을 알게 되었다. 또한 임피던스 스펙트로스코피 파라미터와 폴리머 발광 소자의 효율과의 관계를 조사하고자, 다양한 플라스틱 기판 위에서 소자를 제작하였다. 임피던스 스펙트로스코피 분석을 이용하여, 이동도 그래프에서 추출한 기울기가 소자의 효율과 밀접한 관계가 있음을 확인하였다.

주요어: 폴리머 발광 소자, 투명 전도성 전극, 그래핀, 전도성 폴리머 양극, PEDOT:PSS, 임피던스 스펙트로스코피

학번: 2011-30262